Numerical study of advection-diffusion-reaction processes in microfluidic systems

Von der Universität Bayreuth
zur Erlangung des Grades eines
Doktors der Naturwissenschaften (Dr. rer. nat.)
genehmigte Abhandlung

von

Gabriel Sitaru

aus Bîrlad, Rumänien

1. Gutachter: Prof. Dr. Stephan Gekle
2. Gutachter: Prof. Dr. Walter Zimmermann

Tag der Einreichung: 24.05.2022
Tag des Kolloquiums: 17.11.2022

Abstract

Mass transport phenomena are fundamental to many scientific and engineering applications. Two areas of great interest, i.e. catalytic synthesis and microchannel mixing, are studied in the framework provided by the interplay of advection, diffusion and reaction. This work aims to offer a deeper understanding of the role that the three mechanisms have in different setups by analysing the evolution of the concentration field, in order to improve the overall performance of the systems.

Gold nanoparticles are well-known for their high catalytic performance. Using a lattice Boltzmann solver for the advection-diffusion-reaction equation and a random walk particle tracking method, we compare the conversion curves generated by a single large particle and by two smaller particles, with radii chosen such that the total surface area is kept constant. Furthermore, we also model the anisotropic diffusion induced by increased hydrodynamic resistance next to the catalytic surface of the gold particles. We find that the reaction rates are independent of the particle size, thus excluding the surface-modified diffusion regime of the reactant as a cause for the experimentally observed change in the catalytic activity. Additionally, the reaction kinetics of gold nanoparticles immobilised on patchy hybrid nonwovens are studied in the context of the catalysed alcoholysis of dimethylphenylsilane with n-butanol. The swellability of the functional patches in n-butanol is reflected in an observed induction period. We propose an extended first order kinetics model, which captures this behaviour through the introduction of a new parameter, i.e. the accessibility rate of the reactants to the embedded catalytically active nanoparticles. Using our tool, a good fit to the experimental results is obtained, which further highlights a strong dependency of the accessibility rate on both the size and chemistry of the patches.

In the synthesis of complex chemical products, usually a series of catalytic reactions involving simpler initial substances are required. A better alternative to the traditional step-by-step approach, which requires isolation of each intermediate product, are the one-pot cascade reactions where no recovery step is needed. We study the case of a generic two-step $A \rightarrow B \rightarrow C$ reaction where the Wolf-Lamb-type

catalysts are immobilised on fibrous membranes to avoid their deactivation. The reactants are transported from the first catalytic site to the second by advection and diffusion. The efficiency of such a flow-through reactor is computed as a function of two dimensionless parameters, i.e. the Péclet and the Damköhler number, using the lattice Boltzmann method, the random walk particle tracking method and a simple analytical model. Our results show that, at higher flow speeds the system becomes less efficient, as the reactants have less time to reach the surface of the fiber, while the total production increases due to a higher advective flux. Moreover, reducing the distance between the two catalytic sites significantly increases the reaction efficiency, with the side-by-side morphology, which places both catalyst on a single fiber, yielding the best results.

Species mixing is a crucial process in microfluidic systems, such as the lab-on-a-chip technology and bioprinting, having direct impact on the efficiency and sensitivity of these devices. In this work we investigate the mixing inside a microchannel where a deformable capsule is flowing through, in the context of two passive mixers, i.e. serpentine channel and parallel lamination of the stream. Combining a lattice Boltzmann/immersed boundary scheme for the Navier-Stokes equation with a finite volume solver for the advection-diffusion equation, we simulate the coupled flow field, membrane dynamics and concentration field. We confirm that, while the channel geometry has a minimal impact on the mixing process, parallel lamination considerably decreases the distance at which uniformity is achieved. Remarkably, the passage of the microcapsule disrupts the local homogeneity over short distances in front and behind its position. Furthermore, we record the same relative deviation in the mixing values generated by the capsule for multiple concentration distributions at the inlet.

Zusammenfassung

Massentransportphänomene sind für viele wissenschaftliche und technische Anwendungen von grundlegender Bedeutung. Zwei Bereiche von großem Interesse, nämlich die katalytische Synthese und das Mischen in Mikrokanälen, werden im Rahmen des Zusammenspiels von Advektion, Diffusion und Reaktion untersucht. Diese Arbeit zielt darauf ab, ein tieferes Verständnis der Rolle zu vermitteln, die die drei Mechanismen in verschiedenen Anordnungen spielen, indem die Entwicklung des Konzentrationsfeldes analysiert wird, um die Gesamtleistung der Systeme zu verbessern.

Gold-Nanopartikel sind bekannt für ihre hohe katalytische Leistung. Unter Verwendung eines lattice Boltzmann-Lösers für die Advektions-Diffusions-Reaktionsgleichung und einer Random-Walk-Particle-Tracking-Methode vergleichen wir die Konversionskurven, die von einem einzelnen großen Partikel und von zwei kleineren Partikeln erzeugt werden, wobei die Radien so gewählt werden, dass die Gesamtoberfläche konstant bleibt . Darüber hinaus modellieren wir auch die anisotrope Diffusion, die durch erhöhten hydrodynamischen Widerstand neben der katalytischen Oberfläche der Goldpartikel induziert wird. Wir finden heraus, dass die Reaktionsgeschwindigkeiten unabhängig von der Partikelgröße sind, wodurch das oberflächenmodifizierte Diffusionsregime des Reaktanten als Ursache für die experimentell beobachtete Änderung der katalytischen Aktivität ausgeschlossen werden kann. Zusätzlich wird die Reaktionskinetik von auf patchy hybrid nonwovens immobilisierten Goldnanopartikeln im Rahmen der katalysierten Alkoholyse von Dimethylphenylsilan mit n-Butanol untersucht. Die Quellbarkeit der funktionellen Patches in n-Butanol spiegelt sich in einer beobachteten Induktionsperiode wider. Wir schlagen ein erweitertes Kinetikmodell erster Ordnung vor, das dieses Verhalten durch die Einführung eines neuen Parameters erfasst, nämlich der Zugänglichkeitsrate der Reaktanten zu den eingebetteten katalytisch aktiven Nanopartikeln. Mit unserem Tool wird eine gute Anpassung an die experimentellen Ergebnisse erzielt, was eine starke Abhängigkeit der Zugänglichkeitsrate sowohl von der Größe als auch von der Chemie der Patches unterstreicht.

Bei der Synthese komplexer chemischer Produkte sind meist eine Reihe katalytischer Reaktionen mit einfacheren Ausgangsstoffen erforderlich. Eine bessere Alternative zum traditionellen schrittweisen Ansatz, der die Isolierung jedes Zwischenprodukts erfordert, sind die Eintopf-Kaskadenreaktionen, bei denen kein Rückgewinnungsschritt erforderlich ist. Wir untersuchen den Fall einer generischen zweistufigen $A \to B \to C$-Reaktion, bei der die Wolf-Lamb-Katalysatoren auf Fasermembranen immobilisiert sind, um ihre Deaktivierung zu vermeiden. Die Reaktanten werden durch Advektion und Diffusion von der ersten katalytischen Stelle zur zweiten transportiert. Der Wirkungsgrad eines solchen Durchflussreaktors wird als Funktion zweier dimensionsloser Parameter, nämlich der Péclet- und der Damköhler-Zahl, unter Verwendung der Lattice-Boltzmann-Methode, der Random-Walk-Particle-Tracking-Methode und eines einfachen analytischen Modells berechnet. Unsere Ergebnisse zeigen, dass das System bei höheren Strömungsgeschwindigkeiten weniger effizient wird, da die Reaktanten weniger Zeit haben, die Oberfläche der Faser zu erreichen, während die Gesamtproduktion aufgrund eines höheren Advektionsflusses steigt. Darüber hinaus erhöht die Verringerung des Abstands zwischen den beiden katalytischen Stellen die Reaktionseffizienz erheblich, wobei die Side-by-Side-Morphologie, bei der beide Katalysatoren auf einer einzigen Faser platziert werden, die besten Ergebnisse liefert.

Das Mischen von chemische Spezies ist ein entscheidender Prozess in mikrofluidischen Systemen wie der Lab-on-a-Chip-Technologie und dem Biodruck, der sich direkt auf die Effizienz und Empfindlichkeit dieser Geräte auswirkt. In dieser Arbeit untersuchen wir das Mischen in einem Mikrokanal, durch den eine deformierbare Kapsel strömt, im Kontext zweier passiver Mischer, dem Serptentinenkanal und der parallelen Laminierung des Stroms. Durch die Kombination eines Lattice-Boltzmann-/Immersed-Boundary-Schemas für die Navier-Stokes-Gleichung mit einem Finite-Volumen-Solver für die Advektions-Diffusions-Gleichung simulieren wir das gekoppelte Strömungsfeld, die Membrandynamik und das Konzentrationsfeld. Wir bestätigen, dass, während die Kanalgeometrie einen minimalen Einfluss auf den Mischprozess hat, parallele Laminierung den Abstand, bei dem Gleichmäßigkeit erreicht wird, erheblich verringert. Bemerkenswerterweise stört die Passage der Mikrokapsel die lokale Homogenität nur über kurze Distanzen vor und hinter ihrer Position. Darüber hinaus erfassen wir die gleiche relative Abweichung in den von der Kapsel erzeugten Mischwerten für mehrere Konzentrationsverteilungen am Einlass.

Contents

Abbreviations

ADE	Advection-diffusion equation
ADRE	Advection-diffusion-reaction equation
Au NPs	Gold nanoparticles
BC	Boundary condition
BGK	Bhatnagar-Gross-Krook
CFD	Computational fluid dynamics
CO	Carbon monoxide
CO_2	Carbon dioxide
COV	Coefficient of variation
DMF	Dimethylformamide
FVM	Finite volume method
IBM	Immersed boundary method
LBE	Lattice Boltzmann equation
LBM	Lattice Boltzmann method
MVC	Mixing variance coefficient
$NaBH_4$	Sodium borohydride
NP	Nanoparticle
NSE	Navier-Stokes equation
PDE	Partial differential equation
PVP	Polyvinylpyrrolidone
RWPT	Random walk particle tracking
sCCMs	Spherical crystalline-core micelles
wCCMs	Worm-like crystalline-core micelles

Chapter 1

Introduction

1. INTRODUCTION

Mass transport phenomena deals with the movement of chemical species and play an important role in most aspects of daily life as well as in many scientific and engineering disciplines. Despite the wide range and the complexity of the applications based on mass transport processes, its mechanisms can simply be highlighted while preparing a cup of tea. After dropping a teabag in water, the emerging tea molecules start to travel and spread inside the whole cup from high to low concentration regions, changing the color of liquid. This phenomenon, called diffusion, is the result of random interactions between molecules and, ultimately, leads to homogeneous concentration throughout the system. With diffusion being a slow process, it is very common to stir the liquid in order to speed up mixing. Advection represents this bulk motion of fluid which carries with it the distribution of tea molecules. For a complete description of mass transport phenomena, a source which account for the production or consumption of species inside the system has to be considered. In this example, the teabag is the place from where the tea molecules are introduced in water. Usually, through sources are modelled the reactions between species, which represents the local mechanisms and kinetics involving electron rearrangements that generates molecule transformations. Ultimately, this translates into changes in the concentration field giving rise to new gradients.

The framework provided by the interplay of these three processes is of great importance not only for preparing a beverage, but also for describing a plethora of phenomena in various scientific disciplines. Examples of studies include evolution of concentration following a reaction [1, 2], weather dynamics [3], environmental transport of contaminants and chemicals achieving pollutant [4], modelling dispersal at active volcanoes [5] and even animal movement in dynamic environments [6].

Of particular concern here are two areas of growing interest and significance: catalytic reactions and mixing of species in microchannels. Catalysis represents the change of the rate of a chemical reaction in the presence of an additional substance that is not consumed during the process. It plays an essential part in industry as the manufacturing of most of the chemical-based materials involves a catalytic stage. Catalysis has started to develop as a scientific discipline at the beginning of the nineteenth century. Louis Thénard was one of the pioneers in this field, identifying metals such as platinum, copper and iron as suitable catalysts in his studies on decomposition of ammonia. An interesting case is represented by gold, which is considered a poor catalyst being chemically inert and the most stable among metals. However, in 1987 it has been noticed that gold nanoparticles (Au NPs) exhibit catalytic behaviour in the process of oxidizing CO into CO_2 [7]. Since then, many studies have shown that, in the nanometer range,

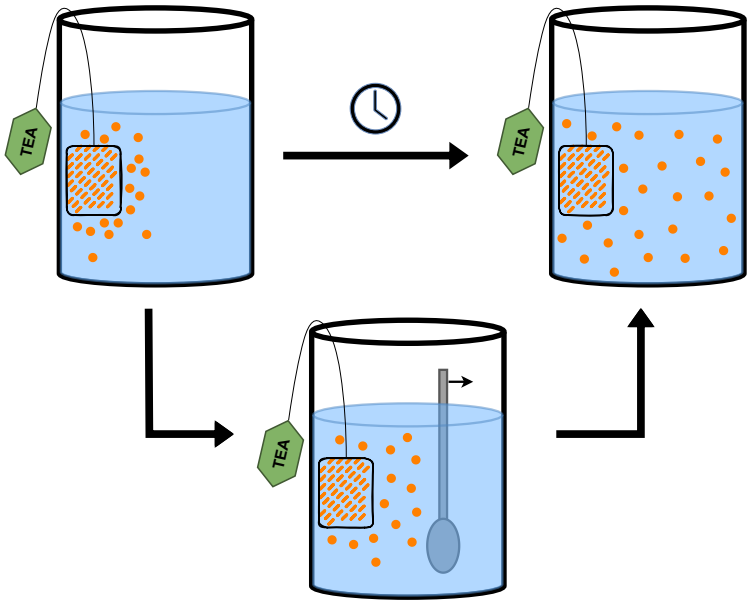

Figure 1.1: Illustration of an advection-diffusion process in a cup of tea. Diffusion is the movement of small tea molecules from higher (teabag) to lower concentration regions and given enough time, it leads to a homogeneous distribution. Stirring represents the advection mechanism, i.e. the bulk motion of fluid, which accelerates the mixing process.

gold becomes a good catalyst [8–10]. Beside their high catalytic performance, gold nanoparticles offer additional advantages such as stability, easy recovery and recyclability, which makes them relevant for applications in many areas, including medicine [11–13], photonics [14], sensors [15–17] and electronics [18, 19].

A characteristic of the nanoparticles is their large total surface area which enhances the catalytic performance. However, due to the large number of particles used in such processes and their active surfaces, they are prone to aggregation, which reduces the surface available for the reaction and decreases the activity. To minimise this effect, two popular solutions have been developed, i.e. stabilising the nanoparticles using ligands and immobilising the particles on solid supports. In the first case, the size [20–22], shape [23] and capping ligands [24] of Au NPs have already been shown to have significant impact on the catalytic performance, influencing the reaction rates. Regarding their size, Suchomel et al.[22] and Fenger et al.[25] have reported that the catalytic activity increases as particles become smaller. However, in most cases the comparison was made using the same quantity of gold for all sizes. This leads to a higher surface

area available in case of smaller radii when the total volume is kept constant, which offers a simple explanation for this effect. One of the very few studies where the size-dependent catalytic activity of Au NPs was analysed in the context of a constant total surface area is the work of Piella et al. [26], which also shows a higher efficiency for smaller radii. The explanation proposed here is based on the chemistry of ligands, i.e. gold atoms are lower coordinated on smaller particles compared to the larger ones. To our knowledge, there has not been any attempt of investigating this phenomenon for the perspective of the changes in the advection-diffusion of the reactant around nanoparticles with different sizes.

The other strategy to avoid Au NPs aggregation, which has no influence on the catalytic activity of their surfaces, is the immobilisation of the nanoparticles on various types of solid supports. The most common choices have been the use of inorganic supports such as metal oxides [27, 28], nanotubes [29] and layered materials like graphene [30], or metal-organic frameworks [31, 32] as hosts for the metal nanoparticles. Recently, the class of polymeric supports, which includes porous polymers [33, 34] and polymer micelles [35] have become an interesting alternative due to their properties which allow simple adjustments to the requirements of a specific reaction process. Schöbel et al. [36] have proposed an efficient teabag-like catalyst system in the form of nonwovens that have a polystyrene-based core and Au NPs-loaded patchy micelles as the shell. One interesting property of this morphology is that the accessibility of the reactants to the surface of the embedded nanoparticles is determined by the swellability of the patches and thus an induction period is observed in the reaction process. Usually, when analysing reaction kinetics that exhibit different stages, each regime is treated separately such that the classical simple reaction rates laws can be applied [37]. However, developing mathematical models specifically tailored for the particularities of a system can offer a better and more accurate insight into its characteristics, i.e. the influence that the patch structure and chemistry have on the catalytic performance [38].

The relevance of mass transport mechanisms in catalysis becomes clearer when studying processes involving synthesis. Complex chemical products are manufactured as the result of a series of catalytic reaction involving simpler initial substances. The traditional way of implementing this is based on a step-by-step approach which requires the isolation and purification of each intermediate product before the next reaction can take place. This leads to high costs, long production time, while also generating large amounts of waste. As an alternative, the cascade approach, where all the chain reactions take place without any additional recovery step, has been developed. Due to the reduced number of operations, smaller quantities of

solvents required and less waste produced, one-pot cascade reactions have received increasing attention in many technological areas [39–41]. The biggest issue of this technique is that some processes use incompatible catalysts (e.g acid and base) that annihilate each other when mixed together [42, 43]. Similar to gold nanoparticles, the Wolf-Lamb-type catalysts can be immobilised on solid supports, a great example being fibers prepared by electrospinning which have already shown their potential [44, 45]. The fibers carrying the catalysts can then be assembled into membranes through which the reactants are flowing. This type of reactor can be modelled as an advection-diffusion-reaction system in order to understand how various parameters and geometries influence the efficiency of the cascade reactions. Previous studies related to this topic have mostly concentrated on diffusion dominated processes [46–48]. Works that include advection are limited to simulations of two dimensional systems with reactive boundaries [49], microchannels [50] and molecular dynamics simulations of spherical catalytic sites [51]. There is currently a lack of computational studies that systematically investigate one-pot cascade reactions and the effect of complex fiber morphologies on the catalytic efficiency of fibrous membranes.

Another topic of particular interest in this thesis is the process of mixing inside microchannels. Microfluidics devices have been a major topic of research in the past decade, driven by the high interest in the lab-on-a-chip technology [52]. These type of devices have had a significant impact on the fields of chemistry, life sciences and bioengineering, with a growing number of applications covering a wide range of processes such as polymerisation [53], synthesis [54], clinical diagnostics [55, 56], drug delivery [57] and bioprinting [58]. Mixing has represented one of the most fundamental and difficult to achieve feature of these systems. The microscale channels generally have low flow rates being characterised by a laminar flow regime with no disruptions between the layers. Therefore, diffusion becomes the main mechanism by which uniformity of concentration is achieved. However, diffusion is a slow process that requires long time to obtain a good mixing and as a result, additional methods of microfluidic mixing must be devised. The progress in development of micromixers has been reviewed in a series of excellent recent articles [59–61]. Increasing the contact area between the mixing species by splitting and folding the streams has emerged to be one of the most efficient means of enhancing the diffusive mixing performance, while being very reliable and easy to implement in microdevices [62]. Furthermore, the geometry of the channel can also play a role, with serpentine microchannels [63] or obstacles on the walls [64] providing a simple way to improve the efficiency. An interesting topic is the addition of microcapsules or cells to the stream, which has significant relevance in the young and evolving field of bioprinting [58]. However, the effect on the concentration distribution generated

by the passage of soft objects inside microchannels is still poorly understood.

Studying all the phenomena presented here requires the advection-diffusion-reaction equation (ADRE) to be solved for each individual system. The availability of complete analytical solutions is usually limited to simple cases and depends on the initial and boundary condition [65]. Thus, the field of computational fluid dynamics is vital for solving mass transport problems and the wide variety of methods that have been invented are well summarised by Krüger et al. [66]. The finite volume method (FVM) is one of the conventional solvers being based on discretising the ADRE and has been often chosen for its simplicity. Alternatively, particle-based methods simulate the behaviour of individual molecules or collections of molecules that form the fluid. First example from this category is the random walk particle tracking (RWPT) [67] which can be fairly easy to implement but requires high computational resources. A better and more popular option is the lattice Boltzmann method (LBM) due to its ability to handle complex systems and its suitability to high performance computing on parallel architectures [68].

This thesis aims to study the interplay of advection diffusion and reaction mechanisms in the context of catalytic processes and microchannel mixing by developing multiple simulation tools. It provides novel insight into the efficiency of flow-through catalytic reactors and the impact produced by the passage of microcapsules inside micromixers. The content of this work is organised as follows.

Chapter 2 introduces the basic theory that describes advection-diffusion-reaction phenomena and a kinetic theory which serves as a foundation for the LBM. In chapter 3, the implementations of three ADRE solvers, i.e. FVM, RWPT and LBM, are presented and their advantages and disadvantages are discussed. Chapter 4 analysis the catalytic behavior of gold nanoparticles. The reaction rates are monitored in relation to changes in the solvent diffusion around particles of various sizes using LBM and RWPT simulations. Additionally, an analytical model for the kinetics of reactions that exhibit an induction period is developed in order to fit the experimental data. Chapter 5 discusses one-pot catalytic cascade reactions. The classical second order kinetics model is extended to account for a delayed start in the second step. Furthermore, the efficiencies for different configurations of flow-through reactors are simulated using LBM. Chapter 6 focuses on the topic of mixing of chemical species inside microchannels. Passive mixing techniques such as parallel lamination and serpentine channel are analysed while deformable microcapsules are flowing through the system. Finally, a summary and an outlook are given in chapter 7.

Chapter 2

Mass transport processes

2. MASS TRANSPORT PROCESSES

Transport phenomena are essential to the universe being the underlying mechanism for any process that involves physical change, starting from something as simple as mixing in hot cup of tea to the existence of life on Earth. They describe the exchange of mass (transport of chemical species), energy (heat transfer) and momentum (fluid dynamics) between different systems. In many cases, these forms of transport occur simultaneously in engineering, meteorology and environmental studies and they share a similar mathematical framework, despite covering diverse topics such as thermodynamics and continuum mechanics [69]. It is possible to describe the transport of mass, momentum or energy using three different scales:

- at macroscopic level, one can study the variation of the quantity of interest (i.e. mass, energy or momentum) for a system due to inputs from the surroundings by analysing the macroscopic balances. However, no insight of the details of the systems can be gained as this offers only a global assessment of the problem, which can be employed as a good starting point in an analysis or when only an overall view is required. Typical lengths at this level are of the order of meters.

- at mesoscopic level the variation of mass, energy or momentum is studied only in a small region of the system using equations that describe the rate of change. This way, it is possible to obtain information about concentration, temperature, velocity and pressure profiles within the system, which offer a deeper understanding of the processes. This level is usually used in the micron to centimeter range.

- at microscopic level individual particles are studied and the molecular structure and intermolecular forces are considered in order to gain a fundamental understanding of the mechanisms of mass, energy and momentum transport. Studies at this level involve lengths in the ranges of about 1 nanometer to 1 micrometer.

Throughout this work, our focus is on processes characterised by mass transport and its interplay with momentum transport phenomena. This chapter introduces two fundamental kinds of transport mechanism, advection and diffusion, which can be be observed in daily life and in many hydrodynamic problems. Given the fact that the physical picture and the mathematical framework of transport by advection and diffusion remain unchanged with respect to the fluid property that is studied [70], in section 2.1 the equations will be derived in a generic form at the macroscopic level and then the particular case for mass transport will be presented. Section 2.2 provides a concise summary of the kinetic theory which can be used to describe fluids at a

mesoscopic scale. Section 2.3 discusses the kinetics of chemical reactions, which influences the mass transport by producing or destroying species.

2.1 Advection-Diffusion fundamentals

Advection represents the transport by bulk motion of a fluid. As matter is moving, the properties associated with it are carried with that motion. A great illustration of this process is the oil spilled in a river which is moving downstream being dragged along with the water. Another example is the movement of the clouds due to the wind.

Diffusion is a less intuitive phenomenon, lacking a macroscopic explanation. For a given finite temperature, molecules show random motion with high velocities over very short distances. This happens even if the average velocity is zero, which makes the medium seem static at the macroscopic level. Brownian motion is a famous example that is driven by this mechanism [71]. It was first described by Robert Brown in 1827 who studied the behavior of fine particles placed on top of a water surface. By being constantly hit by random water molecules, these particles follow Brownian trajectories as shown in Figure 2.1. Almost eighty years later, Einstein [72] and Smoluchowski [73] simultaneously managed to explain this motion and related the mean squared displacement of a particle to a system property, i.e. the diffusion coefficient D, according to

$$\left\langle |\vec{x}(t) - \vec{x}(0)|^2 \right\rangle = 2nDt, \tag{2.1}$$

where $\vec{x}$ is the position of the particle and n is the dimension of the Brownian motion. Considering a set of particles, initially confined to one place, it tends to spread out spontaneously due to the random walk of each individual, which leads to a uniform spatial distribution. Due to this phenomenon, two miscible fluids such as ink and water mix themselves when put together, with both species diffusing until the concentrations are homogeneous throughout the system. Thus, diffusion is the transport of properties via molecular interactions from regions of high content to regions of low content.

Most transport processes can be classified as pure advective, pure diffusive or a combination of both. Being two independent mechanisms, when advection and diffusion act simultaneously, the result may be considered a superposition of the two transports. This property is highlighted in Figure 2.2 by tracking the evolution of the spacial distribution of a set of particles in all three possible scenarios: pure advection, pure diffusion and advection-diffusion. Even though both advection and diffusion occur in fluids, their contributions may not be equally significant.

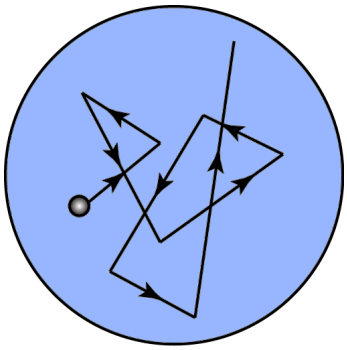

Figure 2.1: Brownian trajectory of a particle at a water surface due to the random collisions with the fluid molecules.

For instance, in a flow close to a stationary wall, the fluid velocity, which drives the advection, approaches zero, thus diffusion becomes the dominant transport mechanism. Similarly, moving away from the boundary, the velocity starts to increase and the advection might become dominant. Additionally, diffusion is usually a slow process when the system considered is large. Equation (2.1) shows that the mean squared displacement increases linearly with time, which means that diffusion is proportional to $\sqrt{t}$. Meanwhile, for a constant velocity $\vec{u}$, advection scales linearly with time since the displacement in this case is $\vec{u}t$. Thus, spacial scale also influences the importance of the transport mechanisms.

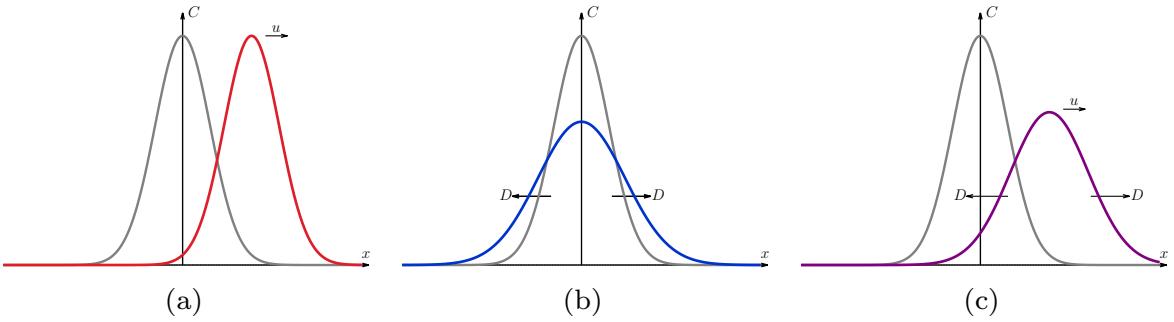

(a) (b) (c)

Figure 2.2: Illustration of the three types of mass transport: (a) pure advection, (b) pure diffusion and (c) advection-diffusion, driven by the advection velocity u and the diffusion coefficient D. The grey curve represents the initial concentration distribution $C(x, t = 0)$, while the three colored curves show the distribution at a later time.

2.1.1 Advection and diffusion fluxes

We start by considering the advection flux of some property X of a fluid. The volume of fluid crossing a unit area of a plane in a unit of time, depends on the velocity $\vec{u}$ of the flow. The advection flux of X is also proportional to the fluid content of that property per unit of volume V, thus its general expression is given by

$$\vec{j}_X^{adv} = \frac{X}{V}\vec{u} \tag{2.2}$$

For the transfer of a substance, X is replaced by the number of particles N of a species carried in the volume V. Additionally, the advection flux of mass becomes

$$\vec{j}_{mass}^{adv} = \rho\vec{u} \tag{2.3}$$

since the mass per volume is just the density ρ.

For the diffusion transport, in order to have a nonzero net flux, a gradient in the property X is required across the surface considered. According to this observation, the diffusion flux can be considered proportional to the gradient in the following form

$$\vec{j}_X^{diff} = -(\textit{diffusivity})\vec{\nabla}\left(\frac{X}{V}\right), \tag{2.4}$$

where diffusivity is the proportionality constant and the minus sign is the result of the flux developing from the high content region to the low content region. Equation (2.4) is the generalisation of Adolf Fick's study of concentrations and fluxes of salt diffusing between two reservoirs. Fick's first law that describes the relation between the diffusive flux and the gradient of the concentration of a species is usually written as [74]

$$\vec{j} = -D\vec{\nabla}C \tag{2.5}$$

where D is the diffusion coefficient or diffusivity and C is the concentration scalar field. The diffusion coefficient is a material property that is usually temperature-dependent and its physical unit is m^2/s.

It should be noted that not all diffusion processes are described by Fick's law (normal diffusion). When the mean squared displacement does not scale linearly with time, the process does not follow Fick's law and is referred to as non-Fickian (anomalous diffusion). However, this behavior is beyond the scope of this work.

2.1.2 Continuity equation

Continuity equation is a stronger, local form of conservation laws stating that a property cannot be created or destroyed and that it has to move by a continuous flow. In the most general form, considering a control volume as shown in Figure 2.3, a conservation statement is described by the balance between the local rate of change of a specific property and the net transport of that property to the region, according to

$$(change) = (in - out). \tag{2.6}$$

When a differential volume is considered, the net transport becomes the negative divergence of fluxes. Thus, the differential form of equation (2.6) can be written as

$$\frac{\partial(stored)}{\partial t} = -\vec{\nabla} \cdot (fluxes) \tag{2.7}$$

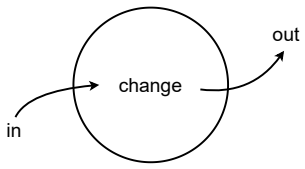

Figure 2.3: Illustration of the conservation principle.

We will now proceed to derive the equation of continuity for the total mass of an incompressible fluid. The transport is initially assumed to be caused only by advection, without considering the species that form the fluid. We consider a two-dimensional volume as displayed in Figure 2.4. Assuming that the system is in the steady state, the mass flowing into the control volume must equal the mass flowing out. To quantify this, the boundary is dived into four surfaces. The rate of mass advected across one face of the control volume is the dot product between the flux $\rho\vec{u}$ and the differential surface area $d\vec{A}$. Since the normal vector of each surface points outwards from the volume, the product is negative when mass is flowing into the region and positive when it is advected out the region. The rates at which that mass is transported through each boundary

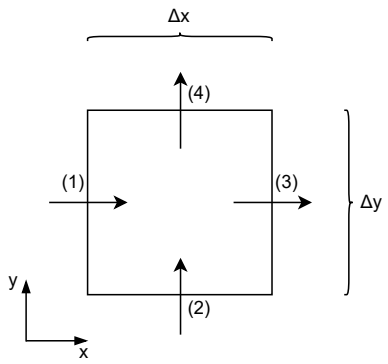

Figure 2.4: Two dimensional flow through a control volume

can be computed as

$$\begin{aligned}(1) &: -(\rho u_x)|_x \, \Delta y \\ (2) &: -(\rho u_y)|_y \, \Delta x \\ (3) &: (\rho u_x)|_{x+\Delta x} \, \Delta y \\ (4) &: (\rho u_y)|_{y+\Delta y} \, \Delta x\end{aligned} \tag{2.8}$$

Assuming that the mass is conserved, the net rate must be zero according to equation (2.6). Therefore, summing all the contributions displayed in (2.8) yields

$$-(\rho u_x)|_x \, \Delta y + -(\rho u_y)|_y \, \Delta x + (\rho u_x)|_{x+\Delta x} \, \Delta y + (\rho u_y)|_{y+\Delta y} \, \Delta x = 0, \tag{2.9}$$

which can be further divided by $(\Delta x \Delta y)$, leading to

$$\frac{(\rho u_x)|_{x+\Delta x} - (\rho u_x)|_x}{\Delta x} + \frac{(\rho u_y)|_{y+\Delta y} - (\rho u_y)|_y}{\Delta y} = 0. \tag{2.10}$$

Reducing the control region to a differential volume by imposing $\Delta x \to 0$ and $\Delta y \to 0$, the differential form of the continuity equation for the steady two dimensional flow is obtained as

$$\frac{\partial(\rho u_x)}{\partial x} + \frac{\partial(\rho u_y)}{\partial y} = 0. \tag{2.11}$$

This equation shows that the increase in advection mass flux through the differential volume in one direction must be compensated by a decrease in the other direction since their sum must be zero in order to have mass conservation. To account for any arbitrary number of dimensions,

equation (2.11) can be rewritten as

$$\vec{\nabla} \cdot (\rho \vec{u}) = 0. \tag{2.12}$$

Next, we expand this model by considering the case when more mass is transported out of the control volume compared to the amount advected in. In mathematical terms, this means that the divergence in equation (2.12) becomes positive. There are two mechanism that can lead to this outcome: the mass stored in the volume decreases over time and mass being created inside the volume. For the time being, we consider only the first scenario which implies that the flow is unsteady. The net rate of mass transport from equation (2.9) must equate the rate of increase of mass inside the volume according to

$$-(\rho u_x)|_x \, \Delta y + -(\rho u_y)|_y \, \Delta x + (\rho u_x)|_{x+\Delta x} \, \Delta y + (\rho u_y)|_{y+\Delta y} \, \Delta x = (\Delta x \Delta y) \frac{\partial \rho}{\partial t}. \tag{2.13}$$

Performing the same division by the volume $(\Delta x \Delta y)$ and taking the limit $\Delta x \to 0$ and $\Delta y \to 0$ yields the differential form of the continuity equation for an unsteady flow in two dimensions

$$\frac{\partial \rho}{\partial t} + \frac{\partial (\rho u_x)}{\partial x} + \frac{\partial (\rho u_y)}{\partial y} = 0. \tag{2.14}$$

Under the assumption of mass conservation and that the only form of fluxes transporting mass is advection, the continuity equation may be generalised to

$$\frac{\partial \rho}{\partial t} + \vec{\nabla} \cdot (\rho \vec{u}) = 0. \tag{2.15}$$

2.1.3 Advection-Diffusion equation

We now focus our attention to the transport of chemical species in a fluid. Compared to the previous case where the property of interest was the mass of the fluid, this time diffusion must be considered as well as advection to track the species. Introducing the diffusive flux given by the Fick's law from equation (2.5) in (2.15), the advection-diffusion equation (ADE) for the concentration of a species in a fluid reads

$$\frac{\partial C}{\partial t} + \vec{\nabla} \cdot (C \vec{u}) = \vec{\nabla} \cdot (D \vec{\nabla} C). \tag{2.16}$$

Although mass is neither created or destroyed, it can suffer changes in terms of its chemical composition. Thus, a species may be produced or consumed through chemical reactions. A source term q, modelling the reaction rates described in section 2.3, can be added to equation (2.16),

thus leading to the advection-diffusion-reaction equation (ADRE) which reads

$$\frac{\partial C}{\partial t} + \vec{\nabla} \cdot (C\vec{u}) = \vec{\nabla} \cdot (D\vec{\nabla}C) + q. \tag{2.17}$$

This equation describes the local change in the concentration C through the three different possible mechanisms:

- advection caused by the flow of the ambient fluid with the velocity $\vec{u}$;
- diffusion driven by the gradient of C according to Fick's law;
- reaction, indicated by the source term q, that locally produces or consumes C.

If the diffusion coefficient D is homogeneous, the ADRE can be further simplified to

$$\frac{\partial C}{\partial t} + \vec{\nabla} \cdot (C\vec{u}) = D\nabla^2 C + q. \tag{2.18}$$

2.2 Kinetic theory

In this section we offer a kinetic description of fluids, which is the foundation for our main simulation method, i.e. the lattice Boltzmann method (section 3.3). Unlike the previous approach used in this chapter to derive the transport equations from the macroscopic picture, we now start from the microscopic scale where the movement of individual particles is tracked. The central role at this level is played by the collisions between the molecules. We first assume that the density of the fluid is sufficiently low so that only binary collisions are considered. This also implies that the time spent colliding is neglectable. In order to avoid treating the microscopical interactions quantum mechanically, kinetic theory operates at a mesoscopic level by using a statistical description of a large number of particles. According to Bohr's correspondence principle, the quantum behaviour of a system is reduced to a classical behavior when the system becomes large enough.

The fundamental variable is the particle distribution function $f(\vec{x}, \vec{\xi}, t)$, which represents the density of particles with the velocity $\vec{\xi}$ at the position $\vec{x}$ and time t. Thus, it has the units $\mathrm{kg} \cdot \mathrm{s}^3/\mathrm{m}^6$. The macroscopic variables can be recovered from the moments of the distribution function. These moments represent the integrals of f weighted with functions of $\vec{\xi}$, over the entire velocity space. As an example, the density is obtained by considering the contribution of

particles having any possible velocity at position $\vec{x}$ and time t as

$$\rho(\vec{x},t) = \int f(\vec{x},\vec{\xi},t)\mathrm{d}^3\xi. \tag{2.19}$$

Similarly, the momentum density can be found as the moment

$$\rho(\vec{x},t)\vec{u}(\vec{x},t) = \int \vec{\xi} f(\vec{x},\vec{\xi},t)\mathrm{d}^3\xi, \tag{2.20}$$

where $\vec{u}$ is the mean velocity.

The multiple collisions between particles tend to even out the distribution of velocities in a system around $\vec{u}$. Therefore, when a gas is left alone for long enough, the distribution function $f(\vec{x},\vec{\xi},t)$ will reach an equilibrium distribution $f^{eq}(\vec{x},\vec{\xi},t)$ that is isotropic in velocity space around $\vec{\xi} = \vec{u}$.

Next we look for the equation that describes the evolution of f in time towards the equilibrium. The total derivative of the distribution function is given by

$$\frac{\mathrm{d}f}{\mathrm{d}t} = \left(\frac{\partial f}{\partial t}\right)\frac{\mathrm{d}t}{\mathrm{d}t} + \left(\frac{\partial f}{\partial x_i}\right)\frac{\mathrm{d}x_i}{\mathrm{d}t} + \left(\frac{\partial f}{\partial \xi_i}\right)\frac{\mathrm{d}\xi_i}{\mathrm{d}t}. \tag{2.21}$$

Analysing the right-hand side, it can be noted that in the first term $\mathrm{d}t/\mathrm{d}t = 1$, in the second term the particle velocity $\mathrm{d}x_i/\mathrm{d}t = \xi_i$ is recovered, while the body force $\mathrm{d}\xi_i/\mathrm{d}t = F_i/\rho$ is present in the last term. Thus, the Boltzmann transport equation is obtained as

$$\frac{\partial f}{\partial t} + \xi_i\frac{\partial f}{\partial x_i} + \frac{F_i}{\rho}\frac{\partial f}{\partial \xi_i} = \Omega(f), \tag{2.22}$$

where $\Omega(f) = \mathrm{d}f/\mathrm{d}t$ represents the total differential. This equation has a similar form to the transport equation as the first two terms describe the advection of f with the velocity ξ. The third term contains the forces that influence ξ, while the right-hand side represents the local redistribution of f due to collisions. This source term $\Omega(f)$ is known as the collision operator. The original collision operator proposed by Boltzmann considers all possible scenarios of binary collisions for any given intermolecular forces and, as a result, has a very complicated form. Later, Bhatnagar, Gross and Krook came up with a simpler version called the BGK operator [75]:

$$\Omega(f) = -\frac{1}{\tau}\left(f - f^{eq}\right). \tag{2.23}$$

Although some accuracy is lost compared to the original operator, equation (2.23) manages

to capture the evolution of the distribution function towards its equilibrium through a single parameter, i.e. the relaxation time τ. This time constant characterises the speed of this equilibration process and is correlated to transport coefficients such as the diffusion coefficient.

Starting from the kinetic theory, it is possible to obtain the macroscopic descriptions of fluid mechanics. We now proceed to show this for the simplest case represented by the continuity equation for the mass of the fluid. Integrating the Boltzmann equation (2.22) over velocity space yields

$$\frac{\partial}{\partial t}\int f \mathrm{d}^3\xi + \frac{\partial}{\partial x_i}\int \xi_i f \mathrm{d}^3\xi + \frac{F_i}{\rho}\int \frac{\partial f}{\partial \xi_i}\mathrm{d}^3\xi = \int \Omega(f)\mathrm{d}^3\xi. \tag{2.24}$$

Using the moments (2.19) and (2.20) that corresponds to the mass density and momentum density, respectively, and assuming that the mass is conserved, the force term and the source term vanishes allowing us to find the same continuity equations from (2.15):

$$\frac{\partial \rho}{\partial t} + \frac{\partial(\rho u_i)}{\partial x_i} = 0. \tag{2.25}$$

This result shows that the mass equation is exact and invariable being independent on the particular form of the distribution function and it also highlights the ability of the Boltzmann equation to describe the macroscopic behavior of a fluid.

2.3 Reaction kinetics

Reaction kinetics represents the study of the rates at which a chemical process occurs. Any chemical process can be broken down into a sequence of one or more single step processes (elementary reactions). In many cases, reactions that are written as a single reaction equation actually consist of a series of elementary steps. In general, an elementary process can be described as a transition between two atomic or molecular states separated by a potential barrier. This potential difference represents the activation energy of the process and determines the rate at which it occurs. The wide variety of chemical species, types of reaction and the associated potential energies results in the timescale required for the fulfilment of chemical reactions to cover many orders of magnitude, from very slow processes (e.g. iron rusting) to extremely fast reactions (e.g. combustion reactions occurring in flames).

The rate of a chemical reaction represents the change in concentration of either reactants or products as a function of time. Considering a generic $aA + bB \rightarrow pP + qQ$ reaction, the rate is

given by

$$\text{rate} = -\frac{1}{a}\frac{\mathrm{d}[A]}{\mathrm{d}t} = -\frac{1}{b}\frac{\mathrm{d}[B]}{\mathrm{d}t} = \frac{1}{p}\frac{\mathrm{d}[P]}{\mathrm{d}t} = \frac{1}{q}\frac{\mathrm{d}[Q]}{\mathrm{d}t}, \tag{2.26}$$

where $[A]$ and $[B]$ are the concentrations of the reactants, $[P]$ and $[Q]$ the concentration of the products and a, b, p, q the stoichiometric coefficients. Note that the negative sign is introduced when the rate is defined using the concentration of a reactant. This is due to the rate of change in this case being negative (reactant is consumed) while the reaction rate needs to be a positive quantity.

The rate law is an equation that relates the rate of a reaction to the concentrations of the chemical species involved. Elementary processes always follow a simple rate law, which takes the form

$$\text{rate} = k[A]^n[B]^m... \tag{2.27}$$

where k is the constant of proportionality between the rate and the concentration of the reactants and is called the rate constant. The power of a particular concentration represents the order of the reaction with respect to that reactant. The overall reaction order is the sum of all the powers. Based on (2.26) and (2.27), it can be deduced that the rate law is a differential equation that describes the rate of change in the concentration with respect to time. If we integrate the rate law, we can obtain an expression for the concentration as a function of time, which is usually the type of measurement performed in an experiment. The first three rate law in terms of complexity are presented in both their differential and integrated form in Table 2.1.

Table 2.1: Differential and integrated form of the rate law for the first three reaction orders.

Reaction	**Order**	**Differential form**	**Integrated form**
$A \rightarrow P$	zeroth	$\frac{\mathrm{d}[A]}{\mathrm{d}t} = -k$	$\frac{[A]}{[A]_0} = -kt$
$A \rightarrow P$	first	$\frac{\mathrm{d}[A]}{\mathrm{d}t} = -k[A]$	$ln\frac{[A]}{[A]_0} = -kt$
$A + B \rightarrow P$	second	$\frac{\mathrm{d}[A]}{\mathrm{d}t} = -k[A][B]$	$ln\frac{[B][A]_0}{[A][B]_0} = ([B]_0 - [A]_0)\,kt$

[ ] = concentration of a species; [ ]$_0$ = initial concentration; k = rate constant.

The main factors that influence the reaction rate are:

- concentration of reactants: as the concentration of reactants increases, so does the likelihood of collisions between reactant molecules;
- temperature: at higher temperatures reactant molecules have more energy which increases the frequency of collisions;

- catalysts: their presence speeds up reactions by lowering the activation energy;
- surface area of a solid reactant: more area for reactants to be in contact;
- pressure of gaseous reactants: raising pressure increases the number of collisions between reactants.

Chapter 3

Simulation methods

Even though the equations that describe the mass transport in a fluid presented in section 2.1 might not seem too complicated, their solutions exhibit complex behavior such that analytical solutions are extremely rare, being available only in some special cases. Potential nonlinearities and the boundary conditions associated with complex shapes make numerical solutions the only option for most fluid problems. This has led to the development of a new field, i.e., computational fluid dynamics (CFD), soon after the electronic computers became available.

There are many methods used for solving fluid flows problems. While some of them are more general, being used for any PDE with minor adaptation for CFD, other methods are specifically tailored for finding fluid solutions. Throughout this work, three methods are employed for simulating advective-diffusive transport of reactive species in hydrodynamic systems. Based on their approach, a wide range of the methods is represented by the ones described in this chapter. Section 3.1 covers the finite volume method which is a "top-down" approach where the macroscopic fluid equations are directly discretised and solved using general-purpose solvers. In contrast, random walk particle tracking (section 3.2) and lattice Boltzmann (section 3.3) can be considered "bottom-up" methods being particle-based solvers where a microscopic or mesoscopic description of the fluid is used.

Although our focus is on solving the ADRE (2.18), we must point out that the term that determines the advection contains the velocity $\vec{u}$ which is externally imposed. This represents the flow field which is usually obtained from solving the Navier-Stokes equation. Since the species concentration does not affect the fluid dynamics, we use a hybrid scheme where a lattice Boltzmann method is used to compute the velocity field for the studied system. Then, the result is used as input for one of the methods that solve the ADRE as described below.

3.1 Finite volume method

Finite volume method (FVM) is one of the conventional numerical methods which take the equation that microscopically describes the system of interest and directly solve it using a method of approximation. It is a method based on the divergence theorem for representing and evaluating partial differential equations in the form of algebraic equations. In FVM, the simulated space is divided into smaller volumes V, which may vary in shape and size throughout the system, allowing for an accurate representation of complex geometries. In the middle of each finite volume, the solution is constructed as an average value within that volume.

By design, FVM is most suited for conservation equations which are characteristic for fluid mechanics. This allows for quantities such as mass, momentum or heat to be perfectly conserved.

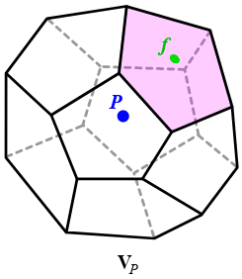

Figure 3.1: Illustration of a generic control volume V_P constructed around the central point P while f denotes the face centre.

To show how this method works, we consider as a starting point the ADE for the concentration field $C(\vec{x}, t)$

$$\frac{\partial C}{\partial t} + \vec{\nabla} \cdot (C\vec{u}) = \vec{\nabla} \cdot (D\vec{\nabla}C) + q, \tag{3.1}$$

where $\vec{u}$ is the flow field, D is the diffusion coefficient and q is a source term. For a generic control volume V_P centred around a point P as illustrated in Figure 3.1, the transport equation can be integrated according to

$$\int_{V_P} \frac{\partial C}{\partial t} \mathrm{d}V + \int_{V_P} \vec{\nabla} \cdot (C\vec{u}) \mathrm{d}V = \int_{V_P} \vec{\nabla} \cdot (D\vec{\nabla}C) \mathrm{d}V + \int_V q \mathrm{d}V. \tag{3.2}$$

Applying the divergence theorem for the terms describing the advection and the diffusion fluxes yields

$$\int_{V_P} \frac{\partial C}{\partial t} \mathrm{d}V + \oint_{\partial V_P} (C\vec{u}) \cdot \mathrm{d}\vec{S} = \oint_{\partial V_P} (D\vec{\nabla}C) \cdot \mathrm{d}\vec{S} + \int_V q \mathrm{d}V, \tag{3.3}$$

where ∂V_P is the surface enclosing the volume V_P and $\mathrm{d}\vec{S}$ is the infinitesimal surface normal element. This step is central to the FVM and highlights the conservation law which states that the sum of all sources and sinks of the field in a region is equal to the net flux across the volume's boundary. By splitting the domain into surfaces f, equation (3.3) can be written as

$$\int_{V_P} \frac{\partial C}{\partial t} \mathrm{d}V + \sum_f \left[\int_f (C\vec{u}) \cdot \mathrm{d}\vec{S} \right] = \sum_f \left[\int_f (D\vec{\nabla}C) \cdot \mathrm{d}\vec{A} \right] + \bar{q} V_P, \tag{3.4}$$

with the additional step of using the average value $\bar{q}$ of the local source term, which is exact if q is either constant or varies linearly within the control volume.

Up to this point, no approximations were introduced, so equation (3.4) is exact if the finite volumes V_P perfectly fit the total volume of the system. The difficulty is represented by the two

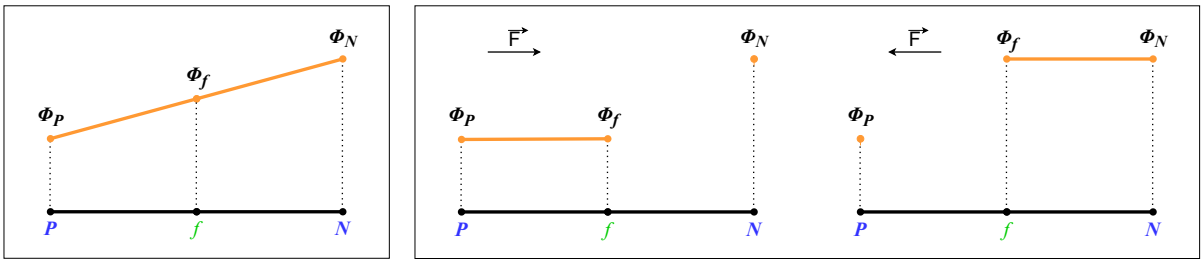

(a) (b)

Figure 3.2: Illustration of (a) the linear interpolation scheme and (b) the upwind scheme used for computing the value of a variable Φ at the interface f between the centres P and N of two adjacent volume elements.

surface integrals which cannot be computed due to the unknown values of the fluxes throughout the surfaces f. This can be overcome by approximating the integrants using the mid point rule, which is second order accurate, yielding

$$\int_{V_P} \frac{\partial C}{\partial t} \mathrm{d}V + \sum_f \left[(C\vec{u})_f \cdot \vec{S}_f \right] = \sum_f \left[(D\vec{\nabla} C)_f \cdot \vec{S}_f \right] + \bar{q} V_P, \tag{3.5}$$

where $\vec{S}_f$ is the face area vector. Given the fact that all variables are evaluated and stored in the centres P, the averages that are assigned at f are computed by some form of interpolation from the central values of the control volumes that are separated by that surface. Here we only present two simple methods that we have employed for our FVM implementation. First one is the central differencing scheme shown in Figure 3.2(a) where a generic quantity Φ is computed at the interface f by a linear interpolation

$$\Phi_f = \frac{|fN|}{|PN|} \Phi_P + \left(1 - \frac{|fN|}{|PN|} \right) \Phi_N. \tag{3.6}$$

This method is second order accurate and was used for computing the magnitude of velocities and diffusive fluxes on the surfaces f. However, by introducing the advective flux, this method can lead to oscillatory solutions in some scenarios, which may cause unphysical behavior [76]. This is mostly because the solution is not bounded by the boundary values. Thus, an upwind scheme was chosen for the advective flux. As described in Figure 3.2(b), the face values are computed as

$$\Phi_f = \begin{cases} \Phi_P, & \text{if } \vec{F} \geq 0 \\ \Phi_N, & \text{if } \vec{F} < 0 \end{cases}, \tag{3.7}$$

where $\vec{F}$ shows the direction of the flux. While this method solves the problems with the oscillations by being bounded, it is only first order accurate and, as a result, it introduces some amount of artificial diffusion.

After the spatial discretization is completed, we can proceed with the temporal discretization which requires additional approximation. For this process we employ the Euler approximation of a derivative. Given the definition, the derivative of C with respect to t is the slope of the curve over an infinitesimal interval, which, in an approximation, can be extended to the finite interval Δt according to

$$\frac{\partial C(t)}{\partial t} = \lim_{\Delta t \to 0} \frac{C(t+\Delta t) - C(t)}{\Delta t} \approx \frac{C(t+\Delta t) - C(t)}{\Delta t}. \tag{3.8}$$

Obviously, to increase the accuracy, Δt has to be closer to the infinitesimal definition. Moreover, the choice of the interval has to be tailored according to the solution itself: a system that varies fast requires a smaller value of Δt to record its full behavior compared to a slowly varying one.

The main advantage of finite volume in CFD lies in its simple principle. The use of control volumes makes it fundamentally conservative such that the quantity of interest, which in this case is the concentration, is conserved throughout the whole domain for a closed system. Another advantage is that FVM is easily formulated to allow for irregular meshes. This leads to a better representation of complex geometries and makes it possible to increase the resolution in the regions of high interest by splitting it up into finer volumes.

On the other hand, generating irregular grids that accurately captures the geometry of the system may be itself a difficult task. Another downside is that FVM become more cumbersome when increased accuracy is sought through higher-order interpolation schemes coupled with unstructured mashes [77].

3.2 Random walk particle tracking method

In contrast to the conventional solvers, particle-based methods model the fluid through particles, which may correspond to atoms, molecules, collections or even distributions of molecules. RWPT is fundamentally a simple microscopic method which, as the name suggests, tracks the position of particles throughout the continuous space of a system.

The movement of a particle at a position $\vec{x}(t)$, that is being advected by a flow field $\vec{u}\left(\vec{x}(t)\right)$ and also diffuses, is given by the Langevin equation [78]

$$\frac{\mathrm{d}\vec{x}(t)}{\mathrm{d}t} = \vec{u}\left(\vec{x}(t)\right) + \sqrt{2nD}\vec{\xi}(t), \tag{3.9}$$

where D is the diffusion coefficient, n represents the dimension of the motion and $\vec{\xi}(t)$ is a vectorial white noise characterised by $< \vec{\xi}(t) >= \vec{0}$. Perez et al. [67] have shown that the ADRE (2.18) is recovered starting from this description of an individual particle. Thus, based on this equivalence, the evolution of the concentration of a species is studied by tracking a large number of non-interacting particles that obey the Langevin model.

For the numerical implementation, equation (3.9) is discretized using the Euler scheme as

$$\vec{x}(t + \Delta t) = \vec{x}(t) + \vec{u}\left(\vec{x}(t)\right) \Delta t + \sqrt{2nD\Delta t}\vec{\xi}(t). \tag{3.10}$$

The displacement is a superposition of a deterministic (advection) and a stochastic (diffusion) component. At any time step, each particle is propagated through the medium using the velocity field obtained from the solution of the external NS equation to simulate advection and a Brownian random displacement is added to model diffusion. In our studies, RWPT is used more for comparison to check the main numerical method, thus, for simplicity, we restrict its application only to 2D systems. The externally imposed velocity $\vec{u}$ is obtained by applying a bilinear interpolation to a discrete flow field obtained using a grid-based solver. The length of the diffusion step is considered constant in time and has the value computed from the mean squared displacement (2.1) as $|\vec{x}(t + \Delta t) - \vec{x}(t)| = \sqrt{4D\Delta t}$, while the direction is randomly selected each time. The particle position is then updated by the Euler integration with $\Delta t = 0.5$.

We have employed RWPT to study systems where a solvent would perform a first order reaction only in the presence of a catalyst that is immobilised on a solid support. To model this reaction, a thin reactive zone is considered around the substrate and every particle within that region has a probability to react during a time step given by $k\Delta t$, with the typical values $k\Delta t \ll 1$. The collision between a particle and the solid support is considered elastic, such that the normal component of the particle velocity is inverted while the tangential component remains unchanged.

The main advantage of RWPT over FVM is that, by avoiding to solve the transport equation directly, it is virtually free of numerical dispersion and artificial oscillations, and therefore it is also free of negative concentrations and mass loss. This approach also allows for high parallelization of the code due to the particles not interacting one with another. The mesh used for computing the concentration of a species by averaging the number of particles from a region of the system, is independent of the one chosen to solve the hydrodynamics, which makes the resolution customizable such that point or linear sources can be better represented.

On the other hand, this method requires the total number of particles used to be larger

enough in order to have an accurate concentration mesh. If too few particles are released in a particle-tracking experiment, it is possible that the trajectories are polluted by statistical outliers and do not satisfactorily represent the desired ensemble average, which may lead to erroneous conclusions. Regarding the optimal number of particles to be used in a simulation, there is no general answer. Thus, for each system, some tests have to be done by repeating the simulation for an increasing number of particles until the concentration will stop fluctuating. Even so, the solution might not be smooth due to the stochastic nature of the diffusive contribution. Opting to increase the number of particles and to decrease the time step to improve the results leads to a significant increase of computational time and memory.

3.3 Lattice Boltzmann method

In section 2.2 we have shown that while the Boltzmann equation describes the dynamics of a gas at a mesoscopic level, it leads to the equations of fluid mechanics on the macroscopic scale. Thus, by solving the Boltzmann equation for a given problem, it is possible to obtain a solution to a macroscopic equation, such as NSE or ADRE, for the same system. The fundamental variable of the kinetic description of a fluid, the distribution function $f\left(\vec{x}, \vec{\xi}, t\right)$ depends on seven parameters corresponding to the physical space, velocity space and time, which makes the Boltzmann equation (2.22) even more difficult to solve analytically than the ADRE (2.18) for instance. However, trying to solve it numerically turns out to be very simple to implement and to optimise for parallel computing. This is a consequence of the fact that the moments of the Boltzmann equation lead to the equations for mass or momentum conservation so, in order to get the correct macroscopic behavior, a lot of the underlying physics is irrelevant.

Inspired by the original lattice gas model [79], the Lattice Boltzmann Method (LBM) tracks the distribution of particles over a discretized space and time domain with a resolution Δx and Δt, respectively. Although many sets of units can be chosen, usually the artificial lattice units where $\Delta x = 1$ and $\Delta t = 1$, are preferred. This allows for simple conversion of quantities to physical units and, to ensure that the same phenomenon described in other units is simulated, one has to check that the relevant dimensionless numbers (e.g. Re, Pe) remain constant from one system to another. The velocity space is also discretized and many velocity sets tailored for different purposes exist. They are represented as DdQq, where d is the number of spatial dimensions covered by the velocity set and q is the number of velocities. Choosing to increase the number of velocities results in improved accuracy but it also requires more computational resources, so the right balance may vary from one case to another. In order to make sure that

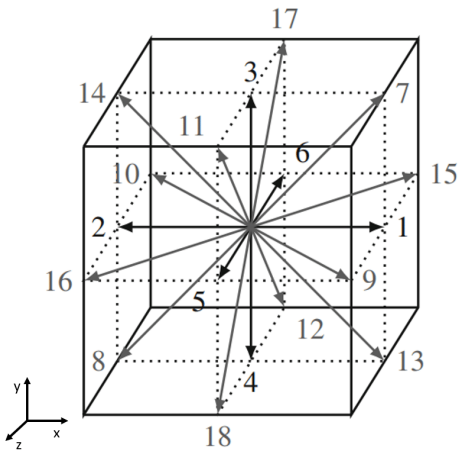

Figure 3.3: D3Q19 velocity set. The rest velocity $\vec{c}_0 = \vec{0}$ is not displayed.

the desired physics is captured, while the number of velocities is kept at a minimum, we opt for D3Q19 which is widely regarded as a good compromise for laminar flows (cf. section 3.4.7 in [66]). As shown in Figure 3.3, the velocities connect neighbouring nodes of the regular grid, thus preventing particles from ending up somewhere between them. Additionally, each velocity has a weight w_i, such that $\sum_i w_i = 1$ and $\sum_i w_i \vec{c}_i = 0$. More details about the D3Q19 velocity set are provided in table 3.1.

Table 3.1: Properties of the D3Q19 velocity set illustrated in Fig 3.3.

Number i	**Velocity** $\vec{c}_i$	**Length** $\lvert\vec{c}_i\rvert$	**Weight** w_i
0	(0, 0, 0)	0	1/3
1..6	(±1, 0, 0), (0, ±1, 0), (0, 0, ±1)	1	1/18
7..19	(±1, ±1, 0), (±1, 0, ±1), (0, ±1, ±1)	$1/\sqrt{2}$	1/36

The velocity sets are also characterised by a constant c_s representing the isothermal model's speed of sound (cf. section 12.1 in [66]). In most cases, including D3Q19, its expresion is given by

$$c_s^2 = \frac{1}{3}\frac{\Delta x^2}{\Delta t^2}. \tag{3.11}$$

Discretising the Boltzmann equation (2.22) in physical space, velocity space and time leads to the lattice Boltzmann equation (LBE)

$$f_i\left(\vec{x} + \vec{c}_i \Delta t, t + \Delta t\right) = f_i\left(\vec{x}, t\right) + \Omega_i\left(\vec{x}, t\right). \tag{3.12}$$

This shows that the discrete-velocity distribution of particles $f_i(\vec{x},t)$, also called particle population and representing the density of particles with velocity $\vec{c}_i$, move from a lattice node at $\vec{x}$ to a neighbouring point $\vec{x}+\vec{c}_i\Delta t$ after one time step Δt. The collision operator Ω_i is responsible for redistributing particles between the populations at each site. Using the BGK operator (2.23), relaxation of distributions towards the equilibrium f_i^{eq}, at a rate given by the relaxation time τ, takes the form

$$\Omega_i(f) = -\frac{f_i - f_i^{eq}}{\tau}\Delta t. \tag{3.13}$$

Thus, the LBE (3.12) becomes

$$f_i\left(\vec{x}+\vec{c}_i\Delta t, t+\Delta t\right) = f_i\left(\vec{x},t\right) - \frac{\Delta t}{\tau}\left(f_i(\vec{x},t) - f_i^{\mathrm{eq}}\right). \tag{3.14}$$

This equation can be separated into two-step scheme used to transport the particles throughout the system. First the collision (relaxation) is performed according to

$$f_i^*(\vec{x},t) = f_i(\vec{x},t) - \frac{\Delta t}{\tau}\left(f_i(\vec{x},t) - f_i^{\mathrm{eq}}(\vec{x},t)\right), \tag{3.15}$$

where f_i^* denotes the population after relaxation. The second step is the streaming (propagation) of the new distribution functions to neighbouring nodes that the corresponding velocity points to

$$f_i(\vec{x}+\vec{c}_i\Delta t, t+\Delta t) = f_i^*(\vec{x},t). \tag{3.16}$$

After completion, one time step has elapsed and the macroscopic moments, such as density or concentration, are computed from $f_i(\vec{x},t)$ (as described in 3.3.1 and 3.3.2). The operations are repeated until the last time step or convergence has been reached.

A major advantage of LBM is its fundamental implementation simplicity by being based on the Boltzmann equation, in contrast with conventional methods which rely on the more complex equations of fluid mechanics. Moreover, the detail in LBM is the particle description within each node, such that the interactions between nodes consist of simple, linear operations, while the local collisions require the heavier computations. This makes LBM suitable for high-performance computing on parallel architectures and more flexible to be adapted to particular cases compared with most methods [68].

Until this point the general characteristics of LBM have been presented. Next, we first offer a short description of its implementation for a Navier-Stokes solver that we have employed to generate the flow field and then, we introduce the LBM for ADRE that we have developed and

used for simulating the actual transport of species.

3.3.1 Lattice-Boltzmann for Navier-Stokes equation

An incompressible flow is governed by the Navier-Stokes equation (NSE)

$$\rho \frac{\mathrm{D}\vec{u}}{\mathrm{D}t} = -\nabla p + \eta \nabla^2 \vec{u} + \vec{F}, \tag{3.17}$$

where ρ is the density of the fluid, $\vec{u}$ is the flow velocity, p is the pressure, η is the dynamic viscosity and $\vec{F}$ is the external body force. The Chapman-Enskog analysis shows that the Boltzmann equation leads to fluid behavior as described by the Navier-Stokes equation [66, 80]. To offer a brief introduction to the LBM for NSE we will look at how the properties of the fluid are linked to the LB concepts presented.

The NSE involves two conserved quantities, density and momentum density, that are represented in LBM as

$$\begin{aligned} \rho(\vec{x}, t) &= \sum_i f_i(\vec{x}, t) \\ \rho\vec{u}(\vec{x}, t) &= \sum_i \vec{c}_i f_i(\vec{x}, t). \end{aligned} \tag{3.18}$$

For the equilibrium distribution, it has been shown that a good stability is acquired through the Taylor expansion of the Maxwell-Boltzmann equilibrium distribution function up to second order [81]

$$f_i^{\mathrm{eq}}(\vec{x}, t) = w_i \rho \left(1 + \frac{\vec{u} \cdot \vec{c}_i}{c_s^2} + \frac{(\vec{u} \cdot \vec{c}_i)^2}{2c_s^4} - \frac{\vec{u} \cdot \vec{u}}{2c_s^2} \right), \tag{3.19}$$

that depends only on the local density and the local fluid velocity. These quantities are computed using the local populations f_i according to equations (3.18), with the velocity found as $\vec{u}(\vec{x}, t) = \rho\vec{u}(\vec{x}, t)/\rho(\vec{x}, t)$.

The relaxation time, which determines the rate of equilibration of the distributions, is set via the macroscopic kinematic viscosity of the fluid as

$$\nu = c_s^2 \left(\tau - \frac{\Delta t}{2} \right). \tag{3.20}$$

Starting from this basic concepts, the free software package ESPResSo [82] has been developed to solve NSE. Thus, we have used it to simulate the flow for each of our studies, in order to get the velocity field required for advection-diffusion problems. To produce a flow, a pressure gradient from one end of the system to another is required. This is implemented as body force

f acting on every lattice node. Setting the boundaries of the system as periodic, the velocity profile develops with each time step until convergence is reached.

Throughout our studies, a large variety of geometries are considered. Implementing them in ESPResSo is quite straightforward: individual nodes of the lattice are set to be solid nodes, i.e. populations cannot end up there, such that the shape is modeled into the grid. At these sites, a bounce-back boundary condition ensures the no-slip condition (chapter 5 in [66]).

3.3.2 Lattice-Boltzmann for Advection-Diffusion-Reaction equation

The LBM is also a powerful method to simulate systems with coupled fluid dynamics and diffusion, therefore we have developed a separate LBM-based solver for ADRE to compute the concentration fields of various species. The NSE and ADRE are very similar, with the former being viewed as an ADE for the fluid momentum density $\rho\vec{u}$. Thus, the lattice Boltzmann equation (3.12) is easily adapted to advection-diffusion processes in the form

$$g_i(\vec{x} + \vec{c}_i\Delta t, t + \Delta t) - g_i(\vec{x}, t) = \Omega_i(\vec{x}, t) + Q_i(\vec{x}, t), \tag{3.21}$$

with g_i denoting the populations to distinguish from the fluid model and Q_i being the source term. The BGK collision operator

$$\Omega_i(\vec{x}, t) = -\frac{1}{\tau_g}\left(g_i(\vec{x}, t) - g_i^{\mathrm{eq}}(\vec{x}, t)\right), \tag{3.22}$$

gives the diffusion coefficient D through the relaxation time τ_g as

$$D = c_s^2\left(\tau_g - \frac{\Delta t}{2}\right). \tag{3.23}$$

Unlike the LBM for NSE, the advcetion-diffusion implementation has only one conserved quantity, the concentration C, which is defined in terms of the distribution function by

$$C = \sum_i g_i. \tag{3.24}$$

The velocity $\vec{u}$ is externally imposed, being provided as the solution of the NSE for the same system.

The equilibrium distribution that is linear in C, but quadratic with respect to the velocity,

and has the form [83]

$$g_i^{\mathrm{eq}} = w_i C \left(1 + \frac{\vec{c}_i \cdot \vec{u}}{c_s^2} + \frac{(\vec{c}_i \cdot \vec{u})^2}{2c_s^4} - \frac{\vec{u} \cdot \vec{u}}{2c_s^2}\right), \tag{3.25}$$

offers good accuracy and convergence.

Source term

Through the source term, it is possible to model chemical reactions which produce or consume species. We consider an elementary first order reaction $A \rightarrow B$ with the rate constant k as described in section 2.3. Since there are two species, A and B, each is characterised by its own LBE. Assuming that they are independent with respect to advection and diffusion, the only difference between the two equations lies in the source terms Q_i^A and Q_i^B, accounting for the consumption of A and production of B respectively. The the macroscopical quantity k is introduced in the discretized source terms in the form [84–86]

$$\begin{aligned} Q_i^{\mathrm{A}} &= -k\Delta t w_i C_{\mathrm{A}} \\ Q_i^{\mathrm{B}} &= +k\Delta t w_i C_{\mathrm{A}} \end{aligned} \tag{3.26}$$

As our aim in our studies is to model a surface-catalytic reaction, we use (3.26) only for those populations that stream into a reactive boundary node. For all others, we set $Q_i^{A,B} = 0$.

Boundary conditions and flux computation

In advection-diffusion processes, if the concentration field cannot penetrate a boundary, the normal flux of C must be zero. However, unlike in fluid dynamics where the velocity vanishes next to a wall, the concentration along a boundary can vary generating a tangential flux. This behavior can be recovered from the anti-bounce-back scheme (cf. section 8.5.2 in [87]) which, for a node $\vec{x}_b$ next to a stationary wall, reads

$$g_{\bar{i}}\left(\vec{x}_{\mathrm{b}}, t + \Delta t\right) = -g_i^*\left(\vec{x}_{\mathrm{b}}, t\right) + 2w_i C_w \tag{3.27}$$

where $g_{\bar{i}}$ is the population streaming away from the boundary, g_i^* the post-collision population streaming towards the wall and C_w is the imposed wall concentration.

Another type of boundary condition is to specify a normal gradient. Neumann boundary conditions are useful for the systems where the concentration does not change along the outflow direction at the outlet. This can be transformed into a Dirichlet boundary condition by setting

$C_w = C_b$ in equation (3.27), where C_b is the concentration of the node that is just before the outlet. In practice, this can be implemented by copying the post collision populations from the plane in front of the outlet to the outlet plane before propagation.

To compute the flux of a species, we consider a plane perpendicular to the flow direction. The difference between all populations that cross this plane streaming along the flow and those streaming in the opposite direction is computed for each node and subsequently averaged across all nodes.

Validation

Advection-Diffusion of a Gaussian Hill

We consider the diffusion and advection of a species in a uniform velocity field $\vec{u}$ on a 2D domain. Starting with a Gaussian concentration profile with the width σ_0 given by

$$C\left(\vec{x}, t=0\right) = C_0 \exp\left(-\frac{\left(\vec{x}-\vec{x_0}\right)^2}{2\sigma_0^2}\right), \tag{3.28}$$

the numerical results can then be compared to the analytical solution [87]

$$C\left(\vec{x}, t\right) = \frac{\sigma_0^2}{\sigma_0^2+\sigma_D^2} C_0 \exp\left(-\frac{\left(\vec{x}-\vec{x_0}-\vec{u}t\right)^2}{2\left(\sigma_0^2+\sigma_D^2\right)}\right), \tag{3.29}$$

where $\sigma_D^2 = 2Dt$. For our LBM simulations, we set the initial concentration $C_0 = 1$ and place the Gaussian hill with the width $\sigma_0 = \Delta x$ in the center of a $100 \times 1 \times 100$ simulation box. As in most of our simulations, we use here $\Delta x = 1$, $\Delta t = 1$ and $\tau_g = \Delta t$ which offers the best stability. Replacing these values in equation (3.23) results in a diffusion coefficient $D = 0.1666$.

First, we consider only the diffusive regime ($\mathrm{Pe} = 0$) by choosing $\vec{u} = \vec{0}$. Figure 3.4 illustrates that our implementation reproduces the analytical results and the small difference between the two does not increase over time.

By introducing a velocity $\vec{u} = (0.1, 0.1)\Delta x/\Delta t$, the previous profile starts to shift. Again, a very good agreement between our simulations and the theoretical results is achieved, as seen in Figure 3.5.

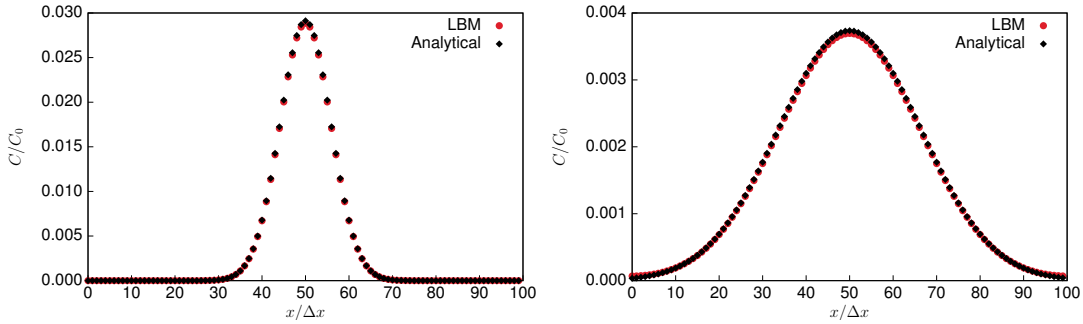

Figure 3.4: Concentration profile of the Gaussian hill in the pure diffusion regime at (a) $t = 100\Delta t$ and (b) $t = 800\Delta t$.

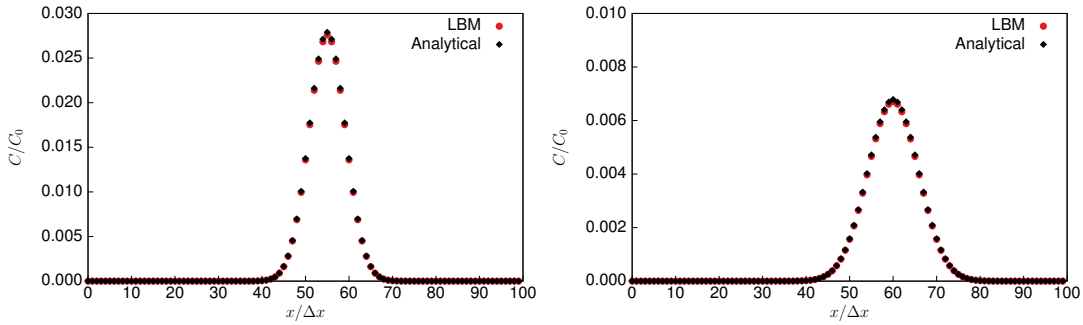

Figure 3.5: Concentration profile of the Gaussian hill in the advection-diffusion regime at (a) $t = 50\Delta t$ and (b) $t = 100\Delta t$.

Advection-diffusion in a microchannel

A more challenging benchmark problem than the Gaussian hill is to replicate the three regimes of dispersion for a point discharge of tracer particles in laminar pipe flow, as described in [88]. Starting from a δ-function initial concentration at the center of the pipe, the moments of the longitudinal distribution of the tracer, $M_n(t)$, can be computed according to equation (1.5) of [88]. The width of the distribution is then defined as

$$\sigma(t) = \sqrt{M_2(t) - M_1^2(t)}. \tag{3.30}$$

Analyzing its time dependency reveals the three stages of longitudinal dispersion. In the beginning, Fickian diffusion dominates ($\sigma \sim \sqrt{2D_{\text{Latini}}t}$), followed by the anomalous regime where the width scales superdiffusively ($\sigma \sim \sqrt{8/3}D_{\text{Latini}}t^2$). Finally, at large times, the flow enters the Taylor

regime where the width scales diffusively again ($\sigma \sim \sqrt{2D^{\text{eff}}_{\text{Latini}}t}$), but with a larger diffusion coefficient $D^{\text{eff}}_{\text{Latini}} = \frac{1}{192D_{\text{Latini}}+D_{\text{Latini}}}$, where D_{Latini} is the dimensionless diffusion coefficient.

A $20000 \times 123 \times 123$ grid was used to model a pipe with a radius $R = 60$. The centerline velocity of the flow was set to $U_0 = 0.4$ and a relaxation time $\tau = \Delta t$ was used as above, thus fixing the dimensionless diffusion coefficient $D_{\text{Latini}} = \frac{D}{RU_0} = 6.94 \times 10^{-3}$. Computing the width of the distribution σ as a function of time, shows a very good agreement with the theoretical values especially for the diffusive and Taylor regimes (Figure 3.6). In order to obtain a clear anomalous regime, a very large lattice must be used which requires a lot of memory. The alternative would be to set the relaxation time close to $\tau = 0.5\Delta t$, but that can lead to negative populations and therefore it is avoided here.

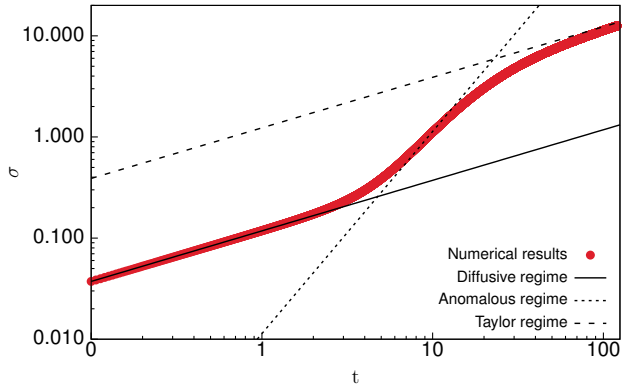

Figure 3.6: The three stages of longitudinal dispersion reproduced by the numerical model with $D_{Latini} = 6.94 \times 10^{-3}$.

Homogeneous reaction

We consider a homogeneous distribution of a species A in a periodic $50 \times 50 \times 50$ system that performs a first-order $A \rightarrow B$ reaction. The well known rate law $C_A(t) = e^{-kt}C_A(0)$ is compared to the results obtained using the linear source term implemented in LBM (cf. equation (3.26)) and RWPT (cf. section 3.2). Figure 3.7 shows that our assumed form matches very well the theoretical model in the low k regime and that for higher values a good compromise between speed and accuracy can be achieved by setting the time step $\Delta t = 0.5$ for the particle based model. The LBM model with $\Delta t = 1$ decays to zero instantaneously as expected for $k = 1$. However, in all our studies, we only consider surface-reaction sites that represent only a very small fraction of the whole system. Therefore, the inaccuracy introduced in LBM for large

reaction rate constants is less significant than here. Moreover, throughout our investigations, we also provide comparisons with RWPT which almost always show a good agreement.

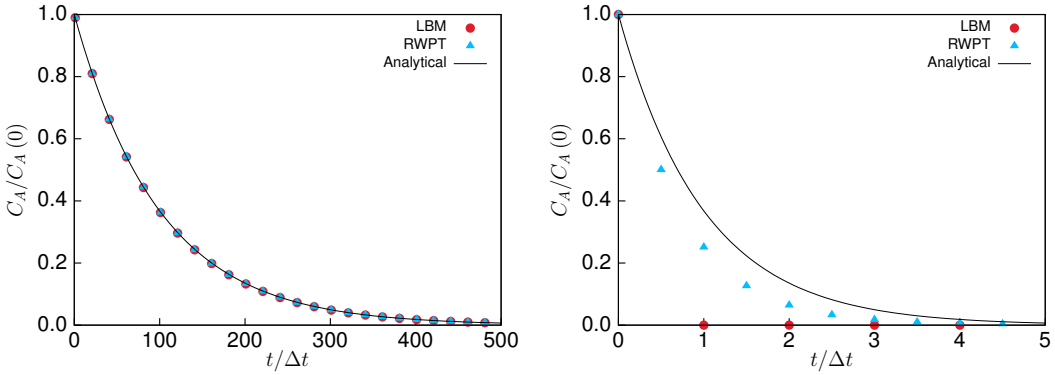

Figure 3.7: Conversion curves for a first-order homogeneous reaction with the reaction rate constants (a) $k = 0.01$ and (b) $k = 1$.

Chapter 4

Kinetic studies on catalytic behavior of gold nanoparticles using first and pseudo-first order reaction models

Bulk gold is chemically inert being the most stable among metals and is generally regarded as a poor catalyst. However, when the size of the particles is reduced to the nanometer range, the gold nanoparticles (Au NPs) become surprisingly active [8–10]. The first major discovery of the catalytic activity of Au NPs dates back to 1987 and highlights their potency to oxidize CO into CO_2 even at low temperatures [7]. Starting from this initial reaction which led to the development of closely related practical applications (e.g. gas masks), the high catalytic activity of Au NPs has generated significant interest in many other areas such as biomedical applications [11–13], sensors [15–17] and electronics [18, 19]. Other advantages of Au NPs that make them attractive for the industrial usage include simple purification process, stability, easy recovery and recyclability. As a result, significant steps towards achieving a more sustainable chemical industry [89] were made once several important Au NP-catalyzed processes were also developed, such as the aerobic oxidation of methanol to the important chemical methyl formate [90] and the production of vinyl acetate and vinyl chloride, which are then used for the synthesis of polymers [91].

A particularity of catalysis involving NPs is represented by their high active surface area. This is a vital morphological characteristic for reaching a good catalytic performance, but, at the same time, it increases the likelihood of NPs aggregating, which in turn will result in a loss of surface, and hence a reduced activity. To overcome this, two major approaches exist, i.e., using ligands for NP stabilisation and immobilization of NPs on a solid support, each of these methods will serve as a base for a different study of the catalytic process in this chapter. Section 4.1 focuses on the influence of the size of polyvinylpyrrolidone (PVP) conjugated Au NPs on the catalytic activity from the perspective of the advection-diffusion processes that the reactant undergoes. In Section 4.2 we analyse the reaction kinetics of a "tea-bag"-like catalyst system where the Au NPs are embedded in hybrid nonwovens and we propose a novel analytical model to fit the experimentally observed catalytic activity.

We have published parts of the following two sections in *Advanced Materials Interfaces* **9**, 2100867 [92] and *Nanoscale Adv.* **2**, 438 [38], respectively.

4.1 Size dependent catalytic activities of gold nanoparticle

Previous studies regarding the size [25, 26, 93], shape [23] and capping ligands [24] of Au NPs show that they play important roles in catalytic activities and determine the reaction rates. Most of the research on the influence of the size of Au NPs has focused on the 4-nitrophenol reductive reaction and it has been shown that smaller particles have a higher activity compared to larger particles due to their higher ratio of surface area to volume. However, there is only a very limited

amount of studies on this topic where various particle diameters were used while keeping the total surface area constant. One of the first observations is attributed to Sau et al. [20] who noted a decrease of the reaction rate with the increase of the diameter of the NPs. Similarly, Piella et al. [26] found the same general trend except for sizes below 13 nm, where it reverted, indicating that smaller particles have less efficient catalytic activity. This unexpected non-monotonic behavior has been attributed to a couple of chemical properties specific to both the NPs and the reactant, such as a less efficient electronic transfer to the catalytic Au site for surfaces smaller than a threshold value [25], as well as possible surface degradation of Au NPs which significantly hinders the accessibility of reactant and, therefore, their catalytic performance [94].

In this section we try to provide insight into the influence of the size of Au NPs on their catalytic activity by investigating the impact of the advection-diffusion effects of the reactants on this process using different simulation methods. Furthermore, we consider the changes in motion that a particle of reactant undergoes near the surfaces of NPs where the diffusion becomes anisotropic. The numerical results are then compared to the experimental findings from the catalysis of 4-nitrophenol reductive reaction in the presence of sodium borohydride ($NaBH_4$) using Au NPs [92].

4.1.1 System description

For this study we consider two different systems with either one large or two small nanoparticles surrounded by solvent containing an initially homogeneous concentration of the reactant A (nitrophenol). The first case, illustrated in Figure 4.1(a), consists of a single sphere with a radius $R = 21$ while Figure 4.1(b) shows the system with two spheres, each having a radius $R = 15$. The values of the radii were chosen such that the total surface area is identical. In both cases the simulation box size is $100 \times 180 \times 100$ and periodic boundary conditions are assumed. The methods used for simulating these systems are LBM and RWPT. An advantage of using both of them is represented by the fact that any effect generated by the discretization of the spheres on a grid in the first case, should be noticed when compared with the results from RWPT where space is continuous.

The reaction used as a model for this study is the conversion of nitrophenol (A) into aminophenol (B) in the presence of the solvent $NaBH_4$ and the Au NPs. Given the fact that $NaBH_4$ is available in excess, we assume a first order $A \rightarrow B$ reaction taking place when the reactant is in the immediate proximity to the surface of the NPs. We assign to the reaction rate constant the value $k = 0.1$ which should provide a good accuracy for our models (cf. Figure 3.7).

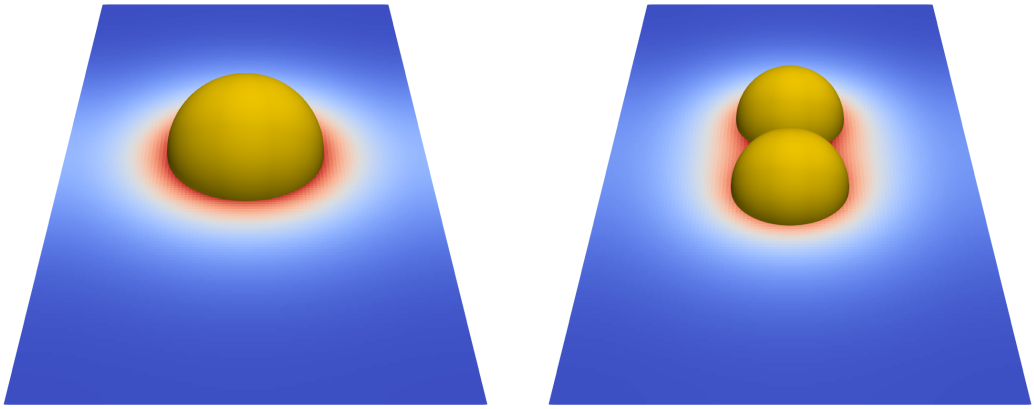

(a) (b)

Figure 4.1: Illustration of the concentration of the product species at $t/t_{max} = 0.01$ in the absence of advection for (a) a single sphere with the radius $R = 21$ and (b) two identical spheres with the radius $R = 15$. Red and blue areas represent high and low concentrations, respectively.

4.1.2 Results and discussion

We start by implementing the LBM as described in section 3.3.2 to solve the ADRE for the two systems. First we consider the case where the reactant is transported throughout the system via diffusion only. Figure 4.2(a) show that, according to our diffusion-reaction model, the large and small NPs exhibit very similar catalytic activities when the total surface area is constant. Introducing an additional hydrodynamic flow with a maximum velocity $u_{max} = 0.3$ which would correspond to stirring in an experiment, does not affect the previous finding, i.e. the reaction rate is entirely independent of the NP size (Figure 4.2(b)).

Next, we consider the impact that a sphere has on the diffusion coefficient of the reactant molecules in the immediate neighbourhood of its surface. It has been shown that, by increasing the hydrodynamic resistance, the diffusion of the molecules close to the surfaces is slowed down [95–97]. Thus, the diffusion perpendicular to the surface is slowed down more comparatively to the diffusion parallel to the surface. To investigate the influence of this effect in our systems, we extend the RWPT method from section 3.2 to account for the anisotropic surface-modified diffusion. Being a 2D model, we consider for both cases a domain with a size of 180×140 simulation units, where the spheres are replaced with one circle having the radius $R = 30$ for the large NP and two circles with radii $R = 15$ for the small NPs, respectively. This way, the

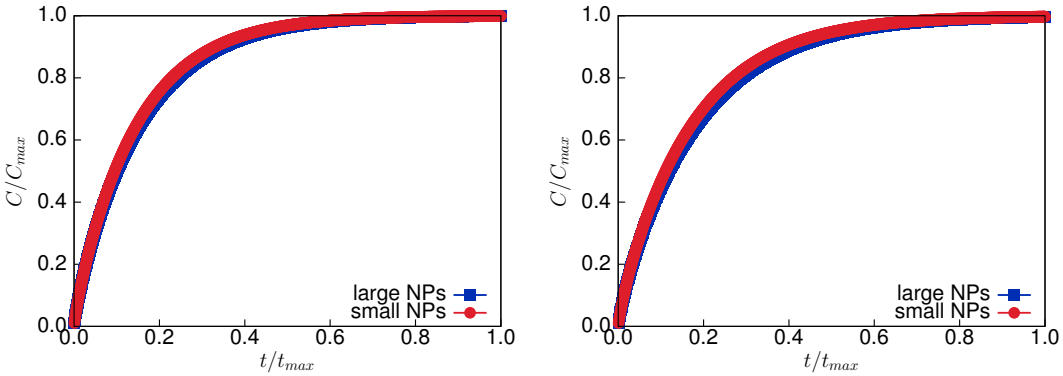

Figure 4.2: Conversion rates of the single and the two NPs using LBM (a) in the diffusion only case and (b) with a maximum advection velocity $u_{max} = 0.3$

same total circumference is ensured for both systems, which corresponds to the surface area conservation in the 3D model. A set of 100000 point particles representing the reactant species A is randomly placed in the periodic domain generating an initial homogeneous distribution. Each particle follows a random walk with a constant step size of 0.1 in a random direction, simulating normal, isotropic diffusion. When a reactant particle reaches the surface of the catalytic NP, the reaction $A \rightarrow B$ takes place with a fixed probability corresponding to the reaction rate $k = 0.1$. To introduce the anisotropic diffusion, we consider an area starting from the circle to a maximum distance of 1 simulation units away from it, where diffusion perpendicular to the NP surface is strongly hindered by choosing a step size of 0.025, while lateral diffusion is hindered comparatively more mildly by setting the displacement tangential to the surface at 0.05. The chosen values correspond, approximately, to the well-known asymmetric diffusion of single particles near a wall [98, 99].

We proceed to compare the numerical results using isotropic and anisotropic diffusion for both large and small Au NPs. Figure 4.3 shows that reaction progress is very similar in all cases, the efficiency being minimally affected for the two systems. To conclude this investigation, we can rule out even a complex surface-modified diffusion scenario as an explanation for the experimentally observed enhanced catalytic activity of large NPs. This leaves the heterogeneous formation of defects on the surface of Au NPs due to the synthetic procedure, as a more likely explanation, with recent studies suggesting that defects between crystalline domains are larger for bigger NPs, which could either enhance association and dissociation of molecules or lead to the leaching process of gold species [92].

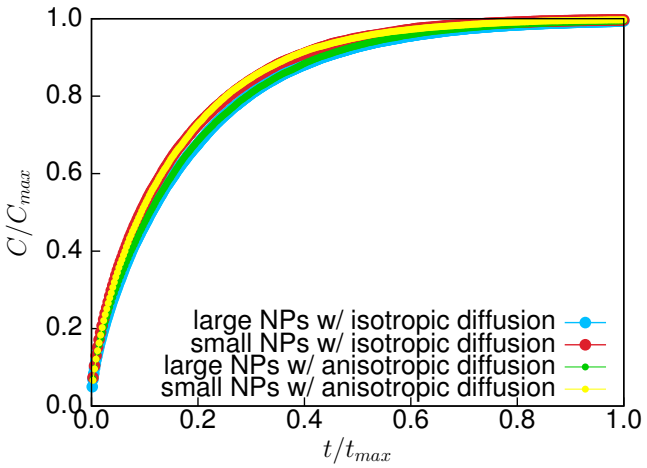

Figure 4.3: Conversion rates of the two systems using the particle model with isotropic diffusion as well as the more complex scenario accounting for the anisotropic surface-modified diffusion coefficients

4.2 Modeling the kinetics of a pseudo-first order reaction with an induction period

4.2.1 Embedded Au NP in patchy nonwovens

An important aspect regarding the catalytic performance of Au NPs is their proneness to aggregation, which leads to a decreased activity. Using low molecular weight or polymeric ligands for NP stabilisation is an often encountered strategy to prevent aggregation, but it might influence the catalytic activity of Au NPs and, as time passes, the ligands can fade away from the surface of NPs, causing destabilization and, thus, agglomeration [100, 101]. An alternative approach is the immobilization of NPs on solid inorganic support such as metal oxides and silica [28, 102], nanotubes [29] and 2D materials like graphene [30]. Other studies have employed metal-organic frameworks as versatile host materials [31, 32]. Recently, polymeric supports such as porous polymer [33, 34], microgels [103] or polymer micelles [35, 104] have attracted more attention due to their properties that can be easily tailored to the requirements of a specific catalytic application. Additionally, polymer nanofibers produced by electrospinning can be used for immobilization of NPs allowing a good recyclability of them [105, 106]. However, this feature is lost in case of hybrid nonwovens as they lack in a precise confinement of NPs, which leads to a reduction of the ratio between the surface and the volume following the process of nanofiber removal.

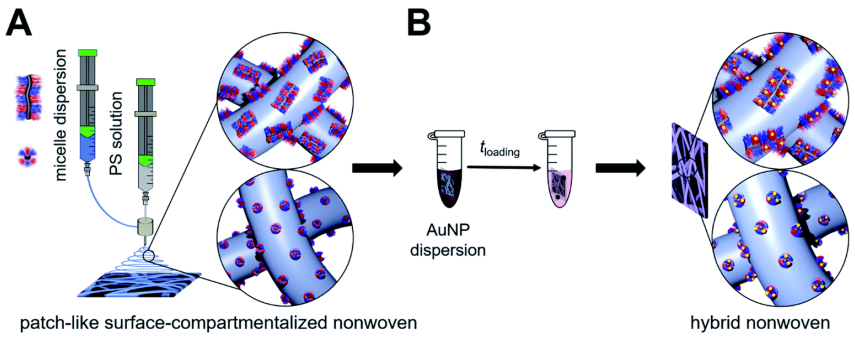

Figure 4.4: Preparation process of Au NP-loaded patchy hybrid nonwovens for the experimental study performed by Hils et al. [38]. First the functional, patchy surface-compartmentalized nonwovens are produced by electrospinning of polystyrene as the core and patchy wCCMs or sCCMs as the shell (A), then the Au NPs are loaded in a simple dipping process (B).

Schöbel et al. [36] have proposed a teabag-like catalyst system consisting of Au NP-loaded patchy nonwovens with functional, nanopatches on the surface of nonwovens. Based on this approach, Hils et al. [38] have conducted an experimental study on the influence of patch size and chemistry on the catalytic activity of patchy hybrid nonwovens in Au NP catalysed alcoholysis of dimethylphenylsilane in n-butanol. Figure 4.4 illustrates their preparation process where the patchy nonwovens were produced by electrospinning with two different geometries for shells, i.e. patchy worm-like crystalline-core micelles (wCCMs) and spherical crystalline-core micelles (sCCMs), which were then loaded with Au NPs in a simple dipping process. Furthermore, to increase the variety of physical and chemical properties of the patches, the following triblock terpolymers were used in the synthesis of the patchy micelles: $S_{28}E_{15}DiPA_{41}{}^{156}$ (s-SEDiPA), $S_{48}E_{21}DiPA_{41}{}^{181}$ (as-SEDiPA) and $S_{33}E_{17}DMA_{50}{}^{132}$ (s-SEDMA). A total of five different patchy hybrid nonwovens were prepared, with s-SEDiPA and as-SEDiPA used for both wCCMs and sCCMs, while s-SEDMA was selected only for wCCMs. Table 4.1 presents the average radius and length for sCCMs and wCCMs, respectively.

Table 4.1: Physical properties of the patchy micells

Polymer	**Radius (sCCMs) [nm]**	**Length (wCCMs) [nm]**
s-SEDiPA	31.4±0.3	260±100
as-SEDiPA	35.8±0.3	480±240
s-SEDMA	-	510±310

4.2.2 Catalytic activity of Au NP-loaded patchy hybrid nonwovens

The alcoholysis of dimethylphenylsilane in n-BuOH is then used as a benchmark [36] for the catalytic activity of the patches having various morphologies and sizes. To investigate the effect of swelling of the patches in n-butanol, 10 consecutive cycles were performed with data on the kinetics being collected for the first and last cycles. The conversion curves for the first cycles (Figure 4.5(a)) show that, irrespective of the micelle shape and patch size, the hybrid nonwovens have an initial slow stage (induction period) of 1 h with full conversion being reached between 5 h and 9 h. However, the induction times are decreased to about 10-20 minutes for the 10^{th} catalysis cycles, while the total conversion is obtained in 4-5 hours. This suggests that the first cycles are characterised by an initial period where the patches swell in the reactant, making it accessible to the reaction sites, i.e., the embedded Au NPs.

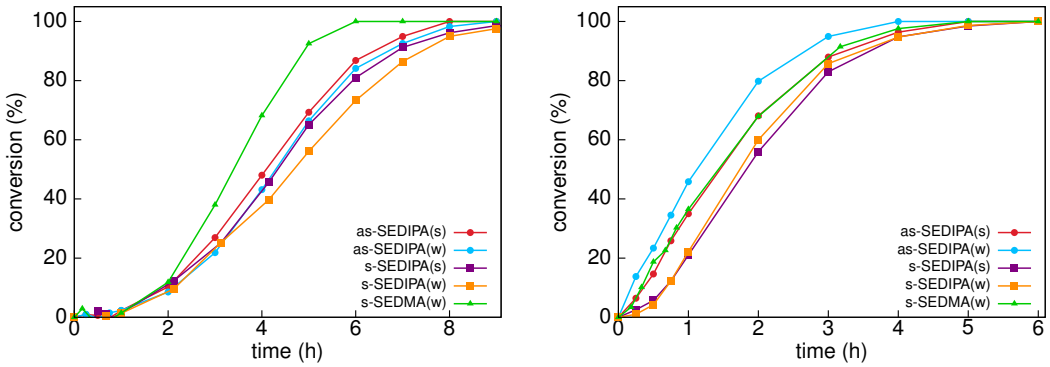

Figure 4.5: Conversion curves of the catalytic alcoholysis of dimethylphenylsilane in n-BuOH for the (a) first and (b) tenth cycles, using the five different Au NP-loaded patchy hybrid nonwovens

Considering that n-BuOH is in excess compared to silane (E), the classical pseudo-first order kinetics can be assumed. Starting from the rate law characterising the reaction

$$\frac{\mathrm{d}\,[E]}{\mathrm{d}t} = -k_{classical}\,[E]\,[n\text{−BuOH}]\,, \tag{4.1}$$

under the condition $[n\text{−BuOH}] = const$, the form corresponding to a first order reaction (section 2.3) is recovered

$$\frac{\mathrm{d}\,[E]}{\mathrm{d}t} = -k_{app,classical}\,[E]\,, \tag{4.2}$$

where the apparent rate constant is

$$k_{app,classical} = k_{classical}\,[n\text{−BuOH}]\,. \tag{4.3}$$

Integrating equation (4.2), a linear relation is recovered

$$-\ln\frac{[E]}{[E]_0} = k_{app,classical}t \tag{4.4}$$

which allows for the apparent reaction rate constant to be computed from the slope of the corresponding first order kinetics plot. To rule out the effect of initial swelling from the dry state, manifested by the long induction times observed for the first catalysis cycles, we will apply the classical pseudo-first order reaction model only to the tenth cycles. Similar to Figure 4.6, all the kinetics plots exhibit a linear behavior only in the latter stages of the reaction, despite the large excess of n-BuOH compared to silane. Thus, for a better quantitative insight into the kinetics of the reaction, a new model has to be developed.

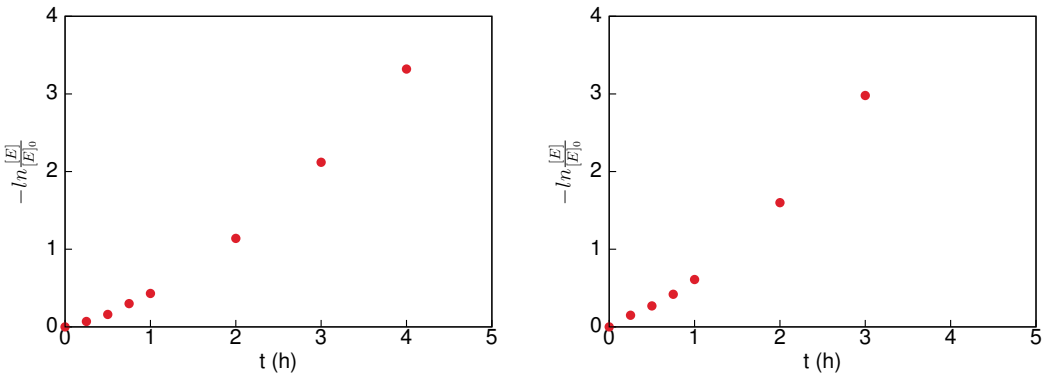

Figure 4.6: Kinetics plot for the tenth cycle of the catalytic alcoholysis of dimethylphenylsilane with an Au NP-loaded patchy nonwoven based on as-SEDiPA with (a) sCCMs and (b) wCCMs. The plots do not exhibit a linear dependence over the full time range, ruling out the classical pseudo-first order kinetics model as an accurate fit.

4.2.3 Model and results

In order to account for the influence of patch swelling, we extend the classical pseudo-first order kinetics model to include the observed induction period. Starting from the previous remarks that the slop of the kinetic plots is not constant, the rate law from equation (4.1) is adjusted

accordingly:

$$\frac{\mathrm{d}\,[E]}{\mathrm{d}t} = -k\,(t)\,[E]\,[n\text{−BuOH}]\,. \tag{4.5}$$

To address the swelling of the patches, we consider the two reactants to slowly became available to the catalytically active Au NPs with a certain accessibility rate r. Thus, the increasing availability of the reactants over the time t is modeled by the variable reaction rate $k(t)$ according to

$$k(t) = k_0\left(1 - e^{-rt}\right). \tag{4.6}$$

The accessibility rate r is a parameter controlling how quickly this process occurs. By replacing (4.6) in (4.5), the rate law can be written as

$$\frac{\mathrm{d}\,[E]}{\mathrm{d}t} = -k_{app}\left(1 - e^{-rt}\right)[E], \tag{4.7}$$

where $k_{app} = k_0[S]$ is the apparent rate constant. Separating variables and integrating equation (4.7) yields

$$-\int_{[E]_0}^{[E]} \frac{\mathrm{d}[E']}{[E']} = \int_0^r k_{app}\left(1 - e^{-rt'}\right)\mathrm{d}t'. \tag{4.8}$$

The natural logarithm form of the power law expression is then obtained as

$$-\ln\frac{[E]}{[E]_0} = k_{app}\left(\frac{e^{-rt}}{r} + t\right) - \frac{k_{app}}{r}. \tag{4.9}$$

The classical pseudo-first order kinetics equation (4.4) is recovered from the equation (4.9) of our model in the limit $r \to \infty$, which corresponds to the immediate availability of the reactants.

Similar to the approach in the classical model, we consider only the kinetics of the 10^{th} cycles. The experimental data were fitted with equation (4.9) and the two parameters from our model, i.e., the apparent rate constant (k_{app}) and the accessibility rate (r), were determined for all five types of patchy hybrid nonwovens. Figure 4.7 shows that an accurate fit over the full time range is achieved. Additionally, the rate constants are in comparable range with the values obtained by using the classical 1^{st} order kinetics model where only the linear part of the plot was fitted using equation (4.4) (table 4.2). For a quantitative comparison between the different catalyst systems, the apparent rate constants have to be normalised to the concentration of n-BuOH and the total surface area of the catalytically active Au NPs. Moreover, knowing the values for k_{app} and r it is possible to compute from equation (4.9) the corresponding induction times (t_{ind}) and reaction times (t_R) representing the time required for 3% conversion and 99% conversion, respectively.

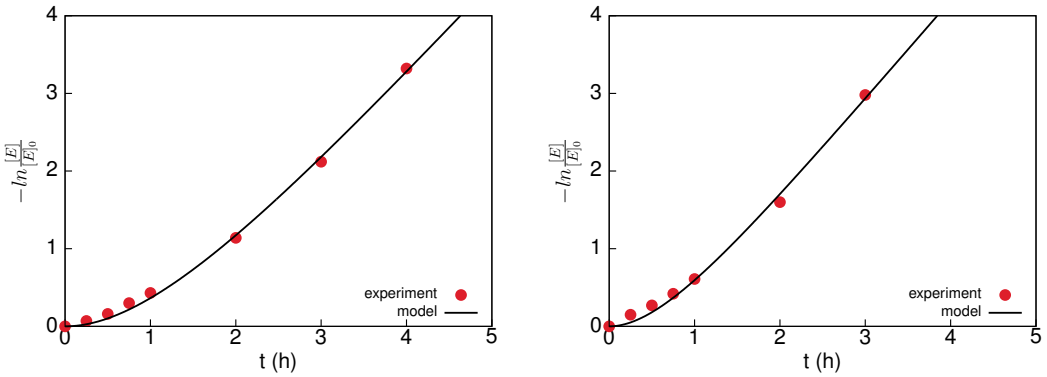

Figure 4.7: Kinetic study of the 10th cycle of the catalytic alcoholysis of dimethylphenylsilane with an Au NP-loaded patchy nonwoven based on as-SEDiPA with (a) sCCMs and (b) wCCMs. Experimental data is fitted using equation (4.9) from our extended pseudo-first order kinetics model.

Table 4.2: Comparison of the apparent rate constants and the normalised rate constants obtained using the classical and our extended pseudo-first order kinetics model

Hybrid nonwovens	$k_{app,classical}$ [h^{-1}]	k_{app} [h^{-1}]
s-SEDiPA(s)	1.21±0.02	1.77±0.10
s-SEDiPA(w)	1.11±0.06	1.54±0.11
as-SEDiPA(s)	1.09±0.06	1.18±0.10
as-SEDiPA(w)	1.18±0.11	1.27±0.11
s-SEDMA(w)	1.28±0.11	1.55±0.26

All this values are presented in table 4.3.

Analysing the hybrid nonwovens based on s-SEDiPA and as-SEDiPA, the normalised rate constants are very similar when the same composition of the polymer is used, making k independent of the CCMs chosen. However, when comparing the two polymers, the accessibility rates for as-SEDiPA are higher with respect to those of s-SEDiPA. This contributes to shorter induction and reaction times for the as-SEDiPA based nonwovens, despite having a lower reaction rate constant compared to s-SEDiPA based nonwovens. This behavior may emerge from the chemical properties resulting from the difference in length and radius of the CCMs (table 4.1) for the two polymers. Changing the patch chemistry and comparing the nonwovens using wCCMs (s-SEDiPA(w) and s-SEDMA(w)) it is possible to study the influence of patch swelling on the catalytic activity as SEDMA patches are more hydrophilic and, thus, expected to swell faster in n-BuOH. The differences can be noted starting from the 1st catalysis cycle (Figure 4.5(a)) where, although the induction times are similar ($t_{ind} \approx 1$ h), the total reaction time for s-SEDMA(w)

Table 4.3: Kinetic parameters for the 10^{th} cycles of the catalytic alcoholysis of dimethylphenylsilane in n-BuOH

Hybrid nonwovens	k_{app} [h^{-1}]	k [$\text{Lm}^{-2}\text{mol}^{-1}\text{s}^{-1}$]	r [h^{-1}]	t_{ind} [h^{-1}]	t_{R} [h]
s-SEDiPA(s)	1.77±0.10	$(1.97 \pm 0.51) \times 10^{-2}$	0.29±0.02	0.35	5.29
s-SEDiPA(w)	1.54±0.11	$(2.10 \pm 0.55) \times 10^{-2}$	0.38±0.05	0.33	5.25
as-SEDiPA(s)	1.18±0.10	$(1.19 \pm 0.31) \times 10^{-2}$	0.79±0.15	0.27	5.16
as-SEDiPA(w)	1.27±0.11	$(1.20 \pm 0.32) \times 10^{-2}$	1.43±0.38	0.18	4.32
s-SEDMA(w)	1.55±0.26	$(1.56 \pm 0.47) \times 10^{-2}$	0.54±0.16	0.28	4.68

decorated nonwoven is the lowest of all, more so compared to s-SEDiPA(w) based nonwoven (6 h vs. 9 h). For the 10^{th} cycle, s-SEDMA(w) still has lower t_{ind} and t_R and a higher accesibility rate than s-SEDiPA(w) but the gap is greatly reduced highlighting the effect of patch swelling on the reaction kinetics.

In conclusion our extended pseudo-first order kinetics model proves to be a useful tool for analysing reactions that present an induction period, being able to reproduce the experimental results over the full time range compared to the classical model where an accurate fit is possible only for the final part of the observed period that exhibits a linear behavior. In this study we have employed it to study the catalytic activity of Au NP-loaded patchy hybrid nonwovens in the alcoholysis of dimethylphenylsilane and it has revealed that the patch size and chemistry affects the accessibility of the reactants to the surface of the embedded NPs, thus influencing the reaction kinetics. The novelty of our model is the introduction of the accessibility parameter (r), which describes the rate at which the reactants (dimethylphenylsilane and n-BuOH) become available to the embedded Au NPs, thus playing an important role in the characterisation of the hybrid nonwovens. This parameter is the largest for as-SEDiPA(w) and results in the shortest observed induction and reaction times, despite the lower normalized rate constant in comparison to s-SEDMA(w) and s-SEDiPA(w) based hybrid nonwovens.

Chapter 5

Analytical and computational study of multistep reaction processes in one-pot

5. ANALYTICAL AND COMPUTATIONAL STUDY OF MULTISTEP REACTION PROCESSES IN ONE-POT

Using the state-of-the-art synthetic organic chemistry and having enough time and material resources available, it is possible to produce almost any isolated and designed organic molecule. The traditional organic synthesis, as it is usually done in laboratory, uses a step-by-step approach to convert an initial substance into a final product through a series of reactions. In this process, a recovery step is required after each reaction in order to isolate and purify each intermediate product before the next conversion step can be performed. These laborious recycle loops increase the processing costs and generate large amounts of waste, while also limiting the potential to scale up and shorten the time to market the final products.

Given the increasing attention for sustainability, the development of new techniques and strategies that can reduce waste and toxic by-products and improve resource efficiency has become essential in chemical synthesis. During the course of evolution, nature was faced with a similar issue, needing to synthesize a wide range of molecules starting from simple precursors. As a result, biosynthesis is performed through a cascade approach without any additional recovery step [107]. This way, there are fewer unit operations and the concentrations are kept low requiring less solvent and yielding less waste. An example of a common multistep syntheses is the transformation of fructose 1,6-diphosphate to lactic acid through two intermediate products, i.e. dihydroxyacetone phosphate and glyceraldehyde 3-phosphate, respectively. Cascade chemical reactions, which consists of multiple bond-forming events carried out in one pot, play an important role not only in nature but also in many technological applications [39–41].

The main hurdle in implementing catalytic cascades on a wider scale is that catalysts used may be chemically incompatible with each other (e.g. acid and base) thus preventing their mixing requires special attention. Examples for such reactions include the Knoevenagel [42, 108] or the Baylis-Hillman [43] reaction. Choen et al. have showed that Wolf-Lamb-type catalysts, which deactivate each other when they come in contact, can be used in one-pot cascade reactions by immobilizing them on solid supports [109]. Besides preventing the deactivation, good mass transport and accessibility of the active sites must be achieved. Various porous carrier systems that exhibit these properties have been studied ranging from polymeric microcapsules [110] to microporous organic nanotube networks [108].

In this chapter two-step reactions using incompatible catalysts are considered and analysed from two different perspectives. First, to gain a greater understanding of the process, we investigate the reaction kinetics of different carrier systems in section 5.1. Similar to the previous chapter, the classical equations are tailored according to the specifics of the experiment and then used to fit the results. Section 5.2 focuses on the potential of fibrous membranes as catalytic

sites for cascade reactions in flow-through reactors. For this, the efficiencies of various membrane geometries are computed using a lattice Boltzmann based solver for the advection-diffusion-reaction equation, a random walk particle tracking method and a simple theoretical model that we have developed.

Parts of section 5.1 have been published in *Chem. Eur. J.* **25**, 13640 [111] and ACS *Applied Polymer Materials* **3**, 1349 [112], while results form section 5.2 are included in *Computers & Fluids* **240**, 105438 [113].

5.1 Kinetics of one-pot cascade reactions

Chemically incompatible functional groups, such as acid and base, deactivate each other when they come in contact. When used in one-pot reactions, these Wolf-Lamb-type catalysts lose their catalytic activity, thus requiring site isolation by compartmentalization. Early studies in this field have showed that the incompatible catalysts can be immobilized on polymeric solid supports [109, 114]. Although many different approaches have been developed, one-pot multistep reactions are still not widely applicable due to the limited reusability and time consuming procedures required for producing the appropriate carriers.

One of the most promising concept is the use of polymers as carriers for mesoporous structures [115–117]. Starting from this model, we analyse two different processes for achieving the high potential of multistep one-pot cascade reactions while using systems that are modular and easy to modify. First, we consider electrospinning as a technique to obtain fibers with diameters ranging from a few hundred nanometers to a few micrometers [45]. By applying a high voltage between a needle and a collector, the polymeric solution is stretched towards the collector. In this process, the solvent evaporates and the solid fibers randomly deposit forming a porous polymer membrane. This approach allows the preparation of catalytic membranes in large amounts and sizes and, by direct spinning of polymeric acid or bases, there is no need for any precise chemistry for the immobilisation of catalytic functional groups.

The other method consists of printing a patterned polymer catalysts on a carrier material [111]. Three dimensional printing has the advantage of precise material structuring and fine tuning of the size and shape. The 2D patterned Wolf-Lamb-type catalysts on a neutral substrate by direct printing of the catalytically active polymers or the electrospun membranes can then be individually fixed in frames and introduced in a reaction medium in one-pot without coming in contact with each other. This techniques can be easily extended in a modular way with more than two incompatible catalysts for cascade reactions.

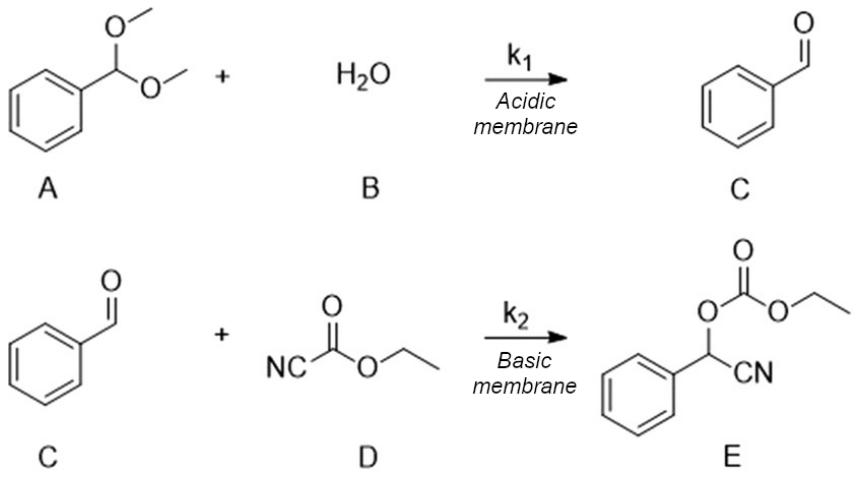

Figure 5.1: Two step reaction sequence catalysed by incompatible acid and base catalysts. The reaction components are dimethoxybenzylacetale (A), water (B), benzaldehyde (C), ethyl cyanoformate (D) and cyano(phenyl)methyl ethyl carbonate (E) while the reaction kinetic parameters for the first and second step are k_1 and k_2, respectively.

The electrospun polymeric catalyst membranes were previously analysed by Pretscher et al. [45], thus we first attempt to use the same experimental conditions for the printed membranes [111]. The reactions used for testing the catalytic activity consists of the acidic catalyzed deacetylation of dimethoxybenzylacetale (dissolved in dimethylformamide) to benzaldehyde, which reacts with ethyl cyanoformate basic catalyzed to cyano(phenyl)methyl ethyl carbonate. The steps involved in the making and breaking of the bonds during this process can be further separated in the series of reactions as presented in Figure 5.1 in order to obtain the reaction mathematical model in the form of an equation system for the five concentrations:

$$\frac{\mathrm{d}c_\mathrm{A}}{\mathrm{d}t} = -k_1 c_\mathrm{A}(t) c_\mathrm{B}(t) \tag{5.1a}$$

$$\frac{\mathrm{d}c_\mathrm{B}}{\mathrm{d}t} = -k_1 c_\mathrm{A}(t) c_\mathrm{B}(t) \tag{5.1b}$$

$$\frac{\mathrm{d}c_\mathrm{C}}{\mathrm{d}t} = k_1 c_\mathrm{A}(t) c_\mathrm{B}(t) - k_2 c_\mathrm{C}\left(t - \Delta t\right) c_\mathrm{D}(t) \tag{5.1c}$$

$$\frac{\mathrm{d}c_\mathrm{D}}{\mathrm{d}t} = -k_2 c_\mathrm{C}\left(t - \Delta t\right) c_\mathrm{D}(t) \tag{5.1d}$$

$$\frac{\mathrm{d}c_\mathrm{E}}{\mathrm{d}t} = k_2 c_\mathrm{C}\left(t - \Delta t\right) c_\mathrm{D}(t) \tag{5.1e}$$

where c_A is the concentration of (dimethoxy)methyl benzene, c_B is the concentration of water,

c_C is the concentration of benzaldehyde, c_D is the concentration of ethyl cyanoformate, c_E is the concentration of cyano(phenyl)methyl ethyl carbonate while k_1 and k_2 are the reaction rates of the first and second reaction step, respectively. The equations (5.1) resemble the classical second order kinetics model described in section 2.3, while also having the additional parameter Δt.

The fitting of the reaction rates and the concentrations based on the experimental values are performed using a nonlinear least-squares solver in Matlab version R2019b. To understand the role of Δt, we first fit the experimental data for $\Delta t \to 0$ as shown in Figure 5.2(a). The fit function works very well for the first reaction showing a good validity for c_A and c_C, but the mismatch for c_E suggests that the second reaction has a delayed starting time. Moreover, analysing the fitted parameters displayed in table 5.1, we can clearly notice that the value obtained for $c_D(0) = 3.2$ mol L^{-1} is too high compared to the initial amount of D used in the experiment, i.e., $c_D(0) = 0.6$ mol L^{-1}. The behavior of the conversion curves during the initial period of the process, shows that, even though the product C is quickly generated in the first reaction, the second step started only after a significant amount of c_C is produced. This can be explained by the fact that it requires a certain amount of time before C becomes available for the final reaction.

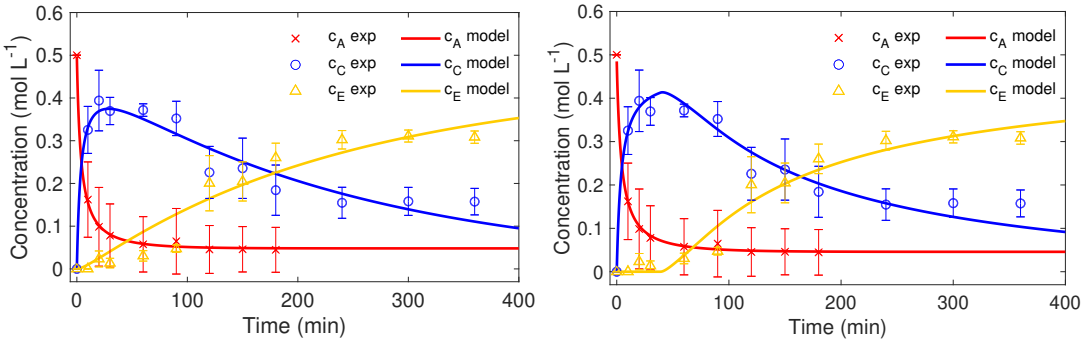

Figure 5.2: Kinetic study of the two-step cascade reaction described by Figure 5.1. (a) The classical model ($\Delta t \to 0$) shows a good fit only for the first reaction, while (b) the addition of the Δt parameter provides a better fit for all quantities.

To model this retarded start, we have introduced the parameter Δt in the equations (5.1c)-(5.1e) which account for the second step. As expected for the new fit, the parameters describing the first reaction show very small variations, while the second step is considered to start with a delay of 52 min. Although the value for the initial concentration of D has improved, this time it is only close to half of the expected result. Therefore, we fix $c_D(0) = 0.6$ mol L^{-1} to maintain the

Table 5.1: Fitted parameters after solving equations 5.1 for the cascade reaction using the 2D-printed structures

Parameter	Fitted value		
	Δt fixed	$c_D(0)$ free	$c_D(0)$ fixed
$c_A(0)$ [mol L^{-1}]	0.496	0.484	0.485
$c_B(0)$ [mol L^{-1}]	0.448	0.440	0.439
$c_D(0)$ [mol L^{-1}]	3.199	0.355	0.600
Δt [min]	0.030	52.000	39.000
k_1 [mol (L min)$^{-1}$]	0.555	0.489	0.509
k_2 [mol (L min)$^{-1}$]	0.001	0.027	0.011

experimental initial condition, which leads to a good alignment of the fitted amount of c_C and c_E (Figure 5.2(b)). The resulting fitted parameters displayed in table 5.1 are close to the values observed in the experiment, only the amount of water $c_A(0) = 0.485$ mol L^{-1} is significantly lower than the concentration of 1 mol L^{-1} used in the reaction. However, it may be explained by the adsorption of water within the printed structures which leads to a decrease of its availability.

After testing the model on a reaction that used the 2D patterned structures as Wolf-Lamb-type catalysts, we switch our focus to a direct comparison between this type of carrier and the electrospun membranes. For this, a new experiment was carried out using both systems [112]. The cascade reaction converts dimethoxy methylbenzene to benzaldehyde to ethyl-2-cyano-3-phenyl acrylate (Figure 5.3). Compared to the previous experiment, there is a change in the second step such that D is represented by ethyl cyanoacetate while the final product E is ethyl-2-cyano-3-phenyl acrylate. Moreover, for a deeper insight into the chemical properties of the carriers, the electrospun membranes were dissolved in both toluene and dimethylformamide (DMF), while for the printed structures only toluene was used. Using the observations from the first study, we proceed to fit the experimental data using the differential equations (5.1) with $c_D(0) = 0.6$ mol L^{-1} being fixed. The fitted parameters presented in table 5.2 show good agreement with the reaction conditions, i.e., $c_A(0) = 0.5$ mol L^{-1}, $c_B(0) = 1$ mol L^{-1} and $c_D(0) = 0.6$ mol L^{-1}. Similar to the behaviour observed in the first experiment, the concentration of water is lower than the expected value only for the printed structure, signaling again the adsorption of water within the system.

A first analysis of the conversion curves for electrospun membranes and 2D-printed structures in toluene (Figure 5.4(a) and (b)) reveals that the overall reaction time is lower for the printed structure. The first reaction step of the conversion to benzaldehyde is finished (more than 95%

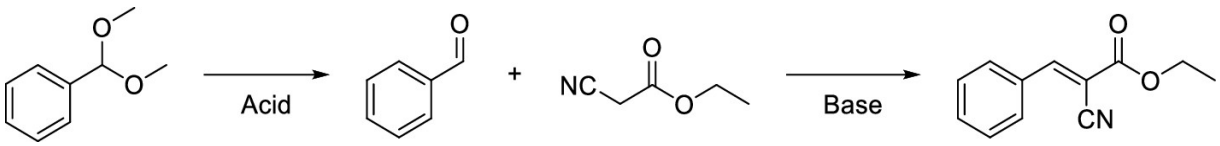

Figure 5.3: Catalytic Wolf–Lamb-type reaction of dimethoxy methylbenzene (A) to benzaldehyde (C) to ethyl-2-cyano-3-phenyl acrylate (E) in toluene and DMF

conversion), while the second step is completed after approximately 30 minutes. On the other hand, the electrospun membranes required 90 minutes for the first conversion and about 150 minutes for the full yield of the final product. This clear difference in favor of the printed structure can be explained by the swelling of fibers in electrospun membranes in the reaction medium, which leads to the formation of a gel. Thus, the reachability of catalytic sites seems to be hindered due to a more difficult mass transport within the fibrous gel network. In contrast, the printed structures are denser, requiring a shorter diffusion length to reach the sites, which leads to an increase in catalytic performance. The same observations can be made by analysing the fitted kinetic parameters from table 5.2, with the reaction rate for the first step k_1 being more than 10 times higher for the 2D-printed structures compared to the electrospun membranes. Additionally, the value of k_2 is roughly 5 times higher for the printed structures, explaining the faster conversion. A comparison between the two solvents (Figure 5.4(a) and (c)) reveals that the first step requires 180 minutes in both cases, the values for k_1 being very similar. However, the large difference in k_2 shows that toluene is a better solvent for this specific system. This translates into a total reaction time of 150 minutes and 180 minutes for toluene and DMF, respectively.

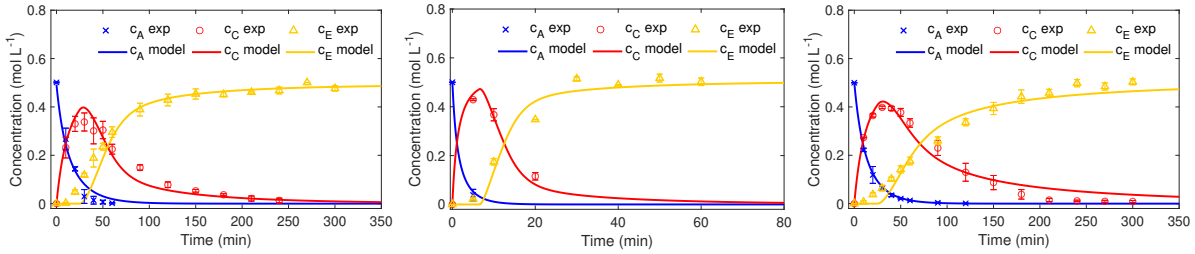

Figure 5.4: Kinetic study of the two-step cascade reaction described by Figure 5.3 using (a) electrospun catalytic membranes in toluene, (b) 2D-printed structures in toluene and (c) electrospun catalytic membranes in DMF

To summarise, we have showed that the implementation of the parameter Δt to model the

Table 5.2: Fitted parameters after solving equations (5.1) for the cascade reaction (Figure 5.3) using different solvents and structures

Parameter	**Fitted value** electrospun membrane in toluene	2D-printed structure in toluene	electrospun membrane in DMF
$c_{\mathrm{A}}(0)\,[\mathrm{mol\ L^{-1}}]$	0.492	0.504	0.502
$c_{\mathrm{B}}(0)\,[\mathrm{mol\ L^{-1}}]$	1.103	0.799	1.267
$c_{\mathrm{D}}(0)\,[\mathrm{mol\ L^{-1}}]$	0.600	0.600	0.600
$\Delta t\,[\mathrm{min}]$	25.000	6.500	25.000
$k_1\,[\mathrm{mol\ (L\ min)^{-1}}]$	0.073	0.949	0.067
$k_2\,[\mathrm{mol\ (L\ min)^{-1}}]$	0.058	0.250	0.035

delayed start in the differential equations, improves the fitting of the experimental data and offers an additional tool for studying the kinetics of the cascade reactions. Furthermore, it indicates that the slow start of the second step is not due to an intrinsic mechanism, but only that it requires a sufficient amount of the intermediate species to be produced from the first reaction.

5.2 Cascade reaction processes in catalytic fibrous membranes

Cascade reactions have attracted great attention recently due to being green processes for saving time, cost and improved atom efficiency compared to the standard multistep reactions which require consecutive product separation and isolation. The multiple catalysts and reagents, are combined in a single reaction vessel to undergo a sequence of precisely staged catalytic steps in a cascade manner. To illustrate this process, we consider an initial species A that reacts to the final product C via an intermediate species B with the two first order elementary reactions $A \rightarrow B$ and $B \rightarrow C$ each requiring a different catalyst. Such reactions were initially limited to the compatible catalysts combinations, excluding the many cases where the two are chemically incompatible (e.g. acid and base) thus preventing their mixing [118]. The site-isolated immobilisation of catalysts made possible the occurrence of acid and base (Wolf-Lamb-type) catalysed sequence of reactions in one pot. The major challenge in this processes is to achieve efficient flux of the intermediate products between different catalytic sites, while at the same time preventing physical contact of the incompatible catalysts. Form the various carrier systems previously presented in this chapter, we focus on electrospun fibrous membranes, which fulfill both requirements since they combine the ability to precisely locate different catalysts in compartments spatially separated

from each other with a high porosity required for a good mass transport. Moreover, their great potential as efficient reactor systems for cascade reactions with incompatible catalysts has also been experimentally demonstrated [44, 45, 111]. In our approach, two types of elongated fibers, one containing the first and the other the second catalyst, are combined into membranes through which the reactants are flowing.

In this section, we focus on predicting the reaction efficiency of one-step and two-step reactions where the catalytic sites have a cylindrical geometry and an additional external flow acts to transport the reactants between the various sites. These advection-diffusion-reaction systems are simulated using two different methods (LBM and RWPT) and, along with an approximative analytical model, the efficiencies are computed as function of the two relevant dimensionless parameters (the Péclet and the Damköhler number) that characterise the balance between the three phenomena.

5.2.1 System setup

We start by analysing and modeling the flow-through reactor setup. The fibers are introduced as infinitely long cylinders arranged in various geometries ranging from just one fiber performing a single reaction to two membranes consisting of randomly arranged fibers, responsible for the multi-step reactions. To ensure the mass transport between fibers, a pressure gradient has to be set from the entrance to the exit of the system in order to generate the flow field specific to a reactor.

Single reaction

First, we consider an $A \rightarrow B$ reaction driven by a single catalyst. The catalytically active site is modeled in the shape of an isolated cylinder with radius $R = 5$, that is placed in the middle of a 300×300 box as illustrated in Figure 5.5(a). Due to the translational symmetry along the fiber axis, the third dimension of the reactor becomes irrelevant. Next, we generate a regular fibrous membrane by adding multiple cylinders in the same region. For this geometry, 6 fibers with a radius $R = 3$ and random positions and orientations were placed in a $120 \times 100 \times 120$ simulation box, as displayed in Figure 5.5(b).

Cascade reaction

The scope of our study is to understand and to predict reaction efficiencies for the $A \rightarrow B \rightarrow C$ cascade reactions. Thus, we introduce the simplest case of two individual fibers being the carriers

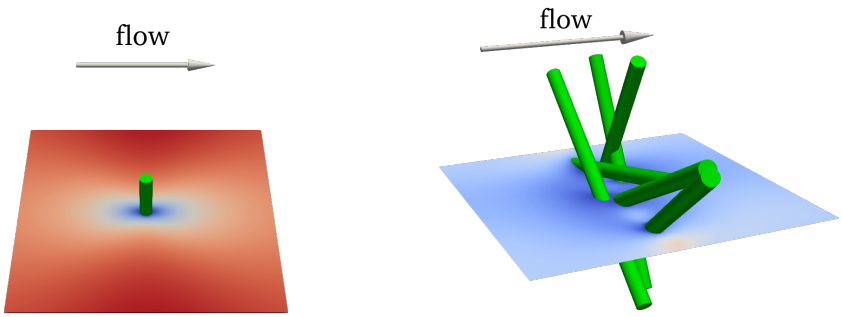

(a) (b)

Figure 5.5: Illustration of the system geometries and the flow field used in our single-reaction studies: (a) an isolated fiber, (b) a membrane with randomly oriented fibers

of the catalysts responsible for the $A \to B$ and the $B \to C$ reaction, respectively. Figure 5.6(a) shows such a system for two fibers having a radius $R = 5$ and separated by a distance $\xi = 100$ in a box of 1000×300.

The special fiber morphology called side-by-side, which can immobilize two incompatible catalysts next to each other with a common interface running all throughout the length of the fiber [119], is presented in Figure 5.6(b). In order to achieve a fair comparison between the different morphologies, the total surface area of the catalytically active sites must be constant. Therefore we set the radius $R = 10$ for the single side-by-side fiber, while the simulation box size is 1000×300.

Similar to the single reaction case, we further consider the case of fibrous membranes consisting of six randomly orientated fibers as displayed in Figure 5.6(c) and (d). However, for computational reasons, we had to reduce the dimensions of the systems such that for the single fiber morphology a radius of $R = 3$ and a box size of $200 \times 60 \times 60$ is used, while for the side-by-side fibers we have opted for $R = 6$ and a $160 \times 60 \times 60$ box.

System parameters and dimensionless numbers

The behavior of these flow-through reactors is determined by the balance between advection, diffusion and reaction. Thus, it is convenient to characterise our systems using two dimensionless numbers which encapsulate the three different phenomena. First one is the Péclet number

$$\mathrm{Pe} = \frac{u_0 R}{D}, \tag{5.2}$$

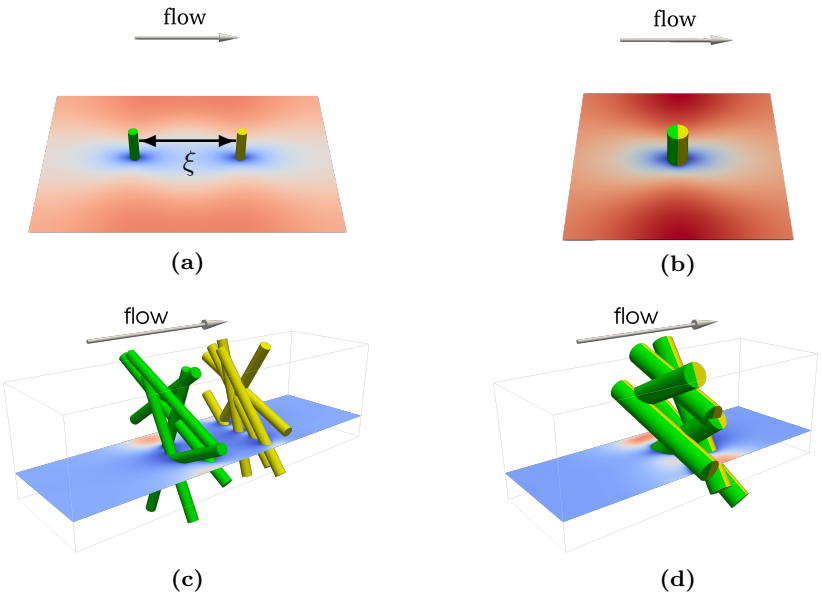

Figure 5.6: Illustration and flow field for: (a) two fibers, (b) a single side-by-side fiber, (c) two membranes, each carrying a different catalyst, (d) a single side-by-side membrane

giving the ratio between the advection velocity u_0, the fiber radius R and the diffusion coefficient D. For u_0 we choose the centerline, i.e., maximum velocity at the entrance. The second is the Damköhler number

$$\mathrm{Da} = \frac{kR^2}{D}, \tag{5.3}$$

giving the ratio between the reactive and the diffusive time scales, with k being the reaction rate constant. To compare the different parameters and geometries, we use as an output parameter for our studies the reaction efficiency defined as

$$\epsilon = \frac{N_B}{N_A + N_B} \qquad \text{for } A \to B \tag{5.4}$$

$$\epsilon = \frac{N_C}{N_A + N_B + N_C} \qquad \text{for } A \to B \to C \tag{5.5}$$

where N_x is the number of particles of species x that flow out of the system per time unit. Additionally, another quantity that may be of interest when analysing a flow-through reactor is the production rate. Thus, we also compute the amount of final product that leaves the reactor per unit of time in order to have a qualitative description of the systems for a direct comparison with the efficiency trends. As both the system parameters as well as the main output quantity

are dimensionless and thus independent of the employed unit system, we use simulation units throughout this study for simplicity.

5.2.2 Simulation methods

Lattice Boltzmann

The evolution of the concentration field of each species throughout a system is determined by the ADRE (2.17). Since the species concentration does not affect the fluid dynamics, the flow field $\vec{u}$ is constant in time, but not in space due to the fibers. Thus, we first compute the steady-state velocity field using a NSE solver for each system described before. Then, the resulting $\vec{u}$ is used as an input for an ADRE solver. Due to its amenability to parallelisation combined with the ability to handle the complex geometries displayed by the fibrous membranes arrangements, we opt to use the lattice Boltzmann method (section 3.3) for both equations.

For the NSE, we use the LBM implementation from the free software package ESPResSo [82, 120, 121]. Here we set the time step $\Delta t = 1$, the lattice spacing $\Delta x = 1$ and a body force $f = 10^{-6}$ in x direction to generate the pressure difference. For simplicity, each system geometry is simulated only once for about 6000 time steps until the steady flow is reached at this low pressure gradient. To obtain other velocities, we use the linearity of Stoke flow and we just multiply the previously generated field with a constant scaling factor. There is no loss of accuracy due to this procedure at $\mathrm{Re} \ll 1$, a condition which is satisfied in most of our setups. Even at the highest velocities that occur in our study, the maximum corresponding Reynolds number is $Re \approx 7$, for which the inertial corrections are expected to be small and linearity is still a reasonable approximation.

The boundaries of the system are periodic in all directions, while at surfaces of the fibers a bounce-back boundary condition ensures the no-slip condition.

To solve the ADRE, we have implemented a LBM as described in section 3.3.2. We simulate our systems by employing the same lattice as the one utilised in the NS LBM above. Using a time step of $\Delta t = 1$, a steady concentration profile is typically obtained after a number of time steps ranging from 130000 in the low Pe regime to 8000 for higher Pe. To replicate the flow-through reactor, we set a homogeneous concentration of the initial substance $C_A = 1$ as a boundary condition at the entrance while for the rest of the species a simple bounce-back is performed. At the channel outlet, the normal derivatives are set to zero for every species.

The output parameters are computed by measuring the outflux of the species through a plane perpendicular to the flow direction and located two lattice points away from the right

system boundary. At this position, the difference between all the populations streaming towards the outlet (right) and those streaming to the left is computed for each node and subsequently averaged across all nodes. The concentrations are then directly proportional to the particle numbers N in equation (5.5). The remainder of the boundaries are considered periodic.

Membrane generation

Membranes were generated by placing randomly oriented cylindrical fibers inside the simulation box. Cases where two or more fibers showed significant overlap were discarded. The cylinders are then included as boundaries as described in Section 5.2.1 into the ESPResSo software. Due to the random orientation, the periodicity of the fibers cannot be ensured, and thus the cylinders are closed at both ends to avoid the fluid running inside. The boundaries used for generating the flow fields are then inserted in the ADRE solver to simulate the concentration fields throughout the exact same systems.

Random walk

In addition to the LBM, we have also used a random walk particle tracking method (section 3.2). However, for simplicity and computation efficiency, we limit our implementation of RWPT to 2D systems. Thus, we only simulate the geometries with translational invariance along the fiber axes, i.e. systems illustrated in Fig. 5.5(a) as well as 5.6(a) and (b). Since the space in RWPT method is continuous, the discrete flow field generated with ESPResSo is interpolated to obtain the advective contribution for each particle at every time step. The fibers are not imported as the discretised lattice version from LBM, instead are modeled as circles with the center position and radius identical to the ESPResSo setup.

To introduce the reactions, we consider a thin reactive zone of size $\delta = 0.2$ around each fiber carrying a catalyst. Every particle of a species that performs a reaction in the presence of that catalyst, has the probability $k\Delta t$ to react within a time step inside that region. The collision between a particle and a fiber is considered elastic, such that the normal component of the particle velocity is inverted while the tangential component is not affected.

We implement the constant homogeneous concentration $C_A = 1$ along the inlet surface of the system by periodically adding or removing particles at random locations when necessary. For the rest of the species a bounce-back is set at the entrance. At the outlet, all particles that exceed the dimension of the system are removed. The other boundaries are considered periodic. The efficiency is computed using the definition given in equation (5.5) by counting the number of

particles that leave the reactor for each species during one time step.

5.2.3 Results and theoretical model

Single reaction

We start our investigation by considering a single catalytic fiber placed in the middle of a domain as displayed in Figure 5.5(a). The initial reactant A is advected by a fluid from left to right and, after suffering a reaction on the surface of the fiber, is converted into the product species B. Using the definition from equation (5.5), the efficiency is computed as a function of the Péclet number, both from the LBM and RWPT simulations. Figure 5.7 shows the decrease of the efficiency ϵ with Pe, which can be explained by the fact that at higher velocities (higher Pe), the particles spend less time near the catalyst and thus, a smaller fraction of them can reach the catalytic site and react. Changing the reaction rate k reveals that this behavior is qualitatively independent of the dimensionless Damköhler number Da which can be seen by comparing Figure 5.7(a) and (b).

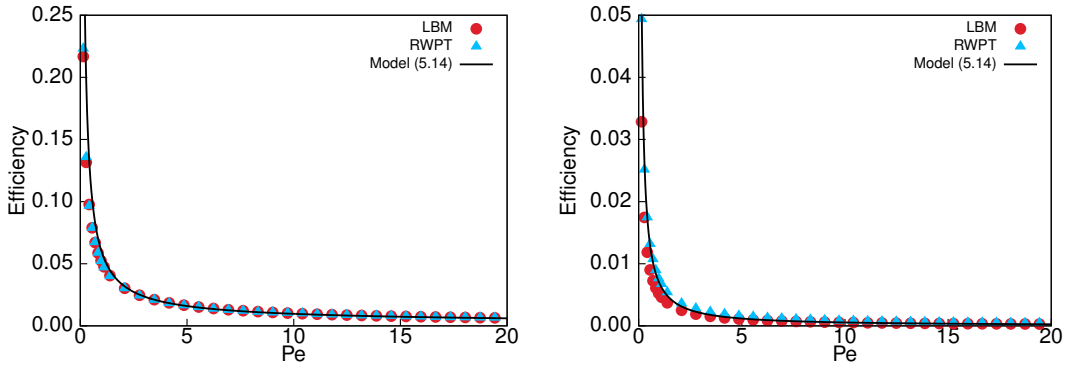

(a) (b)

Figure 5.7: Efficiency of an $A \rightarrow B$ reaction as a function of Pe for a system containing a single fiber as illustrated in Figure 5.5(a). The corresponding Damköhler numbers are set to (a) Da = 150 via $k = 1$ and (b) Da = 1.5 via $k = 0.01$.

For a deeper insight into the behavior shown by the simulation results, we propose an approximative analytical model. We consider a single fiber represented by an infinitely long cylinder with radius R in a domain with the width l from the center, as illustrated in Figure 5.8. The species are advected from left to right by a steady flow. Next, we consider a maximum distance d from the surface of the cylinder at which a particle is able to reach the fiber through diffusion. In contrast, all particles outside this region around the cylinder are assumed to be

advected without ever interacting with the catalytic fiber.

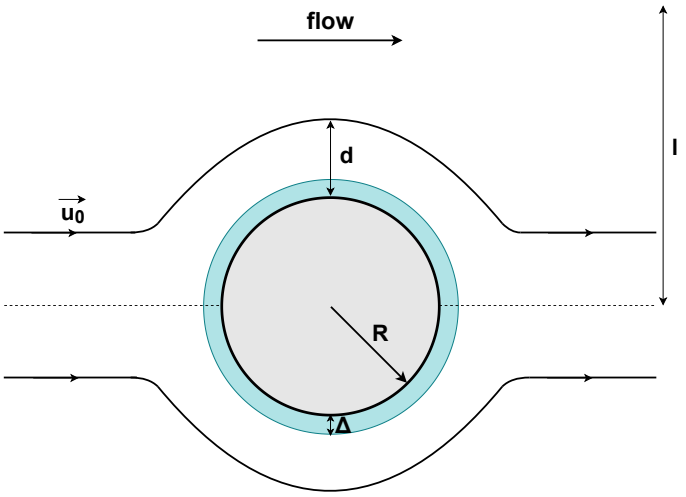

Figure 5.8: Illustration of the approximative theoretical model. The streamline separates the particles of reactant that never reach the cylinder from those that suffer at least one collision with it. The reaction can take place only in the highlighted region at a maximum distance Δ from the surface of the fiber

Assuming a homogeneous distribution of species at the inlet and a much larger domain size compared to the cylinder, the fraction of particles that suffer at least a collision can be expressed as the ratio between the widths of the two regions

$$\epsilon_{\text{coll}} = \frac{d}{l}. \tag{5.6}$$

For a particle moving with the velocity $\vec{u}_0$ along the streamline placed at the distance d from the fiber, the time t_a required to advect past the cylinder is equal to the time t_D required to diffuse towards the cylinder:

$$t_{\text{a}} = \frac{\pi\,(R+d)}{u_0} \tag{5.7}$$

$$t_{\text{D}} = \frac{d^2}{2D}, \tag{5.8}$$

where the one dimensional diffusion was considered due to the radial symmetry of the system. Equating (5.7) and (5.8) yields the following quadratic equation for d

$$\frac{1}{2D}d^2 - \frac{\pi}{u_0}d - \frac{\pi R}{u_0} = 0. \tag{5.9}$$

Considering that only half of the particles diffuse towards the cylinder, replacing the solution of (5.9) in (5.6) and introducing the Péclet number gives using the positive root of (5.9)

$$\epsilon_{\text{coll}} = \frac{1}{2}\left(\frac{\pi}{\text{Pe}} + \sqrt{\frac{\pi^2}{\text{Pe}^2} + \frac{\pi}{2\text{Pe}}}\right)\frac{R}{l}. \tag{5.10}$$

The reaction of the particles that reach the surface of the fiber is characterised by the reaction rate constant k and thus the efficiency (5.5) can be rewritten as

$$\epsilon = \epsilon_{\text{coll}}\left(1 - e^{-kt_{\text{r}}}\right) \tag{5.11}$$

where the reaction time scale t_r represents the time that the particle spends in the proximity of the catalytic surface. To determine t_r we consider a thin reaction shell of width Δ as displayed in Figure 5.8, within which the reaction can take place. The ratio between the reactive and the diffusive timescale can be expressed as the ratio α between the areas within which the reaction takes place and the area where collisions take place

$$\alpha = \frac{t_{\text{r}}}{t_{\text{D}}} = \frac{(R+\Delta)^2 - R^2}{(R+d)^2 - R^2}. \tag{5.12}$$

Assuming that the widths of the two regions are much smaller than the radius of the fiber, the ratio can be estimated in a simpler form as

$$\alpha \overset{(R\gg d,\Delta)}{\approx} \frac{\Delta}{d}. \tag{5.13}$$

This yields the new expression for the efficiency

$$\epsilon = \epsilon_{\text{coll}}\left(1 - e^{-k\alpha t_{\text{D}}}\right). \tag{5.14}$$

The width of the reaction region represents a fitting parameter for our model and a value of $\Delta = 0.5$ is selected for all simulations. Our choice is directly linked to the LBM algorithm where the space is discretised in a rectangular grid with unit spacing, and thus the average distance between the reactive surface and a neighboring lattice point will be of the order of half a grid cell.

For the single fiber case, the efficiencies predicted by this model are in very good agreement with the simulation results as shown in Figure 5.7. Deviations occur only in the low Pe regime where the width d of the collision zone increases and becomes comparable with the system width

l. As result, the idealized clear-cut separation between the collision and the no-collision zone on which our model is based becomes increasingly blurred, leading to less accurate predictions.

To estimate the total production from this theoretical model, the efficiency is multiplied by the flux of particles at the inlet. The difference between 2D and 3D systems becomes relevant when measuring the total number of B particles that leave the domain per unit of time, so we account for this by considering the number of node layers in the third dimension present in the LBM. The corresponding results, displayed in Figure 5.9, show a reasonable qualitative agreement between the three sets of data with the expected overestimated value from the theoretical model in the low Pe regime. Despite the drop in efficiency noticed in Figure 5.7, there is an increase of the total production at higher flow speeds due to the higher mass flux. This effect is especially obvious at large reaction rate constants, where the most of the particles react in a very short amount of time when close to the fiber.

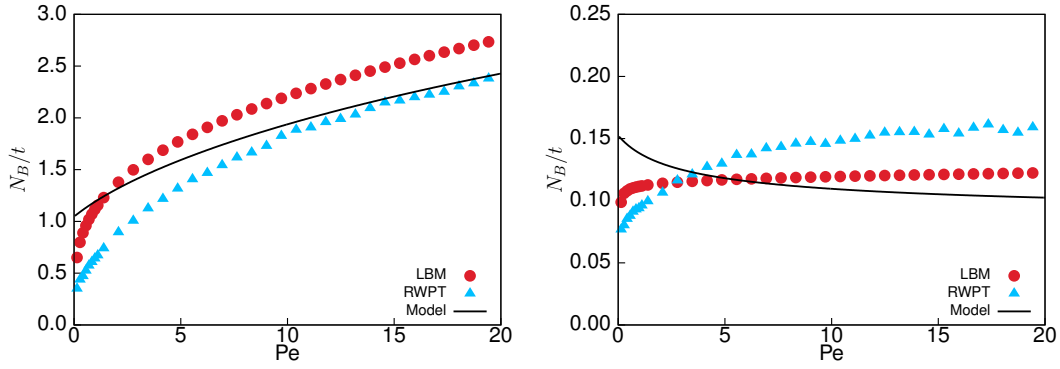

(a) (b)

Figure 5.9: Production rate of B species as a function of Pe for (a) Da $= 150$ ($k = 1$) and (b) Da $= 1.5$ ($k = 0.01$).

To further investigate the role of the reaction rate, we now focus on its influence on the efficiency. The numerical results presented in Figure 5.10 show the predicted trend that ϵ increases with Da. The growth rate slows down with increasing Da and eventually a plateau is reached where the reaction rate is so high that every molecule that collides with the surface immediately reacts and thus no further increase in efficiency is possible. This behavior is qualitatively and, within some limits, also quantitatively reproduced by the theoretical model. We note again that the only adjustable parameter of our model is set to $\Delta = 0.5$ throughout the entire study and not re-fitted for each simulation series individually.

The corresponding total production plots are shown in Figure 5.11 where, similarly to the

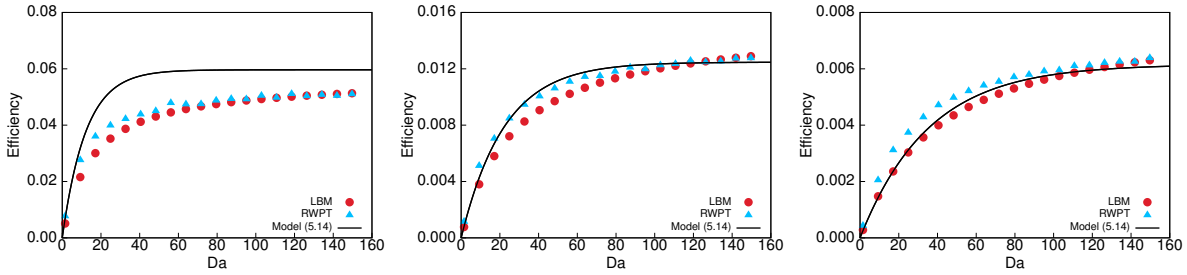

(a) (b) (c)

Figure 5.10: Efficiency of an $A \rightarrow B$ reaction, in the presence of a single fiber, as a function of Da for (a) Pe = 1, (b) Pe = 7, (c) Pe = 20.

previous cases, the best agreement is reached at high Péclet numbers.

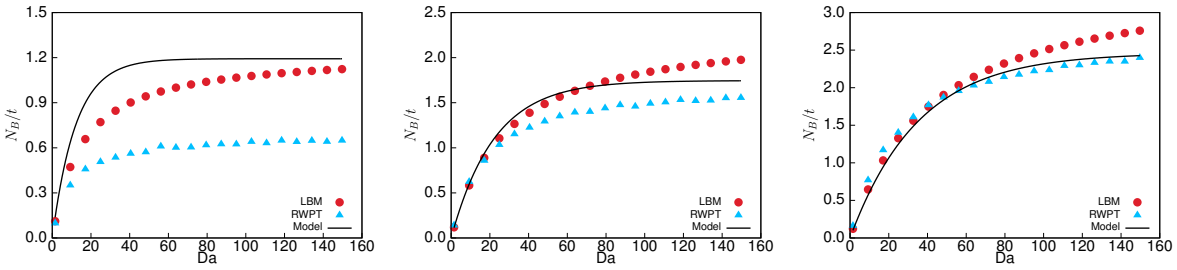

(a) (b) (c)

Figure 5.11: Production rate of an $A \rightarrow B$ reaction, in the presence of a single fiber, as a function of Da for (a) Pe = 1, (b) Pe = 7, (c) Pe = 20.

Having understood the system behavior for a single isolated fiber, we proceed to investigate the effect of multiple fibers. If the fibers are close to each other, this is a non-trivial extension as the catalytically active sites can compete with each other for the same pool of reactants. As a result, the overall efficiency of the system becomes less than the sum of each individual fiber's efficiency. To reduce potential biases in the arrangement of the cylinders, we consider two different membranes, each consisting of six randomly aligned fibers as illustrated in Figure 5.5(b). Being a truly 3D system, the RWPT method cannot be applied to the membranes, so only the LBM is used for numerical simulations. The results shown in Figure 5.12 reveal the same general trend of efficiency decreasing as Pe increase, that is also observed for the single fiber. However, the decline of efficiency appears to be less drastic than in the isolated fiber scenario. The production rates associated to the membranes are plotted in Figure 5.13.

Our theoretical model can also be extended to account for the multiple fibers that form

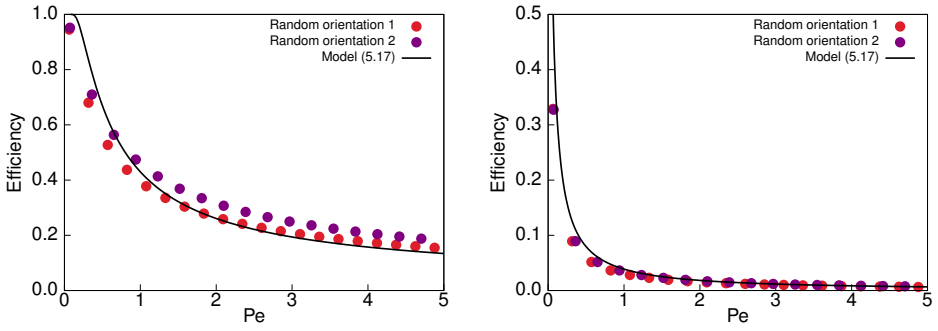

Figure 5.12: Efficiency of an $A \rightarrow B$ reaction performed by a membrane consisting of six randomly oriented fibers as illustrated in Figure 5.5(b). The reaction rates correspond to (a) Da = 150 and (b) Da = 1.5.

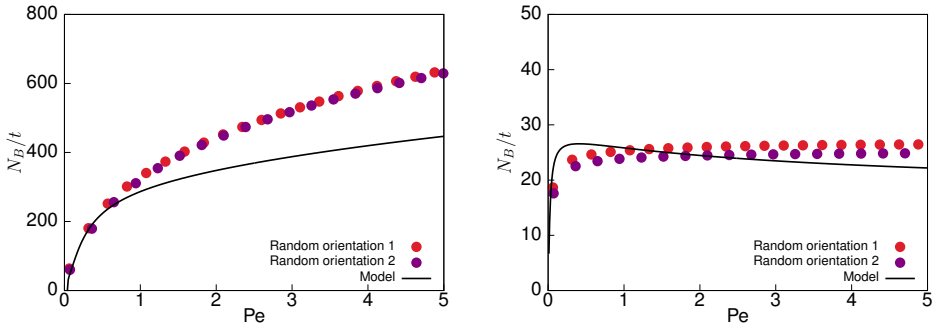

Figure 5.13: Production rates of an $A \rightarrow B$ reaction performed by a membrane consisting of six randomly oriented fibers as illustrated in Figure 5.5(b). The reaction rates correspond to (a) Da = 150 and (b) Da = 1.5.

the membranes. For this, we consider n identical fibers each having a random orientation. Being close to each other, one can assume that the reactive regions of size d corresponding to different cylinders overlap, and thus all fibers share the same pool of potential reacting molecules . Accordingly, the efficiency of the i^{th} fiber from the membrane can be expressed as the efficiency of a single fiber applied to the unreacted particles left over from the previous $(i-1)$ fibers. Adding up all the n fibers, the overall efficiency of the membrane is given by

$$\epsilon_{\text{mem}} = \sum_{i=1}^{n} \epsilon \left(1-\epsilon\right)^{i-1} . \tag{5.15}$$

Performing the summation yields

$$\epsilon_{\text{mem}} = \epsilon \frac{(1-\epsilon)^n - 1}{(1-\epsilon) - 1}, \tag{5.16}$$

which leads to the final form for the efficiency of a n-fiber membrane

$$\epsilon_{\text{mem}} = 1 - (1-\epsilon)^n . \tag{5.17}$$

As it can already be seen in Figure 5.12, this model extension is in similarly good agreement with the simulation data as was already the case with the single fiber.

5.2.4 Cascade reaction

In order to study the $A \to B \to C$ cascade reaction, a second fiber or membrane, responsible for the conversion of B into C, is introduced into our simulation and theoretical model. This adds a new parameter compared to the single reaction, which is the distance ξ between the two catalytically active sites. In the limit $\xi \to 0$, the side-by-side morphology is recovered as illustrated in Figure 5.6. We will proceed to investigate the cascade reactions by considering both the pure diffusion case and advection-diffusion case.

Pure diffusion case

To assess more clearly the influence of the catalyst distance, we start by investigating a slightly modified simulation setup where the external flow is absent and so the transport is driven by diffusion only. Additionally, at the start of the simulation, particles representing A species are homogeneously distributed throughout the whole system and periodic boundaries are imposed in all directions. Since there is no inflow and outflow of substance, instead of the efficiency ϵ, we now monitor the total concentration of the three species over time. To study the single fibers, a 300×300 box was used and two fibers with a radius $R = 5$ were placed far away from each other for the individual approach, while for the side-by-side morphology a single fiber with a radius $R = 10$ was considered such that the total surface area is conserved. For the randomly generated membranes, the box size was set to $200 \times 60 \times 60$ and six fibers were used to form a membrane having $R = 3$ and $R = 6$ for the individual and side-by-side, respectively. Figure 5.14(a) shows the corresponding data for two fibers separated by a distance $\xi = 100$ compared to the side-by-side morphology. Even though the total surface areas for both systems were kept constant, the side-by-side morphology proved to be faster due to the placement of the

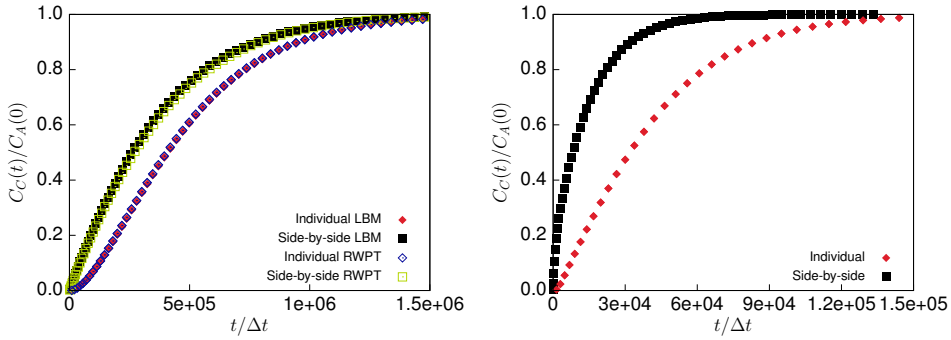

Figure 5.14: Conversion curves for the $A \rightarrow B \rightarrow C$ cascade reaction in the absence of external flow for Da = 150. (a) The comparison between two fibers separated by $\xi = 100$ and the side-by-side morphology shows a slight superiority of the latter. (b) The effect becomes more obvious for the membrane geometries.

catalysts next to each other such that the intermediate species required less time to reach the next catalytic site. The same effect is present in an accelerated form in the case of membranes (Figure 5.14(b)). As expected, similar behaviours, albeit to a lesser extent, are observed at lower Da as shown in Figure 5.15.

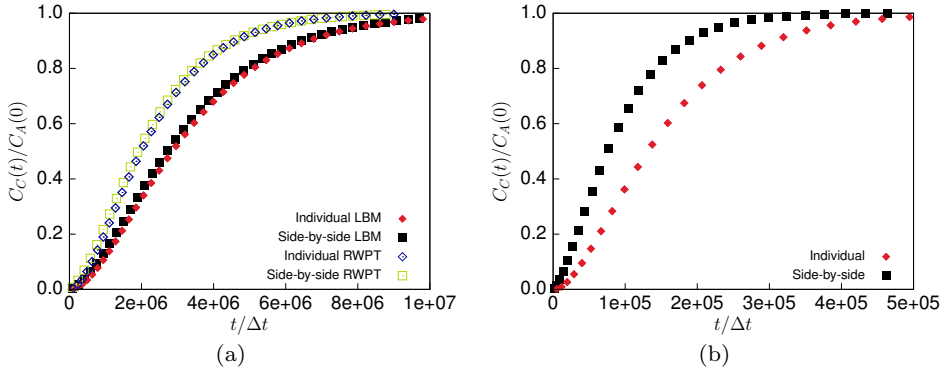

Figure 5.15: Conversion curves for the $A \rightarrow B \rightarrow C$ cascade reaction in the absence of external flow for Da = 1.5. (a) The comparison between two fibers separated by $\xi = 100$ and the side-by-side morphology shows almost no difference. (b) The superiority of the side-by-side morphology becomes clearer for the membrane geometries.

Advection-Diffusion case

While the effect introduced by the parameter ξ in the basic setup of the pure diffusion scenario was relatively obvious, its robustness even in flow is not so clear. Thus, we now return to study

the flow-through reactor systems by first considering the system illustrated in Figure 5.6(a). The efficiency ϵ is computed as a function of Pe for different distances ξ, using LBM and RWPT simulations. The results, presented in Figure 5.16, exhibit the same trend as in the previous section, namely that a closer spacing leads to more efficient reactions, with the highest efficiency achieved for the side-by-side morphology. Here we must note that the relatively large difference between the $\xi = 2$ and the side-by-side scenario can be mostly attributed to the definition of Pe which involves the differing radii $R = 5$ and $R = 10$, respectively.

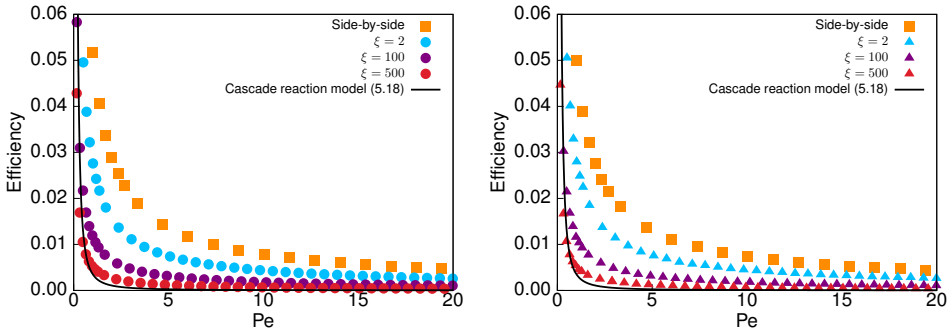

(a) (b)

Figure 5.16: Efficiencies of $A \to B \to C$ cascade reactions simulated using (a) LBM and (b) RWPT method for Da = 150. The two fibers that perform the reactions are separated by a distances ξ, as illustrated in Figure 5.6(a). The large difference between the side-by-side morphology and $\xi = 2$ is mostly due to the definition of Pe which involves the different radii $R = 10$ and $R = 5$, respectively.

For a more accurate comparison, the efficiency is represented as a function of the absolute flow velocity in Figure 5.17. Although the difference shrinks in this case, the trend still shows that having the two catalytic sites closer to each other is more beneficial, and thus the side-by-side morphology remains the most efficient geometry.

We now look to extend our theoretical model to include the second catalyst. For simplicity, we start by placing the second reaction site downstream at a distance $\xi > 2d$ from the first one such that the two collision regions do not overlap. Since the two fibers are considered far away, the B particles produced at the first catalytic site have enough time and space to diffuse throughout the system such that we can assume a fairly homogeneous distribution approaching the second site. As a result, the expected efficiency is then given by the product of the efficiency for each individual fiber

$$\epsilon_{\mathrm{ABC}} = \epsilon^2. \tag{5.18}$$

By analysing Figure 5.16, it can be seen that this approach indeed reproduces well the simulation

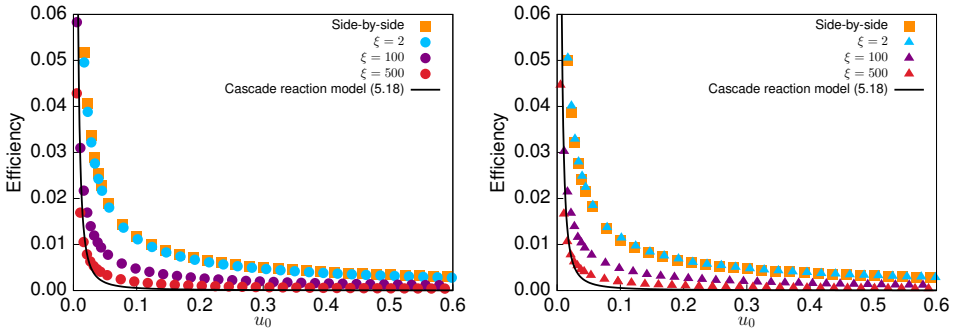

(a) (b)

Figure 5.17: Efficiencies of $A \to B \to C$ cascade reactions plotted as a function of the absolute flow velocity. The system illustrated in Figure 5.6(a) was simulated using (a) LBM and (b) RWPT method for Da = 150.

data at large ξ.

In order to simulate the cascade reaction for a multi-fiber system, two membranes separated by $\xi = 50$, each carrying a different catalyst were assembled using six randomly orientated fibers with a radius $R = 3$, as shown in Figure 5.6(c). Similar to the previous approach, the side-by-side membrane consisting of six fibers but with a radius $R = 6$ and illustrated in Figure 5.6(d), was also studied for comparison. To discard possible biases introduced by the random generation of the membranes, three different configurations were considered. In complete analogy to equation (5.18), our model predicts the total efficiency in the form

$$\epsilon_{\text{mem,ABC}} = \epsilon_{\text{mem}}^2 \tag{5.19}$$

which is in good agreement with the simulation data as shown in Figure 5.18. The match between the model and all three random membranes illustrates that the precise arrangement of fibers within a membrane is only of secondary importance for its catalytic efficiency.

Since the catalytic sites are next to each other in the side-by-side configuration, we can assume that shortly after the B particles are produced, almost all of them reach the second site. Therefore, the efficiency (5.17) of a geometrically identical membrane performing a simple $A \to B$ reaction can be viewed as the limiting case for the side-by-side membrane. This behaviour can be clearly observed in Figure 5.19 which displays the efficiencies and production rates as a function of the absolute flow velocity for a more accurate evaluation of the gap between the two morphologies.

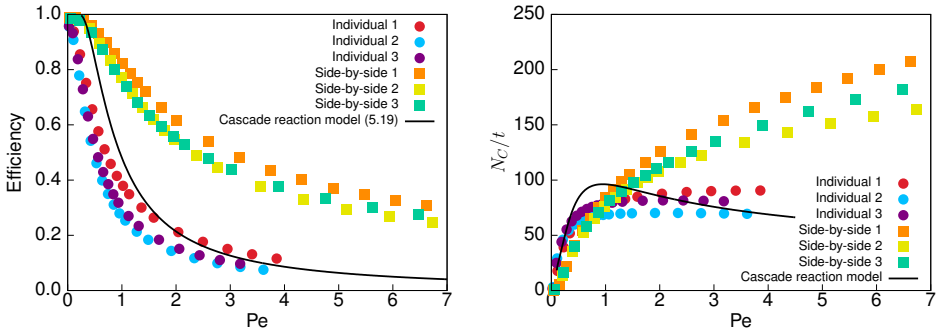

(a) (b)

Figure 5.18: (a) Efficiencies and (b) Production rates of randomly generated membranes for the $A \rightarrow B \rightarrow C$ reaction at Da = 150. All three sets of membranes for each morphology show good agreement with the proposed model, despite the various arrangements.

5.2.5 Summary

The efficiency of fibrous membranes as catalyst carriers in flow-through reactors was studied using a lattice Boltzmann solver for the advection-diffusion reaction equation. Complementary, an approximative theoretical model was developed as a tool for predicting the behaviour of such systems. First, the two methods were applied on the simple $A \rightarrow B$ first order reactions, followed by the introduction of a second catalytic site further down the stream in order to evaluate the efficiency of the multi-step $A \rightarrow B \rightarrow C$ reactions. The catalytic performance of the flow-through reactors were predicted as a function of two dimensionless numbers, i.e. the Péclet number which capture the ratio between advective and diffusive transport and the Damköhler number which relates reaction to diffusion. Moreover, the influence of the geometry of the system was analysed in the context of two different fiber morphologies. Our analytical model, characterised by a single adjustable parameter Δ, proved to be in full agreement with the numerical results.

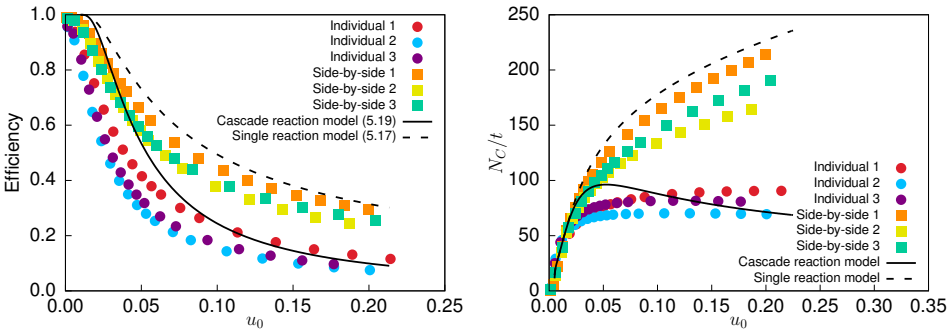

(a) (b)

Figure 5.19: (a) Efficiencies and (b) Production rates of randomly generated membranes for the $A \to B \to C$ reaction as a function of the absolute flow velocity, for Da = 150. While the data for the individual fiber membranes show good agreement with equation (5.19), the behavior of the side-by-side configuration can be fairly well approximated by equation (5.17) which describes a simple $A \to B$ reaction.

Chapter 6

Species mixing in a microchannel

Microfluidic devices have attracted considerable interest over the last two decades having applications in a wide range of processes such as chemical synthesis [54, 122], biological processing [123, 124], clinical diagnostics [125] or bioprinting [58]. Reduced sample consumption, precise control of output, low cost and portability are some of the advantages associated with microfluidic devices. A fundamental role in this systems is played by mixing which determine the performance of these processes. Given their small dimensions, microfluidic devices are characterised by low Reynolds number corresponding to laminar flow. Therefore, in the absence of turbulence, mixing is driven only by diffusion which is a slow process and requires longer microchannels to reach a homogeneous state. As result, additional mechanisms are sought to enhance mixing efficiency within shorter distances, which can reduce the size of the devices and increase its throughput.

Due to the continuing growing interest in microfluidic applications, the theory behind flows and mixing at microscale and the progress on the development of micromixers have been summarised in several state-of-art reviews [59, 126–128]. Based on how the fluids are manipulated, mixers are classified as active type and passive type. Active micromixers require external energy source to employ active elements such as pressure [129], acoustic [130] and electric field perturbations [131] and offer the highest degree of mixing. By contrast, passive mixers rely only on pressure gradient to drive the flow and uses elements such as channel geometry and special microstructures to split, break or fold the streams in order to achieve homogeneous mixing [60]. Although passive mixers may not always be simple to manufacture, they are easier to integrate and more robust compared with active mixers, which makes them more widely used.

From the various passive mixers that have been proposed over the years [61], we focus on the most popular types, i.e. obstacle based and lamination based micromixers. In the first case, it has been shown that various channel shapes containing embedded grooves or barriers can achieve high mixing efficiencies [132, 133]. However, at low Reynolds number, the serpentine channel does not significantly improve mixing by itself [134] and additional obstacles are required [135]. Lamination based mixers split the streams in order to form multilayered flows which leads to excellent mixing in short amount of time [62].

In this chapter, we investigate micromixing in the presence of a deformable capsule that is flowing through the channel. To our knowledge there is a lack of studies on topic, which can have direct implications in fields such as drug delivery [136] or bioprinting [58]. Therefore, the influence of the capsule on the mixing process is analysed in combination with some simple passive mixers. Obstacle based designs have been discarded due to the high local strains which

can damage the microcapsule through shearing and only used for comparison. For the channel geometry, a sinusoidal shape was chosen due to its increased efficiency compared with the straight or the simple serpentine channel [63]. Additionally, coaxial, side-by-side and parallel lamination concentration distribution were imposed at the inlet and their mixing performances were compared.

6.1 Mixing in microfluidic devices

6.1.1 Mixing principles

Generally speaking, the laws that describe the flow at macroscale are also valid for flows in microsystems. However, microfluidic devices cannot be viewed just as a scaled-down version of their macroscale equivalent because some physical properties such as the ratio between surface area and volume, diffusion or surface tension do not exhibit linear behaviour from large to small systems. Thus, microfluidic devices should be designed in ways that take advantage of the characteristics of the mixing in a confined space.

One of the most important differences that arise at small length scale is that inertial effects that typically result in turbulence and good mixing on the macroscale are dominated by the viscous effects in microfluidics. The relative importance of inertial to viscous forces for a given flow condition is given by the Reynolds number

$$\mathrm{Re} = \frac{uR}{\nu}, \tag{6.1}$$

where u is the velocity of fluid, R is the channel radius and ν is the kinematic viscosity of the fluid. Due to small channel size (R), microfluidic systems are characterised by low Re, often less than 1. In this case, the fluid flow is laminar, with the streamlines which follow the velocity fields not crossing each other. Since the advective mass transport happens only along the streamlines, no transfer between adjacent layers of fluid is possible. As a result, only diffusion can lead to mass transport normal to the velocity field at low Reynolds number.

Diffusion is the process of spreading molecules from a region of high concentration to one of lower concentration by Brownian motion as described in section 2.1. For an isolated system with an initial non-uniform concentration, a state of homogeneous concentration distribution is ultimately achieved. The mixing time t_{mix} depends on the diffusion coefficient and the striation length l_{st}, which represents the distance over which diffusion acts to homogenise the concentration field. Being a nonlinear process, for normal diffusion time scales quadratically with the distance

according to

$$t_{mix} \sim \frac{l_{st}^2}{D}. \tag{6.2}$$

This clearly shows that a faster mixing can be achieved by reducing the striation length. Figure 6.1 highlights that by halving the diffusion path, the same state of mixing is achieved four times faster. The relative importance of diffusion to advection is given by another dimensionless

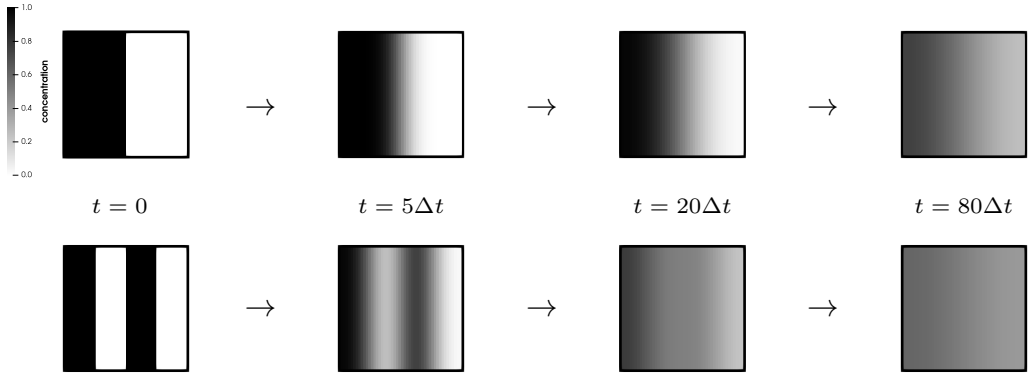

Figure 6.1: Comparison of the concentration fields starting from two different initial distributions of an unmixed solution driven by diffusion. Halving the striation length decreases the mixing time fourfold.

number, i.e. the Péclet number

$$\mathrm{Pe} = \frac{uR}{D}, \tag{6.3}$$

where D is the diffusion coefficient. It can also be viewed as the ratio of characteristic diffusion time (t_{diff}) to the characteristic advection time (t_{adv}).

Considering a cylindrical channel with the radius R and a homogeneous concentration source placed at the entrance at a distance h from the channel walls as illustrated in Figure 6.2. Inside the channel, the typical steady Poiseuille profile develops with the maximum velocity magnitude U_0 and the average flow velocity $u = \frac{U_0}{2}$. Since diffusion is the only contribution to mass transport across tangent fluid layers, the Péclet number normal to the direction of advection is always zero. The diffusion length l_{diff} in a plane perpendicular to the centreline at a distance x from the inlet can be computed according to equation (2.1) as

$$l_{diff}(x) = \sqrt{4Dt_{adv}(x)}. \tag{6.4}$$

The characteristic timescale $t_{adv}(x)$ for a flow to traverse the length x is x/U_0. Thus, l_{diff} is

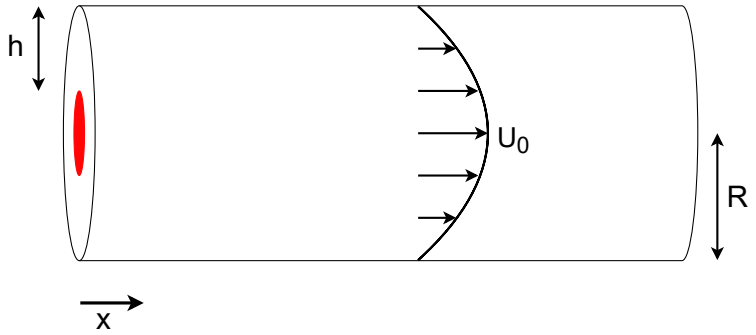

Figure 6.2: Illustration of a cylindrical microchannel with the radius R and the steady Poiseuille flow inside. At the inlet a homogeneous concentration is set at a distance h from the channel walls.

given by

$$l_{diff}(x) = \sqrt{4D\frac{x}{U_0}}. \tag{6.5}$$

Assuming that a high degree of mixing is achieved when the diffusion length scale exceeds the distance to the channel walls, we can introduce the condition for effective mixing

$$\frac{l_{diff}}{h} > 1. \tag{6.6}$$

This is equivalent to requiring a large value of the following dimensionless number

$$\theta_{mix} = 2\sqrt{\frac{Dx}{U_0 h^2}}. \tag{6.7}$$

6.1.2 Mixer performance

One of the most common way to measure mixing is based on the concentration distribution inside the channel. By dividing the volume of interest and computing the deviation of concentration in each sub-volume from the average value, the mixing variance coefficient (MVC) is obtained as follows [137]

$$MVC = \frac{1}{N}\sum_{i=1}^{N}\left(c_i - c_{avg}\right)^2, \tag{6.8}$$

where N is the number of sub-domains, c_i is the concentration in the i^{th} sub-volume and c_{avg} is the average concentration in the whole domain. When the concentration becomes homogeneous,

the value of MVC approaches zero.

To compare systems where the initial total concentration changes, we also consider the coefficient of variation (COV) to quantify the radial mixing. Although it shares the same approach as MVC, COV represents the relative standard deviation and is expressed as [138]

$$COV = \frac{1}{c_{avg}} \sqrt{\frac{\sum_{i=1}^{N} (c_i - c_{avg})^2}{N}}. \tag{6.9}$$

As a result, it is a dimensionless number that makes it possible to compare data sets with widely different c_{avg}. However, if the average value is close to zero, COV approaches infinity and is therefore sensitive to small changes of c_{avg}.

6.2 Simulation setup

Our main goal is to investigate the advection-diffusion of a species inside microchannels and the changes in the mixing performance caused by the passage of a microcapsule. For this, we compare multiple channel setups, incorporating different passive mixer elements and various concentration distributions at the inlet. In this section we present all the systems that are considered, followed by a description of the simulation methods used for modelling the interplay of three different processes: diffusion, fluid flow and the capsule's membrane dynamics.

6.2.1 System geometry

The basic geometry consists of a straight microchannel which is modelled as a cylinder with a radius of 95 μm and a length of 900 μm, which in simulation units corresponds to $R = 19$ and $L = 180$ grid nodes, respectively. Here, one or more substances are being constantly fed into the system where they are transported from one end to another. The patterns considered in this study for the concentration distribution of the species at the inlet are shown in Figure 6.3. First a central circular distribution of the species is used to replicate the inner-layer in the coaxial printing nozzle [139, 140]. Another case that is analysed here consists of placing two fluid flows in a side-by-side manner at the entrance such that the species homogeneously fills half of the channel at inlet. This corresponds to T- and Y-shaped channels [141, 142]. Additionally, the side-by-side distribution can be improved considering the principles stated in Section 6.1.1, by halving the striation length using parallel lamination [143].

The advection is driven by a Poiseuille flow, as illustrated in Figure 6.4, which is the result of

(a) (b) (c)

Figure 6.3: Concentration distribution of the species at the inlet: (a) a central circular shape with a radius of 5 grid nodes, (b) half of the channel is filled and (c) the previous species stream is split in half using parallel lamination.

inflow/outflow boundary conditions for the fluid velocity at the inlet and outlet and a no-slip condition at the walls of the channel. We model the incompressible Newtonian fluid using the properties of water, i.e. density $\rho = 10^3$ kg/m^3 and kinematic viscosity $\nu = 1.2 \cdot 10^{-6}$ m^2/s. Because the channel is of micrometer scale, the flow is usually in the Stokes flow regime, thus, throughout our simulations, the Reynolds number is kept to small values $\mathrm{Re} \ll 1$. For the diffusion, we consider the simple case of oxygen in water which has the diffusion coefficient $D = 2 \cdot 10^{-9}$ m^2/s around room temperature [144]. Furthermore, we set $\mathrm{Pe} = 10$ for every system that is simulated.

To study the mixing throughout the channel, we consider three additional setups as displayed in Figure 6.5. First, an obstacle in form of a sphere with the radius $r = 12$ is fixed at $x = 30$ from the inlet. Then, we test the impact of the shape of the system by using a wavy channel constructed as sinusoidal wave [145]. Lastly, we introduce synthetic microcapsules which are impermeable for the fluid and the species and we flow them through the channel as another form of a mixer element. Initially, they are modelled as spheres having the radii $r = 12$ and are then deformed by the hydrodynamic forces. To characterise the deformation of the capsules, we introduce another dimensionless number, i.e. the capillary number Ca, representing the relation between viscous forces and the surface tension forces acting across the membrane. It is defined as

$$\mathrm{Ca} = \frac{\mu u}{\sigma}, \tag{6.10}$$

where μ is the dynamic viscosity of the fluid and σ is the surface tension.

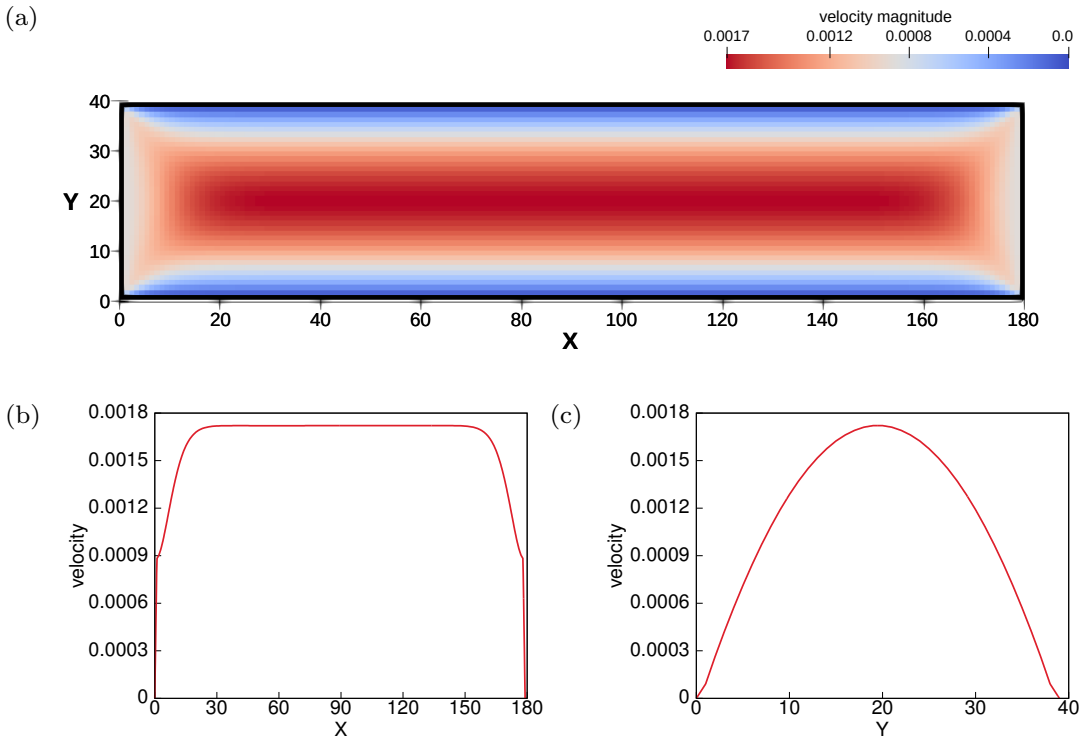

Figure 6.4: (a) The steady flow field inside the microchannel with (b) the longitudinal profile along the centreline and (c) the transversal profile at $x = 120$.

6.2.2 Simulation methods

Considering the most complex case where the mixing is not only influenced by the diffusion of the species and the flow field inside the channel but also by the moving impermeable capsule, one has to pay attention to the coupling of three different phenomena: advection, diffusion and the membrane dynamics of the immersed boundary. Given the time dependent velocity field of the fluid and the continuous movement of the capsule, the coupled solvers for the flow field and the concentration field have to be run at each time step.

Fluid dynamics

We start by considering the simulation of the fluid dynamics. The flow fields are computed by employing the LBM implementation for the NSE solver from the open source software package ESPResSo [82] as described in section 3.3.1. Due to limitations in the method used for modeling the capsule and the ADE solver extension that are later discussed, we must resort to using inflow/outflow boundary conditions to drive the advection. Thus, the velocity u is imposed on

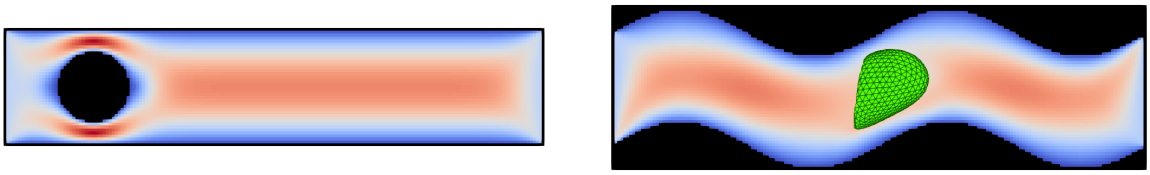

(a) (b)

Figure 6.5: The steady flow field inside (a) a straight microchannel with a rigid sphere placed at $x = 30$ and (b) a wavy microchannel with a deformable synthetic microcapsule flowing through it.

the boundaries representing the inlet and outlet. The other walls have a no-slip condition which leads to the formation of the parabolic flow profile in the steady-state with the average velocity u. Figure 6.4 shows the effect introduced by the chosen BC at inlet and outlet, with the Poiseuille profile not being fully developed close to the two ends of the channel, even in the steady-state.

Membrane dynamics

The coupling between fluid and the capsule is achieved via the framework of the immersed-boundary method (IBM) [146, 147] which was already successfully implemented in ESPResSo [148–150]. The IBM consists of two main steps: the elastic forces acting on the capsule are passed to the fluid while the massless capsule is advected with the local fluid velocity due to no-slip boundary condition. The inlet and outlet boundaries are considered periodic for the capsule. It should be noted here that due to technical issues of the implementation used for this method, we avoid using a pressure gradient within the channel. As a result, generating the advection requires us to prescribe a certain average flow velocity as previously mentioned.

The membrane of the capsule is represented by an infinitely thin elastic sheet, discretized by a set of nodes connected by triangles as illustrated in Figure 6.6. The triangulation of the surface is performed using successive refinements of an icosahedron as described by Krüger et al. [151]. The shell of the capsule usually consists of an elastic polymer which can vary its area through stretching caused by hydrodynamic forces. Therefore, its mechanics can be described using the Neo-Hookean framework [152, 153]. Employing a similar setup, where an initially undeformed capsule is flowing through a cylindrical channel, Chu et al. have computed the critical capillary number beyond which a capsule modeled by the Neo-Hookean law does not reach a steady state for a given size [154]. In our case, the typical value $\mathrm{Ca} = 0.05$ is much lower than the threshold for the size ratio $r/R = 0.63$ between the radius of the spherical capsule and the radius of the

channel.

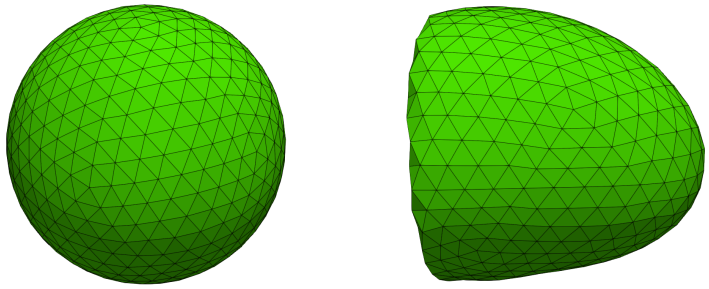

(a) (b)

Figure 6.6: The geometry of the triangulated infinitely thin elastic membrane used in the simulations: (a) the initially spherical capsule is placed in a Poiseuille flow and (b) it deforms axisymetrically.

Species transport

Our focus in this study is represented by species which diffuse inside the channel and are advected by the flow field computed with the LBM at each time step, while also being influenced by the movement of the capsule. To solve the ADE which describe their transport throughout the system, we have opted to extend ESPResSo with the finite volume method presented in section 3.1. For the spatial discretization we use the same lattice employed by the LBM for the flow simulation.

The boundaries introduced for the fluid are also inherited, with different conditions available to be assigned to them. We start with the walls forming the channel which are considered impermeable and thus, a zero flux is imposed. At the inlet, a fix concentration C_0 is set for the nodes that form the desired pattern, while, for simplicity, the rest are considered impermeable. Analysing the longitudinal flow profile in Figure 6.4 (b), it can be noticed that the advective flux is influenced by the changing velocity near the two ends. As a result, the amount of species that are transported from the inlet is less than the expected value. At the outlet it is often assumed that the concentration does not change along the flow direction, which translates to a zero gradient boundary condition. However, due to the aforementioned effect, the advective flux decrease close to the exit, which would lead to a constant accumulation of concentration in that region. Therefore, we choose to impose a fix concentration $C = 0$ at the outlet which prevents this behaviour.

6.3 Numerical results

6.3.1 Coaxial distribution

We start our investigation with an empty straight channel having the coaxial setup at inlet where the species is homogeneously distributed in a circular shape with the radius of 5 grid nodes as displayed in Figure 6.3(a). To assess the impact that the distortions of the flow field near the inlet and outlet, highlighted in Figure 6.4, have on the mixing process, we have additionally simulated the advection-diffusion of the species inside the same system using the LBM described in section 3.3.2. For the LBM, besides being able to use a pressure gradient to generate the Poiseuille flow field, we have also imposed a zero gradient for the concentration at the outlet to replicate the classical outflow boundary condition. Figure 6.7 shows a significant discrepancy in the MVC results between the two methods close to the inlet, which can be attributed to a larger quantity of species being fed into the channel when using LBM, compared to the implementation of FVM in ESPResSo. However, when using COV to measure the mixing, a very good agreement is obtained. Therefore, our extended ESPResSo package proves to be a useful tool at least for qualitative studies of mixing performance inside various systems.

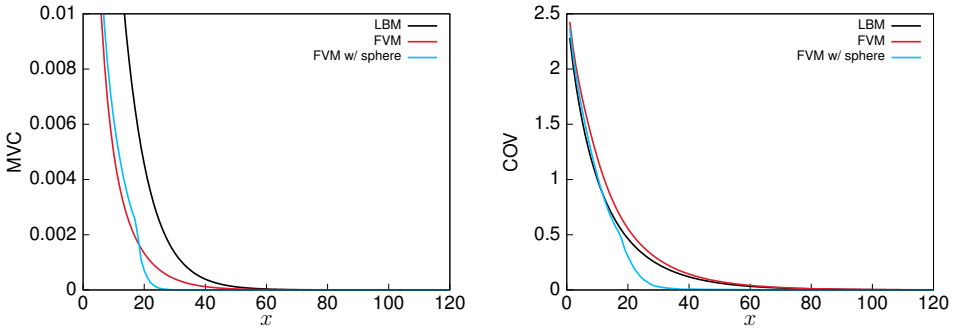

Figure 6.7: Mixing in a straight microchannel with the coaxial inlet concentration distribution, measured using (a) MVC and (b) COV. The case of adding a spherical obstacle at $x = 30$ (Figure 6.5(a)) is also considered.

Using the analytical analysis from section 6.1.1, we can evaluate the dimensionless number θ_{mix} for our current setup to estimate the distance required for efficient mixing to be obtained. For the coaxial inlet boundary condition $h = 14$, which means that $\theta_{mix} > 1$ is satisfied for $x > 52$. The numerical results presented in Figure 6.7(b) show indeed that a good mixing (COV $< 5\%$) is achieved beyond $x = 56$, while a complete mixing (COV $< 1\%$) occurs from $x = 84$. The

addition of a fix sphere with the radius $r = 12$ at $x = 30$ from the inlet, significantly accelerates this process such that mixing is completed from $x = 35$.

Next, we turn our attention to the wavy channel illustrated in Figure 6.5(b). The low Re regime makes the results obtained with this geometry almost indistinguishable from the ones produced by the empty straight channel. Figure 6.8 shows that in both systems the total mixing occurs at the same distance. A more interesting case is represented by the addition of the microcapsule which is flowing though out the channel. After the time required in the previous case to reach the steady-state, we measure the mixing inside the system when the deformed capsule is in the second half of the channel. The first thing that we notice is the disturbance in the mixing process that occurs around the position of the capsule which can clearly be seen in Figure 6.8(b). This heterogeneity is characterised by two peaks, each corresponding exactly to the front and to the back of the capsule, respectively. To explain this behaviour we consider the passage of the capsule from the entrance of the channel to the current position. Close to the inlet, the species is not well mixed and, as a result, small volumes of high concentration, that are either right in front or behind the capsule, are being advected together with it. The membrane is impermeable for the species, and thus the capsule hampers the diffusion from these pockets of higher concentration compared with the regions next to the walls, where transport is less obstructed. To further highlight this, we note that the mixing increases from the front or from the back of the capsule towards the median part where a high homogeneity is achieved. This point corresponds to the transversal cross section of the channel that has the largest area occupied by the capsule. Although this disturbance in the mixing extends more then the length of the capsule, it only occurs on short distances, such that closer to the inlet no effect is measured compared to the case of the empty channel.

6.3.2 Side-by-side distribution

We now change the pattern of the species distribution at the inlet to the side-by-side configuration as illustrated in Figure 6.3(b). Given the fact that the species fill exactly half of the cross section, this time we may consider the radial distance for the diffusion to correspond to the radius of the channel, such that $h = 19$. As a result, the analytical condition $\theta_{mix} > 1$, required to obtain mixing of the species, is fulfilled for $x > 95$. This result suggests that the distance at which a homogeneous distribution can be observed significantly increases. Therefore we have opted to extend the length of the straight channel to 240 grid nodes for this simulation. The computational results displayed in Figure 6.9 show that a good mixing (COV $< 5\%$) occurs from $x = 135$, while

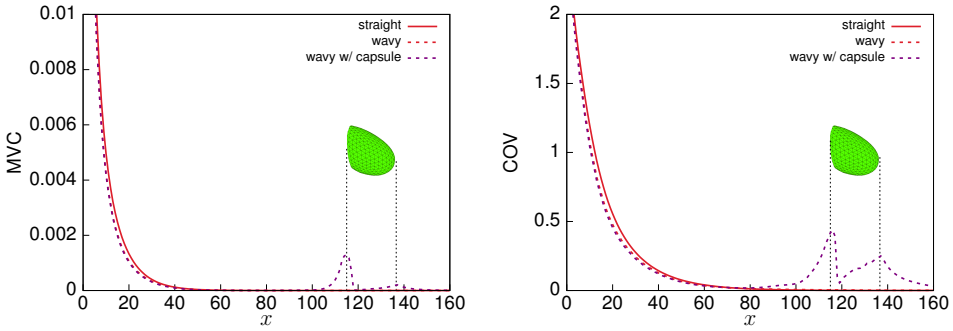

(a) (b)

Figure 6.8: Comparison of the mixing performance between an empty straight channel, an empty wavy channel and an wavy channel with a microcapsule flowing through it. The results are measured after the steady-state is reached, using (a) MVC and (b) COV. The coaxial setup is used as a boundary condition for the concentration at the inlet.

complete mixing (COV $< 1\%$) is achieved beyond $x = 212$. Due to the complete separation of the species into the two halves of the channel at the inlet, this time the addition of the fixed sphere close to the entrance increases the distance required for the mixing process.

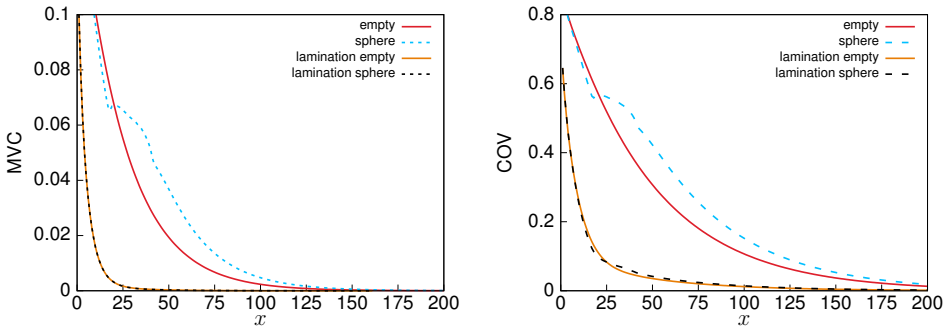

(a) (b)

Figure 6.9: Comparison of the mixing performance between the simple side-by-side (Figure 6.3(b)) and the laminar (Figure 6.3(c)) concentration distribution at the inlet in a straight channel using (a) MVC and (b) COV. The case of adding a spherical obstacle at $x = 30$ (Figure 6.5(a)) is also considered.

An enhancement in the mixing performance can be achieved through the process of parallel lamination. Each of two different concentration streams from the inlet (Figure 6.3(b)) are divided into two laminae such that the distribution illustrated in Figure 6.3(c) is obtained. According to equation 6.2, this should lead to mixing that is faster by a factor of four. Due to the linearity between time and distance, the length required for the same level of homogeneity to be

achieved should also be only a quarter of the previous value. Figure 6.9 shows the improvement characteristic to this setup, with a good mixing of COV $< 5\%$ being obtained from $x = 37$. However, complete mixing (COV $< 1\%$) occurs only beyond $x = 108$, which is approximately half the distance required in the initial case. This discrepancy compared to the expected value can be explained by the lack of periodic boundaries in the direction normal to the laminae, and therefore, the particles next to the walls require more time to reach the depleted zones, which becomes noticeable when total mixing is sought. We also note that in the case of parallel lamination, the fixed sphere has almost no impact due to the fact that the species are more evenly distributed at the inlet.

For the study of the wavy channel geometry effects, we revert to the initial grid length of 180 nodes due to computational reasons. Figure 6.10 shows that for the side-by-side concentration distribution, the wavy channel enhances mixing such that a value of COV $< 5\%$ is reached from $x = 108$. The reason why the difference is noticeable now may be attributed to the fact that the species is placed closer to the channel walls at the inlet, unlike the coaxial distribution where it is concentrated in the centre.

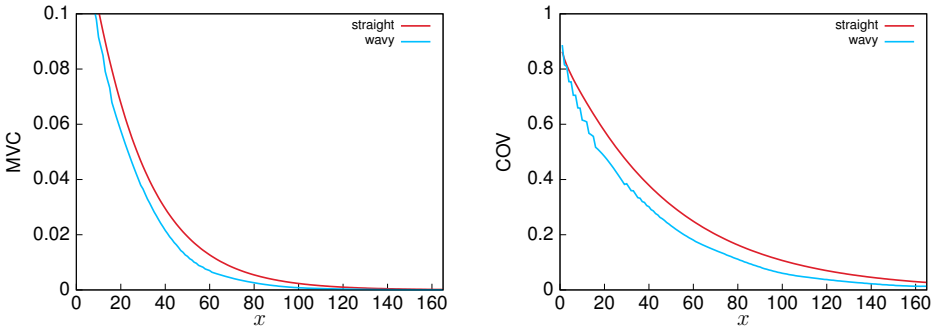

(a) (b)

Figure 6.10: Comparison of the mixing performance between the straight and the wavy channel geometries using (a) MVC and (b) COV.

Next, we introduce the deformable microcapsule into the wavy channel and measure the mixing level when it reaches the same position that was analysed for the coaxial distribution. Again, in Figure 6.11 we notice the same effect around the capsule as described for the previous inlet concentration distribution. The interesting aspect is that the same level of heterogeneity is induced by the capsule, for both the simple side-by-side and the parallel lamination pattern, even though a better mixing is achieved for the latter in the absence of the perturbation. Moreover, for all three cases of concentration distribution considered in our study, the peaks in front of

the capsule and behind it have almost exactly the same values of COV = 25% at $x = 137$ and COV = 44% at $x = 116$, respectively.

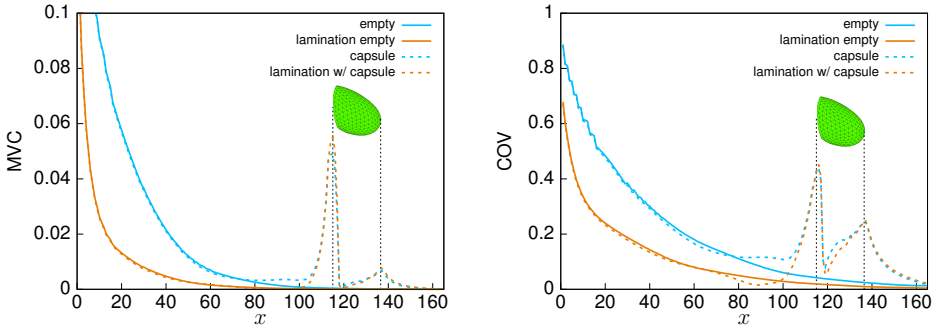

(a) (b)

Figure 6.11: Mixing performance in a wavy channel with and without a microcapsule flowing though it measured using (a) MVC and (b) COV. Both the simple side-by-side (Figure 6.3(b)) and the parallel lamination (Figure 6.3(c)) concentration distributions are considered for the inlet.

Chapter 7

Conclusions and outlook

In this thesis, advection-diffusion-reaction processes were studied in the light of two key research areas, i.e. chemical synthesis and microfluidics. Using numerical simulations and developing simple theoretical models, we were able to offer new insight into the properties and characteristics of novel techniques that have emerged in these fields. For this, we have implemented three different solver, namely LBM, RWPT and FVM, which, coupled with a fluid solver, allowed us to track the evolution of the concentration fields in various systems. Moreover, we have shown that a better understanding of the reaction processes can be gained by developing kinetics models tailored for the systems of interest. In this regard, two new tools have been proposed for studying reactions with an induction period by extending the classical first-order and second-order kinetics models with an additional parameter.

The catalytic performance of gold nanoparticles was analysed in chapter 4. First, we investigated the impact that the size of the particles has on the reaction process from the perspective of the advection-diffusion mechanisms that describe the reactant transport. To compare systems with different particle sizes but constant total surface areas, we have employed a lattice Boltzmann scheme and a random walk particle model. The latter allowed for modelling the anisotropic diffusion induced by the higher hydrodynamic resistance close to the surface of the nanoparticles. All our results showed that the reaction rates are independent of the particle size, thus ruling out the surface-modified diffusion of the reactant as a possible explanation for the change in the catalytic performance that was observed in the experiments.

Furthermore, gold nanoparticles can be embedded on patchy nonwovens in order to prevent their aggregation and their particular catalytic activity was also studied. To account for the induction period due to the swelling of the patches in the reactants, we have proposed an extended pseudo-first order kinetics model. The novelty is represented by the introduction of the accessibility parameter r which determines the rate at which the reactants become available to the catalytic sites. Using this model we were able to accurately fit the experimental results over the full time range which revealed that both the geometry and the composition of the patches affect the catalytic performance by having different accessibility rates.

Chapter 5 is dedicated to the study of one-pot multi-step reactions using Wolf-Lamb-type catalysts. Initially we analysed the kinetics of a two-step reaction with different type of catalytic sites. The measured reaction rates exhibited a slow start of the second reaction which could not be replicated using the classical second order kinetics model. Therefore, we have introduced an additional parameter Δt in the equations that account for the second step. The improvement in the fitting suggested that the delayed start is caused by the lack of intermediate species available

in the beginning and not by some intrinsic mechanisms.

The efficiency of flow-through reactors using fibrous membranes as catalytic carriers for cascade reactions was then considered. Using the lattice Boltzmann method, we were able to simulate the interplay of the three mechanisms (advection, diffusion and reaction) that describe such systems. The reactor efficiency was computed as a function of two dimensionless parameters: the Péclet number which measures the ratio between the advective and diffusive transport and the Damköhler number which gives the ration between reactive and diffusive time scales. The membrane geometry was also taken into account, with the side-by-side fiber morphology yielding better performances due to the close proximity of the reaction sites and thus supporting the recent experimental efforts to immobilise two catalysts on a single fiber. Additionally, we have also developed an approximative theoretical model, characterised by a single adjustable parameter Δ, which showed a good agreement with the numerical results. Thus, our analytical model can be a useful tool for a quick estimation of the efficiency of a cascade reaction system using fibrous membranes as catalytic carriers. For further studies, our simulation code can be used for modelling more complex morphologies, such as mesoporous and core-shell fibers, as well as different fiber mats configurations. Another important development would be the implementation of an upscaling step which would allow our computational model to simulate the behaviour of the full centimeter-scale flow chamber. For this step, the same ADRE equation would be employed, but the diffusion coefficient and the reaction rate constant are replaced with the effective values which incorporate the influence of the individual fiber arrangement and morphology, computed using the fiber-scale method presented here.

The last part of this work (chapter 6) focuses on the study of the mixing process inside microchannels. The combined lattice Boltzmann/immersed boundary method has been extended with a finite volume method to be able to compute the coupled flow field, membrane dynamics and concentration field throughout the channel. Using coaxial and side-by-side concentration distributions of the species at the inlet, we were able to compute the distance required for an effective mixing. Passive elements to enhance homogeneity, such as channel geometry and lamination of the species stream, were considered, with the latter showing a significant reduction in the mixing length. A novel and significant result was the influence of a suspended deformable microcapsule on the species distribution. Notably, the mixture uniformity was worsened around the position of the capsule, the highest variations being recorded right in front of and behind it. This behavior was attributed to the volumes of unmixed species from the inlet being transported with the capsule, while their diffusion is blocked by the impermeable membrane. It was also

shown that the relative variance in the mixing induced by the suspended capsule has the same value for all concentration distributions that were considered at the inlet. Our study can be extended by considering a wider range of parameters for the fluid and capsule properties, as well as different mixers, such as herringbone groove channel [155, 156] and alternate injection design [157]. Furthermore, in the framework of ESPResSo package, the LBM/IBM implementation has already been successfully used to simulate suspensions of red blood cells [149, 158]. Therefore, our extension can be used to model the transport of molecules (e.g. oxygen, drug carrier) in blood vessels and offer a deeper insight into their dispersion from the point of release to the channel walls [159].

References

[1] A. Bancaud, G. Wagner, K. D. Dorfman and J.-L. Viovy, Measurement of the surface concentration for bioassay kinetics in microchannels, *Analytical Chemistry* **77**, 833 (2004)

[2] M. Leconte, J. Martin, N. Rakotomalala, D. Salin and Y. C. Yortsos, Mixing and reaction fronts in laminar flows, *The Journal of Chemical Physics* **120**, 7314 (2004)

[3] T. Yanagita and K. Kaneko, Modeling and characterization of cloud dynamics, *Physical Review Letters* **78**, 4297 (1997)

[4] D. Buske, M. T. Vilhena, T. Tirabassi and B. Bodmann, Air pollution steady-state advection-diffusion equation: The general three-dimensional solution, *Journal of Environmental Protection* **03**, 1124 (2012)

[5] C. B. Connor, B. E. Hill, B. Winfrey, N. M. Franklin and P. C. L. Femina, Estimation of volcanic hazards from tephra fallout, *Natural Hazards Review* **2**, 33 (2001)

[6] M.-C. Prima, T. Duchesne, A. Fortin, L.-P. Rivest and D. Fortin, Combining network theory and reaction–advection–diffusion modelling for predicting animal distribution in dynamic environments, *Methods in Ecology and Evolution* **9**, 1221 (2018)

[7] M. Haruta, T. Kobayashi, H. Sano and N. Yamada, Novel gold catalysts for the oxidation of carbon monoxide at a temperature far below 0 °c, *Chemistry Letters* **16**, 405 (1987)

[8] M. Haruta, When gold is not noble: Catalysis by nanoparticles, *The Chemical Record* **3**, 75 (2003)

[9] M. Stratakis and H. Garcia, Catalysis by supported gold nanoparticles: Beyond aerobic oxidative processes, *Chemical Reviews* **112**, 4469 (2012)

[10] T. Ishida, T. Murayama, A. Taketoshi and M. Haruta, Importance of size and contact structure of gold nanoparticles for the genesis of unique catalytic processes, *Chemical Reviews* **120**, 464 (2020)

[11] L. Dykman and N. Khlebtsov, Gold nanoparticles in biomedical applications: recent advances and perspectives, *Chem. Soc. Rev.* **41**, 2256 (2012)

[12] E. C. Dreaden, M. A. Mackey, X. Huang, B. Kang and M. A. El-Sayed, Beating cancer in multiple ways using nanogold, *Chem. Soc. Rev.* **40**, 3391 (2011)

[13] E. C. Dreaden, A. M. Alkilany, X. Huang, C. J. Murphy and M. A. El-Sayed, The golden age: gold nanoparticles for biomedicine, *Chem. Soc. Rev.* **41**, 2740 (2012)

[14] I. Venditti, Gold nanoparticles in photonic crystals applications: A review, *Materials* **10**, 97 (2017)

[15] C.-C. Huang, Z. Yang, K.-H. Lee and H.-T. Chang, Synthesis of highly fluorescent gold nanoparticles for sensing mercury(ii), *Angewandte Chemie International Edition* **46**, 6824 (2007)

[16] K. Saha, S. S. Agasti, C. Kim, X. Li and V. M. Rotello, Gold nanoparticles in chemical and biological sensing, *Chem. Soc. Rev.* **112**, 2739 (2012)

[17] L. Shi, L. Zhu, J. Guo, L. Zhang, Y. Shi et al., Self-assembly of chiral gold clusters into crystalline nanocubes of exceptional optical activity, *Angewandte Chemie (International ed. in English)* **56**, 15397—15401 (2017)

[18] S. Kundu, L. Peng and H. Liang, A new route to obtain high-yield multiple-shaped gold nanoparticles in aqueous solution using microwave irradiation, *Inorganic Chemistry* **47**, 6344 (2008)

[19] M.-C. Daniel and D. Astruc, Gold nanoparticles: assembly, supramolecular chemistry, quantum-size-related properties, and applications toward biology, catalysis, and nanotechnology, *Chemical Reviews* **104**, 293 (2004)

[20] T. K. Sau, A. Pal, N. Jana, Z. Wang and T. Pal, Size controlled synthesis of gold nanoparticles using photochemically prepared seed particles, *Journal of Nanoparticle Research* **3**, 257 (2001)

[21] X. Zhou, W. Xu, G. Liu, D. Panda and P. Chen, Size-dependent catalytic activity and dynamics of gold nanoparticles at the single-molecule level, *Journal of the American Chemical Society* **132**, 138 (2009)

[22] P. Suchomel, L. Kvitek, R. Prucek, A. Panacek, A. Halder et al., Simple size-controlled synthesis of au nanoparticles and their size-dependent catalytic activity, *Scientific Reports* **8** (2018)

[23] S. Kundu, S. Lau and H. Liang, Shape-controlled catalysis by cetyltrimethylammonium bromide terminated gold nanospheres, nanorods, and nanoprisms, *The Journal of Physical Chemistry C* **113**, 5150 (2009)

[24] S. M. Ansar and C. L. Kitchens, Impact of gold nanoparticle stabilizing ligands on the colloidal catalytic reduction of 4-nitrophenol, *ACS Catalysis* **6**, 5553 (2016)

[25] R. Fenger, E. Fertitta, H. Kirmse, A. F. Thünemann and K. Rademann, Size dependent catalysis with ctab-stabilized gold nanoparticles, *Phys. Chem. Chem. Phys.* **14**, 9343 (2012)

[26] J. Piella, F. Merkoçi, A. Genç, J. Arbiol, N. G. Bastús et al., Probing the surface reactivity of nanocrystals by the catalytic degradation of organic dyes: the effect of size, surface chemistry and composition, *J. Mater. Chem. A* **5**, 11917 (2017)

[27] I. Ro, J. Resasco and P. Christopher, Approaches for understanding and controlling interfacial effects in oxide-supported metal catalysts, *ACS Catalysis* **8**, 7368 (2018)

[28] Y. Wang, H. Arandiyan, J. Scott, A. Bagheri, H. Dai et al., Recent advances in ordered meso/macroporous metal oxides for heterogeneous catalysis: a review, *J. Mater. Chem. A* **5**, 8825 (2017)

[29] M. Massaro, C. G. Colletti, G. Lazzara, S. Milioto, R. Noto et al., Halloysite nanotubes as support for metal-based catalysts, *J. Mater. Chem. A* **5**, 13276 (2017)

[30] S. Navalon, A. Dhakshinamoorthy, M. Alvaro and H. Garcia, Metal nanoparticles supported on two-dimensional graphenes as heterogeneous catalysts, *Coordination Chemistry Reviews* **312**, 99 (2016)

[31] H. R. Moon, D.-W. Lim and M. P. Suh, Fabrication of metal nanoparticles in metal–organic frameworks, *Chem. Soc. Rev.* **42**, 1807 (2013)

[32] A. Dhakshinamoorthy, A. M. Asiri and H. Garcia, Metal organic frameworks as versatile hosts of au nanoparticles in heterogeneous catalysis, *ACS Catalysis* **7**, 2896 (2017)

[33] S. Bhattacharyya, D. Samanta, S. Roy, V. P. Haveri Radhakantha and T. K. Maji, In situ stabilization of au and co nanoparticles in a redox-active conjugated microporous polymer matrix: Facile heterogeneous catalysis and electrocatalytic oxygen reduction reaction activity, *ACS Applied Materials & Interfaces* **11**, 5455 (2019)

[34] J. He, S. Razzaque, S. Jin, I. Hussain and B. Tan, Efficient synthesis of ultrafine gold nanoparticles with tunable sizes in a hyper-cross-linked polymer for nitrophenol reduction, *ACS Applied Nano Materials* **2**, 546 (2019)

[35] J. Schöbel, C. Hils, A. Weckwerth, M. Schlenk, C. Bojer et al., Strategies for the selective loading of patchy worm-like micelles with functional nanoparticles, *Nanoscale* **10**, 18257 (2018)

[36] J. Schöbel, M. Burgard, C. Hils, R. Dersch, M. Dulle et al., Bottom-up meets top-down: Patchy hybrid nonwovens as an efficient catalysis platform, *Angewandte Chemie International Edition* **56**, 405 (2017)

[37] L. Qi, Y. Wei, L. Xu and Z. Liu, Reaction behaviors and kinetics during induction period of methanol conversion on HZSM-5 zeolite, *ACS Catalysis* **5**, 3973 (2015)

[38] C. Hils, M. Dulle, G. Sitaru, S. Gekle, J. Schöbel et al., Influence of patch size and chemistry on the catalytic activity of patchy hybrid nonwovens, *Nanoscale Adv.* **2**, 438 (2020)

[39] J. Lu, J. Dimroth and M. Weck, Compartmentalization of Incompatible Catalytic Transformations for Tandem Catalysis, *J. Am. Chem. Soc.* **137**, 12984 (2015)

[40] I. Wheeldon, S. D. Minteer, S. Banta, S. C. Barton, P. Atanassov et al., Substrate channelling as an approach to cascade reactions, *Nature Chem* **8**, 299 (2016)

[41] Z.-Q. Wu, Z.-Q. Li, J.-Y. Li, J. Gu and X.-H. Xia, Contribution of convection and diffusion to the cascade reaction kinetics of beta-galactosidase/glucose oxidase confined in a microchannel, *Phys. Chem. Chem. Phys.* **18**, 14460 (2016)

[42] V. Boucard, Kinetic Study of the Knoevenagel Condensation Applied to the Synthesis of Poly[bicarbazolylene- alt-phenylenebis(cyanovinylene)]s, *Macromolecules* **34**, 4308 (2001)

[43] B. Helms, S. J. Guillaudeu, Y. Xie, M. McMurdo, C. J. Hawker et al., One-Pot Reaction Cascades Using Star Polymers with Core-Confined Catalysts, *Angew. Chem. Int. Ed.* **44**, 6384 (2005)

[44] S. Agarwal, J. H. Wendorff and A. Greiner, Chemistry on Electrospun Polymeric Nanofibers: Merely Routine Chemistry or a Real Challenge?, *Macromol. Rapid Commun.* **31**, 1317 (2010)

[45] M. O. Pretscher, S. Gekle and S. Agarwal, Wolf–Lamb-type Ctalysis in One Pot Using electrospun Polymeric Catalyst Membranes, *Macromolecular Rapid Communications* **40**, 1900148 (2019)

[46] R. Samson and J. M. Deutch, Exact solution for the diffusion controlled rate into a pair of reacting sinks, *J. Chem. Phys.* **67**, 847 (1977)

[47] M. Castellana, M. Z. Wilson, Y. Xu, P. Joshi, I. M. Cristea et al., Enzyme clustering accelerates processing of intermediates through metabolic channeling, *Nature Biotechnology* **32**, 1 (2014)

[48] H. Li, M. Ye and Z. Liu, A multi-region model for reaction–diffusion process within a porous catalyst pellet, *Chem. Eng. Sci.* **147**, 1 (2016)

[49] S. Arcidiacono, J. Mantzaras and I. V. Karlin, Lattice Boltzmann simulation of catalytic reactions, *Phys. Rev. E* **78**, 46711 (2008)

[50] Y. Abdollahzadeh, Z. Mansourpour, H. Moqtaderi, S. N. Ajayebi and M. M. Montazeri, A molecular collision based lattice boltzmann method for simulation of homogeneous and heterogeneous reactions, *Chemical Engineering Research and Design* **136**, 456 (2018)

[51] P. Bauler, G. Huber, T. Leyh and J. A. McCammon, Channeling by Proximity: The Catalytic Advantages of Active Site Colocalization Using Brownian Dynamics, *J. Phys. Chem. Lett.* **1**, 1332 (2010)

[52] G. Whitesides, The lab finally comes to the chip!, *Lab on a Chip* **14**, 3125 (2014)

[53] A. Nagaki, Y. Tomida and J. ichi Yoshida, Microflow-system-controlled anionic polymerization of styrenes, *Macromolecules* **41**, 6322 (2008)

[54] Y. Liu and X. Jiang, Why microfluidics? merits and trends in chemical synthesis, *Lab on a Chip* **17**, 3960 (2017)

[55] J. Kim, P. Gutruf, A. M. Chiarelli, S. Y. Heo, K. Cho et al., Miniaturized battery-free wireless systems for wearable pulse oximetry, *Advanced Functional Materials* **27**, 1604373 (2016)

[56] T. Komatsu, M. Maeki, A. Ishida, H. Tani and M. Tokeshi, Paper-based device for the facile colorimetric determination of lithium ions in human whole blood, *ACS Sensors* **5**, 1287 (2020)

[57] M. Maeki, S. Uno, A. Niwa, Y. Okada and M. Tokeshi, Microfluidic technologies and devices for lipid nanoparticle-based RNA delivery, *Journal of Controlled Release* **344**, 80 (2022)

[58] R. Levato, T. Jungst, R. G. Scheuring, T. Blunk, J. Groll et al., From shape to function: The next step in bioprinting, *Advanced Materials* **32**, 1906423 (2020)

[59] Y. K. Suh and S. Kang, A review on mixing in microfluidics, *Micromachines* **1**, 82 (2010)

[60] C.-Y. Lee, W.-T. Wang, C.-C. Liu and L.-M. Fu, Passive mixers in microfluidic systems: A review, *Chemical Engineering Journal* **288**, 146 (2016)

[61] G. Cai, L. Xue, H. Zhang and J. Lin, A review on micromixers, *Micromachines* **8** (2017)

[62] T. W. Lim, Y. Son, Y. J. Jeong, D.-Y. Yang, H.-J. Kong et al., Three-dimensionally crossing manifold micro-mixer for fast mixing in a short channel length, *Lab Chip* **11**, 100 (2011)

[63] M. Javaid, T. Cheema and C. Park, Analysis of passive mixing in a serpentine microchannel with sinusoidal side walls, *Micromachines* **9**, 8 (2017)

[64] H. S. Heo and Y. K. Suh, Enhancement of stirring in a straight channel at low reynolds-numbers with various block-arrangement, *Journal of Mechanical Science and Technology* **19**, 199 (2005)

[65] A. S. Kim, Complete analytic solutions for convection-diffusion-reaction-source equations without using an inverse laplace transform, *Scientific Reports* **10** (2020)

[66] T. Krüger, H. Kusumaatmaja, A. Kuzmin, O. Shardt, G. Silva et al., *The Lattice Boltzmann Method - Principles and Practice*, Springer (2016)

[67] L. J. Perez, J. J. Hidalgo and M. Dentz, Reactive random walk particle tracking and its equivalence with the advection-diffusion-reaction equation, *Water Resources Research* **55**, 847 (2019)

[68] S. Succi, A. Gabrielli, G. Smith and E. Kaxiras, Chemical efficiency of reactive microflows with heterogeneous catalysis: a lattice Boltzmann study, *Eur. Phys. J. AP* **16**, 71 (2001)

[69] T. Bennett, *Transport by Advection and Diffusion*, Wiley Global Education (2012)

[70] R. Byron Bird, W. E. Stewart and E. N. Lightfoot, *Transport phenomena*, Wiley (2006)

[71] P. Mörters and Y. Peres, *Brownian Motion*, Cambridge University Press (2010)

[72] A. Einstein, *Investigations on the Theory of the Brownian Movement*, Dover Books on Physics, Dover Publications (1956)

[73] M. von Smoluchowski, Zur kinetischen theorie der brownschen molekularbewegung und der suspensionen, *Annalen der Physik* **326**, 756 (1906)

[74] A. Fick, On liquid diffusion, *Journal of Membrane Science* **100**, 33 (1995)

[75] P. L. Bhatnagar, E. P. Gross and M. Krook, A model for collision processes in gases. i. small amplitude processes in charged and neutral one-component systems, *Phys. Rev.* **94**, 511 (1954)

[76] R. J. LeVeque, *Finite Volume Methods for Hyperbolic Problems*, Cambridge Texts in Applied Mathematics, Cambridge University Press (2002)

[77] J. H. Ferziger and M. Perić, *Computational Methods for Fluid Dynamics*, Springer Berlin Heidelberg (2002)

[78] H. Risken, *Fokker-Planck Equation*, Springer Berlin Heidelberg, Berlin, Heidelberg, pp. 63–95 (1996)

[79] J. Hardy, Y. Pomeau and O. de Pazzis, Time evolution of a two-dimensional model system. i. invariant states and time correlation functions, *Journal of Mathematical Physics* **14**, 1746 (1973)

[80] S. Harris, *An introduction to the theory of the Boltzmann equation*, Dover (2004)

[81] X. He, S. Chen and G. D. Doolen, A novel thermal model for the lattice boltzmann method in incompressible limit, *Journal of Computational Physics* **146**, 282 (1998)

[82] A. Arnold, O. Lenz, S. Kesselheim, R. Weeber, F. Fahrenberger et al., Espresso 3.1: Molecular dynamics software for coarse-grained models, in M. Griebel and M. A. Schweitzer, eds., *Meshfree Methods for Partial Differential Equations VI*, Springer Berlin Heidelberg, Berlin, Heidelberg (2013), pp. 1–23

[83] X. Shan, Simulation of rayleigh-bénard convection using a lattice boltzmann method, *Phys. Rev. E* **55**, 2780 (1997)

[84] Q. Kang, P. C. Lichtner and D. Zhang, Lattice boltzmann pore-scale model for multicomponent reactive transport in porous media, *Journal of Geophysical Research: Solid Earth* **111** (2006)

[85] S. Ponce Dawson, S. Chen and G. Doolen, Lattice boltzmann computations for reaction-diffusion equations, *Journal of Chemical Physics* **98**, 1514 (1993)

[86] R. Blaak and P. M. Sloot, Lattice dependence of reaction-diffusion in lattice boltzmann modeling, *Computer Physics Communications* **129**, 256 (2000)

[87] I. Ginzburg, Equilibrium-type and link-type lattice boltzmann models for generic advection and anisotropic-dispersion equation, *Advances in Water Resources* **28**, 1171 (2005)

[88] M. Latini and A. J. Bernoff, Transient anomalous diffusion in poiseuille flow, *J. Fluid Mech.* **441**, 399 (2001)

[89] C. H. Christensen and J. K. Nørskov, Green gold catalysis, *Science* **327**, 278 (2010)

[90] A. Wittstock, V. Zielasek, J. Biener, C. M. Friend and M. Bäumer, Nanoporous gold catalysts for selective gas-phase oxidative coupling of methanol at low temperature, *Science* **327**, 319 (2010)

[91] R. Meyer, C. Lemire, S. K. Shaikhutdinov and H. J. Freund, Surface chemistry of catalysis by gold, *Gold Bulletin* **37**, 72 (2004)

[92] C. Liang, J. Y. Cheong, G. Sitaru, S. Rosenfeldt, A. S. Schenk et al., Size-dependent catalytic behavior of gold nanoparticles, *Advanced Materials Interfaces* **9**, 2100867 (2022)

[93] S. Panigrahi, S. Basu, S. Praharaj, S. Pande, S. Jana et al., Synthesis and size-selective catalysis by supported gold nanoparticles: study on heterogeneous and homogeneous catalytic process, *The Journal of Physical Chemistry C* **111**, 4596 (2007)

[94] M. Varón, I. Ojea-Jimenez, J. Arbiol, L. Balcells, B. Martínez et al., Spontaneous formation of hollow cobalt oxide nanoparticles by the kirkendall effect at room temperature at the water–air interface, *Nanoscale* **5**, 2429 (2013)

[95] A. Goldman, R. Cox and H. Brenner, Slow viscous motion of a sphere parallel to a plane wall—i motion through a quiescent fluid, *Chemical Engineering Science* **22**, 637 (1967)

[96] G. Perkins and R. Jones, Hydrodynamic interaction of a spherical particle with a planar boundary i. free surface, *Physica A: Statistical Mechanics and its Applications* **171**, 575 (1991)

[97] A. Daddi-Moussa-Ider, A. Guckenberger and S. Gekle, Long-lived anomalous thermal diffusion induced by elastic cell membranes on nearby particles, *Phys. Rev. E* **93**, 012612 (2016)

[98] B. U. Felderhof, Effect of the wall on the velocity autocorrelation function and long-time tail of brownian motion, *The Journal of Physical Chemistry B* **109**, 21406 (2005)

[99] M. D. Carbajal-Tinoco, R. Lopez-Fernandez and J. L. Arauz-Lara, Asymmetry in colloidal diffusion near a rigid wall, *Phys. Rev. Lett.* **99**, 138303 (2007)

[100] S. Kunz, Supported, ligand-functionalized nanoparticles: An attempt to rationalize the application and potential of ligands in heterogeneous catalysis, *Topics in Catalysis* **59**, 1671 (2016)

[101] L. M. Rossi, J. L. Fiorio, M. A. S. Garcia and C. P. Ferraz, The role and fate of capping ligands in colloidally prepared metal nanoparticle catalysts, *Dalton Trans.* **47**, 5889 (2018)

[102] M. Davidson, Y. Ji, G. J. Leong, N. C. Kovach, B. G. Trewyn et al., Hybrid mesoporous silica/noble-metal nanoparticle materials—synthesis and catalytic applications, *ACS Applied Nano Materials* **1**, 4386 (2018)

[103] Z. H. Farooqi, S. R. Khan and R. Begum, Temperature-responsive hybrid microgels for catalytic applications: a review, *Materials Science and Technology* **33**, 129 (2017)

[104] S. H. Jo, H. W. Kim, M. Song, N. J. Je, S.-h. Oh et al., Core–corona functionalization of diblock copolymer micelles by heterogeneous metal nanoparticles for dual modality in chemical reactions, *ACS Applied Materials & Interfaces* **7**, 18778 (2015)

[105] S. Agarwal, A. Greiner and J. H. Wendorff, Functional materials by electrospinning of polymers, *Progress in Polymer Science* **38**, 963 (2013)

[106] C.-L. Zhang and S.-H. Yu, Nanoparticles meet electrospinning: recent advances and future prospects, *Chem. Soc. Rev.* **43**, 4423 (2014)

[107] A. Bruggink, R. Schoevaart and T. Kieboom, Concepts of Nature in Organic Synthesis: Cascade Catalysis and Multistep Conversions in Concert, *Organic Process Research & Development* **7**, 622 (2003)

[108] H. Zhang, L. Xiong, Z. He, A. Zhong, T. Wang et al., Microporous organic nanotube network supported acid and base catalyst system for one-pot cascade reactions, *New J. Chem.* **40**, 7282 (2016)

[109] B. J. Cohen, M. A. Kraus and A. Patchornik, "Wolf and Lamb" reactions equilibrium and kinetic effects in multipolymer systems, *Journal of the American Chemical Society* **103**, 7620 (1981)

[110] K. E. Price, B. P. Mason, A. R. Bogdan, S. J. Broadwater, J. L. Steinbacher et al., Microencapsulated linear polymers: "soluble" heterogeneous catalysts, *Journal of the American Chemical Society* **128**, 10376 (2006)

[111] M. O. Pretscher, T. Chen, G. Sitaru, S. Gekle, J. Ji et al., Precise 2D-Patterned Incompatible Catalysts for Reactions in One-Pot, *Chem. Eur. J.* **25**, 13640 (2019)

[112] M. O. Pretscher, G. Sitaru, M. Dietel, H. Schmalz, S. Gekle et al., Post-process-functionalized catalytic electrospun and 2d-printed structures for wolf–lamb-type catalysis, *ACS Applied Polymer Materials* **3**, 1349 (2021)

[113] G. Sitaru and S. Gekle, Analytical and computational study of cascade reaction processes in catalytic fibrous membranes, *Computers & Fluids* **240**, 105438 (2022)

[114] B. J. Cohen, M. A. Kraus and A. Patchornik, Organic synthesis involving multipolymer reactions. polymeric trityllithium, *Journal of the American Chemical Society* **99**, 4165 (1977)

[115] Z. Sun, X. Yang, X. Huang, M. Zhang, G. Bian et al., Mesoporous polymeric catalysts with both sulfonic acid and basic amine groups for the one-pot deacetalizationknoevenagel reaction, *New J. Chem.* **43**, 16676 (2019)

[116] E. Yavuz, N. Cherkasov and V. Degirmenci, Acid and base catalysed reactions in one pot with site-isolated polyhipe catalysts, *RSC Adv.* **9**, 8175 (2019)

[117] X. Wang, L. Zhang, Z. Guo, Y. Shi, Y. Zhou et al., Synergistic catalysis of one-pot cascade reactions by acidic and basic binary porous polymers, *Applied Surface Science* **478**, 221 (2019)

[118] F. Gelman, J. Blum and D. Avnir, One-Pot Reactions with Opposing Reagents: Sol-Gel Entrapped Catalyst and Base, *J. Am. Chem. Soc.* **122**, 11999 (2000)

[119] S. Chen, H. Hou, P. Hu, J. H. Wendorff, A. Greiner et al., Effect of Different Bicomponent Electrospinning Techniques on the Formation of Polymeric Nanosprings, *Macromol. Mater. Eng.* **294**, 781 (2009)

[120] F. Weik, R. Weeber, K. Szuttor, K. Breitsprecher, J. de Graaf et al., ESPResSo 4.0 – an extensible software package for simulating soft matter systems, *Eur. Phys. J. Spec. Top.* **227**, 1789 (2019)

[121] C. Bächer, A. Kihm, L. Schrack, L. Kaestner, M. W. Laschke et al., Antimargination of Microparticles and Platelets in the Vicinity of Branching Vessels, *Biophys. J.* **115**, 411 (2018)

[122] L. Li, H. Ling, J. Tao, C. Pei and X. Duan, Microchannel-confined crystallization: shape-controlled continuous preparation of a high-quality CL-20/HMX cocrystal, *CrystEngComm* **24**, 1523 (2022)

[123] M. Toner and D. Irimia, Blood-on-a-chip, *Annual Review of Biomedical Engineering* **7**, 77 (2005), pMID: 16004567

[124] T. Park, S. Lee, G. H. Seong, J. Choo, E. K. Lee et al., Highly sensitive signal detection of duplex dye-labelled dna oligonucleotides in a pdms microfluidic chip: confocal surface-enhanced raman spectroscopic study, *Lab Chip* **5**, 437 (2005)

[125] B. E. Rapp, F. J. Gruhl and K. Länge, Biosensors with label-free detection designed for diagnostic applications, *Analytical and Bioanalytical Chemistry* **398**, 2403 (2010)

[126] V. Kumar, M. Paraschivoiu and K. Nigam, Single-phase fluid flow and mixing in microchannels, *Chemical Engineering Science* **66**, 1329 (2011)

[127] L. Capretto, W. Cheng, M. Hill and X. Zhang, *Micromixing Within Microfluidic Devices*, Springer Berlin Heidelberg, Berlin, Heidelberg, pp. 27–68 (2011)

[128] C.-Y. Lee, C.-L. Chang, Y.-N. Wang and L.-M. Fu, Microfluidic mixing: A review, *International Journal of Molecular Sciences* **12**, 3263 (2011)

[129] Y. Abbas, J. Miwa, R. Zengerle and F. von Stetten, Active continuous-flow micromixer using an external braille pin actuator array, *Micromachines* **4**, 80 (2013)

[130] P.-H. Huang, Y. Xie, D. Ahmed, J. Rufo, N. Nama et al., An acoustofluidic micromixer based on oscillating sidewall sharp-edges, *Lab on a Chip* **13**, 3847 (2013)

[131] M. H. Oddy, J. G. Santiago and J. C. Mikkelsen, Electrokinetic instability micromixing, *Analytical Chemistry* **73**, 5822 (2001)

[132] J. Peter B. Howell, D. R. Mott, S. Fertig, C. R. Kaplan, J. P. Golden et al., A microfluidic mixer with grooves placed on the top and bottom of the channel, *Lab on a Chip* **5**, 524 (2005)

[133] L. Wang, S. Ma, X. Wang, H. Bi and X. Han, Mixing enhancement of a passive microfluidic mixer containing triangle baffles, *Asia-Pacific Journal of Chemical Engineering* **9**, 877 (2014)

[134] S. Hossain, M. Ansari and K.-Y. Kim, Evaluation of the mixing performance of three passive micromixers, *Chemical Engineering Journal* **150**, 492 (2009)

[135] A. Alam, A. Afzal and K.-Y. Kim, Mixing performance of a planar micromixer with circular obstructions in a curved microchannel, *Chemical Engineering Research and Design* **92**, 423 (2014)

[136] S. Z. Razzacki, Integrated microsystems for controlled drug delivery, *Advanced Drug Delivery Reviews* **56**, 185 (2004)

[137] F. Bottausci, I. Mezić, C. D. Meinhart and C. Cardonne, Mixing in the shear superposition micromixer: three-dimensional analysis, *Philosophical Transactions of the Royal Society of London. Series A: Mathematical, Physical and Engineering Sciences* **362**, 1001 (2004)

[138] L.-H. Lu, K. S. Ryu and C. Liu, A magnetic microstirrer and array for microfluidic mixing, *Journal of Microelectromechanical Systems* **11**, 462 (2002)

[139] X. Dai, L. Liu, J. Ouyang, X. Li, X. Zhang et al., Coaxial 3d bioprinting of self-assembled multicellular heterogeneous tumor fibers, *Scientific Reports* **7**, 1457 (2017)

[140] M. Mao, H. Liang, J. He, A. Kasimu, Y. Zhang et al., Coaxial electrohydrodynamic bioprinting of pre-vascularized cell-laden constructs for tissue engineering, *International Journal of Bioprinting* **7**, 362 (2021)

[141] A. E. Kamholz, B. H. Weigl, B. A. Finlayson and P. Yager, Quantitative analysis of molecular interaction in a microfluidic channel: the t-sensor, *Analytical Chemistry* **71**, 5340 (1999), pMID: 10596213

[142] D. Gobby, P. Angeli and A. Gavriilidis, Mixing characteristics of t-type microfluidic mixers, *Journal of Micromechanics and Microengineering* **11**, 126 (2001)

[143] F. G. Bessoth, A. J. deMello and A. Manz, Microstructure for efficient continuous flow mixing, *Anal. Commun.* **36**, 213 (1999)

[144] W. Xing, M. Yin, Q. Lv, Y. Hu, C. Liu et al., 1 - oxygen solubility, diffusion coefficient, and solution viscosity, in W. Xing, G. Yin and J. Zhang, eds., *Rotating Electrode Methods and Oxygen Reduction Electrocatalysts*, Elsevier, Amsterdam, pp. 1–31 (2014)

[145] M. Pham, F. Plourde and S. Doan, Turbulent heat and mass transfer in sinusoidal wavy channels, *International Journal of Heat and Fluid Flow* **29**, 1240 (2008)

[146] R. Mittal and G. Iaccarino, Immersed boundary methods, *Annual Review of Fluid Mechanics* **37**, 239 (2005)

[147] C. S. Peskin, The immersed boundary method, *Acta Numerica* **11**, 479–517 (2002)

[148] A. Guckenberger, M. P. Schraml, P. G. Chen, M. Leonetti and S. Gekle, On the bending algorithms for soft objects in flows, *Computer Physics Communications* **207**, 1 (2016)

[149] A. Guckenberger and S. Gekle, A boundary integral method with volume-changing objects for ultrasound-triggered margination of microbubbles, *Journal of Fluid Mechanics* **836**, 952–997 (2018)

[150] C. Bächer and S. Gekle, Computational modeling of active deformable membranes embedded in three-dimensional flows, *Phys. Rev. E* **99**, 062418 (2019)

[151] T. Krüger, F. Varnik and D. Raabe, Efficient and accurate simulations of deformable particles immersed in a fluid using a combined immersed boundary lattice boltzmann finite element method, *Computers &amp Mathematics with Applications* **61**, 3485 (2011)

[152] S. J. Müller, F. Weigl, C. Bezold, C. Bächer, K. Albrecht et al., A hyperelastic model for simulating cells in flow, *Biomechanics and Modeling in Mechanobiology* **20**, 509 (2020)

[153] D. BARTHÈS-BIESEL, A. DIAZ and E. DHENIN, Effect of constitutive laws for two-dimensional membranes on flow-induced capsule deformation, *Journal of Fluid Mechanics* **460**, 211–222 (2002)

[154] T. Chu, A.-V. Salsac, E. Leclerc, D. Barthès-Biesel, H. Wurtz et al., Comparison between measurements of elasticity and free amino group content of ovalbumin microcapsule membranes: Discrimination of the cross-linking degree, *Journal of Colloid and Interface Science* **355**, 81 (2011)

[155] J. Aubin, D. Fletcher and C. Xuereb, Design of micromixers using CFD modelling, *Chemical Engineering Science* **60**, 2503 (2005)

[156] S. Hossain, A. Husain and K.-Y. Kim, Optimization of micromixer with staggered herring-bone grooves on top and bottom walls, *Engineering Applications of Computational Fluid Mechanics* **5**, 506 (2011)

[157] J. MacInnes, Z. Chen and R. Allen, Investigation of alternating-flow mixing in microchannels, *Chemical Engineering Science* **60**, 3453 (2005)

[158] C. Bächer, L. Schrack and S. Gekle, Clustering of microscopic particles in constricted blood flow, *Physical Review Fluids* **2** (2017)

[159] S. Gekle, Dispersion of solute released from a sphere flowing in a microchannel, *J. Fluid Mech.* **819**, 104 (2017)

Acknowledgements

First of all, I am extremely grateful to my supervisor, Prof. Stephan Gekle, for his invaluable guidance, patience and understanding displayed throughout my entire PhD study.

I would also want to thank all members of the Biofluid Modeling and Simulation group, especially Sebastian Müller for being such a great person to share the office with and Sanwardhini Pantawane for her kindness and all the interesting discussions.

I would like to express my gratitude to Claudia Brandt and Markus Hilt for their help with organisational and technical problems.

Special thanks go to my former professors, Jean Rotaru and Sebastian Popescu, who have inspired and motivated me to study physics.

I am also very grateful to Raisa Biega and her wonderful dog for all the great memories that we have shared.

Finally, I would like to express my deepest gratitude to my family and friends for their unwavering support and tremendous understanding even through difficult times.

Eidesstattliche Versicherung

Hiermit versichere ich an Eides statt, dass ich die vorliegende Arbeit selbstständig verfasst und keine anderen als die von mir angegebenen Quellen und Hilfdmittel verwendet habe.

Weiterhin erkläre ich, dass ich die Hilfe von gewerblichen Promotionsberatern bzw. -vermittlern oder ähnlichen Dienstleistern weder bisher in Anspruch genommen habe, noch künftig in Anspruch nehmen werde.

Zusätzlich erkläre ich hiermit, dass ich keinerlei frühere Promotionsversuche unternommen habe.

Bayreuth, den

Gabriel Sitaru